TECHNISCHE UNIVERSITÄT MÜNCHEN
LEHRSTUHL FÜR NACHRICHTENTECHNIK
Prof. Dr. sc. techn. Gerhard Kramer

---

**Master's Thesis**

# Frame Synchronization for Satellite-based Internet of Things (IoT) Applications

Vorgelegt von:
Marco Liess

München, Dezember 2021

Betreut von:
Dr. Francisco Lázaro (DLR), Dr. Andrea Munari (DLR)

Master's Thesis am
Lehrstuhl für Nachrichtentechnik (LNT)
der Technischen Universität München (TUM)
Titel : Frame Synchronization for Satellite-based Internet of Things (IoT) Applications
Autor : Marco Liess

Marco Liess
marco.liess@tum.de

Ich versichere hiermit wahrheitsgemäß, die Arbeit bis auf die dem Aufgabensteller bereits bekannte Hilfe selbständig angefertigt, alle benutzten Hilfsmittel vollständig und genau angegeben und alles kenntlich gemacht zu haben, was aus Arbeiten anderer unverändert oder mit Abänderung entnommen wurde.

München, 22.12.2021

.......................................................................................

Ort, Datum (Marco Liess)

# Abstract

This thesis aims at exploring the task of frame synchronization in the presence of a large, unknown Doppler shift. The effect of the Doppler shift is twofold. First, it impairs the performance of traditional correlation-based frame synchronization schemes. Second, it introduces intersymbol interference (ISI) due to imperfect receive filtering. The former is first analyzed in an isolated baseband discussion and later complemented by the effects of ISI. Several frame synchronization algorithms robust to frequency offsets are compared in different scenarios. As a reference, we also consider an algorithm employing an optimal metric. It is shown that an approximation of the optimal metric is tight for a high signal-to-noise ratio (SNR), but loses performance in satellite typical low SNR scenarios. Other algorithms, namely the bank of correlators and the swiveled correlator, reach close to optimal performance. In the presence of ISI, the bank of correlators performs the best out of the studied algorithms, but has a high complexity, whereas the swiveled correlator performs worse, but has a very low complexity. Analytic models for the latter two algorithms are presented, which can tightly estimate the performance of the schemes. The models are extended to account for ISI.

# Contents

# Acronyms

**ACF** auto-correlation function. 1, 16, 40

**AWGN** additive white Gaussian noise. 1, 11, 15, 17, 60

**CDF** cumulative density function. 1, 46

**CoC** center of coverage. XI, 1, 79

**EoC** edge of coverage. 1, 79

**FFT** fast Fourier transform. 1, 27, 29–31, 37, 50, 51, 69, 76

**FIR** finite impulse response. XVI, 1, 69, 71

**i.i.d.** independent and identically distributed. 1, 17, 46, 49, 52, 54, 67

**IoT** Internet of Things. vii, 1–3, 5, 6, 8, 11, 16, 38

**ISI** intersymbol interference. i, viii, VIII, XV, 1, 3, 11, 12, 26, 45, 59–63, 65–76, 78, 79, 81, 82

**LEO** low earth orbit. viii, ix, 1, 2, 79, 80

**LRT** likelihood-ratio test. IV, 1, 17–19, 21, 33, 35–39, 41–43, 81, 82

**MAC** medium access control. 1, 5

**ML** maximum likelihood. vii, 1, 8–11, 34

**NB** narrowband. 1

**NP** Neyman-Pearson. 1, 16

**NTN** non-terrestrial network. 1

**PDF** probability density function. 1, 16–18, 46, 47, 50, 51

**PSD** power spectral density. 1, 15, 60

**PSK** phase-shift keying. XVI, 1, 15, 22, 27, 46

**RF** radio frequency. 1, 60

**ROC** receiver operating characteristic. vii, viii, XVI, XVII, 1, 35, 38–42, 52, 53, 55, 56, 70, 72–74, 80

**RV** random variable. 1, 16–18, 45–52, 66, 67, 69

**SINR** signal-to-noise-and-interference ratio. viii, XVI, XVII, 1

**SNR** signal-to-noise ratio. i, vii, viii, 1, 3, 11, 12, 16, 23, 26, 36–43, 52, 55, 69, 71–76, 78–82

**SRRC** square-root raised cosine. vii, viii, VIII, IX, XV–XVII, 1, 59, 60, 62, 63

**TDM** time-division multiplexing. 1, 5

# List of Figures

# List of Tables

# 1. Introduction

In the past years the Internet of Things (IoT) has become more and more ubiquitous and is a driving technology for many emerging applications. At a high level of abstraction, the IoT aims at interconnecting all kinds of electronic devices and integrating them into the Internet in order to interact with them or enable them to publish data. Typical applications include smart homes or smart factories in the context of Industrial IoT, where devices with sensors and actuators are interconnected to monitor, supervise and control specific tasks. A core requirement that all IoT devices have in common is the need for a network connection. Since the location of a device may not be known in advance or may change during its life cycle, the devices are typically connected wirelessly to a gateway in relatively close proximity. Many communication protocols were developed specifically for such use cases, like Sigfox [Sig21] or LoRa [LoR21], which aim to service certain application areas ranging from very low-power devices with a short communication range to long range scenarios with a very poor signal quality.

As the popularity and the quality of IoT solutions increase and its usefulness becomes apparent, more applications are found to benefit from its usage, but still pose challenges to be solved. Such applications include scenarios for which an integration into terrestrial networks is not feasible or which do not offer the possibility of connecting to a near gateway. An example could be maritime buoys containing sensors to measure the chemical composition of the ocean at different locations of the earth. Although the coverage of terrestrial mobile communication systems is good on densely populated continental areas, providing enough gateways and base stations for extremely remote devices located in the middle of an ocean or a desert would be very complex and expensive. Hence, a solution with a much larger coverage area is required. Especially considering that a massive amount of devices have to be serviced, it seems appealing to use a non-terrestrial network (NTN), such as a constellation of satellites. This is also emphasized by recent 3GPP releases, e.g. [3GP21], about the standardization of narrowband (NB)-IoT for NTN, including satellite connectivity. When designing such systems it has to be considered that IoT devices are usually battery operated and have a finite energy budget, which limits the available transmit power and therefore also the maximum distance of the wireless link. It is therefore desirable to choose a satellite constellation in low earth orbit (LEO).

Although this provides a promising solution from an architectural point of view, with the large coverage area enabling the integration of a large number of devices, the nature of a direct LEO satellite link poses new challenges to the communication in the context of the IoT.

Due to the variety of tasks the IoT devices are used for and the need to minimize the power consumption, most devices are in sleep mode for most of the time and sporadically wake up to gather data, interact with their surroundings and transmit or receive information. This does not have to happen in a periodic fashion, since many monitoring tasks only require updating information in the case of a spontaneous change of events. Periodic updates are typical for applications using sensing devices for data collection purposes, while other applications require spontaneous information transmission, such as early warning systems for natural disaster management. Additionally, the amount of data transmitted will be rather small in most occasions. For these reasons, the data will be transmitted in small packets, rather than as a continuous stream.Therefore, we consider a scenario where the devices are uncoordinated and unsynchronized, and sporadically transmit packets, which is described as a bursty transmission. In this scenario, the receiver, i.e., the satellite, has to detect the incoming packets to be able to start a decoding process. This task is essentially known as frame synchronization for bursty transmissions. The problem of detecting the start of a frame has been studied for a long time (see e.g. [Mas72]), however, the nature of a direct LEO satellite link introduces some additional challenges, mainly a large Doppler shift negatively affecting the performance of traditional detection algorithms.

In this setting, the large Doppler shift originates from a large relative speed between the ground terminal and the satellite, induced by the orbital mechanics of the satellite. Hereby, the lower the orbit of the satellite, the larger will be the range of Doppler shifts. Since the maximum slant range of the wireless link is limited by the transmit power of the terminal, increasing the altitude of the satellite to reduce the Doppler shift is not possible. A common strategy to counteract the Doppler shift when directly communicating with a LEO satellite is precompensation. Hereby, the terminal needs accurate knowledge of its own location and the satellite orbit, as well as a stable time reference, which enables it to calculate the satellite's trajectory and position, the expected relative speed and therefore finally the expected Doppler shift. The carrier frequency is then adjusted accordingly in order to ensure the signal arrives at the satellite roughly at the correct frequency. This is also the approach envisioned by the 3GPP [3GP21]. However, IoT devices may not be stationary and may not always have access to their accurate locations. Additionally, the calculation of the Doppler shift requires some computational effort, and very low-power IoT devices often lack the computational resources or the necessary power budget to perform the calculation of the expected Doppler shift. Therefore, in many scenarios IoT devices will not be able to precompensate for the Doppler shift and the correction has to be performed at the satellite.

Thus, a frequency correction requires an estimation of the Doppler shift from the received signal at the satellite, but before that, it is necessary to detect that there is an incoming packet at all. As mentioned above, this becomes significantly more difficult in the presence of a large Doppler shift and is the main focus of this thesis. For this purpose we will thoroughly study the problem of frame synchronization and the effects of a large, unknown Doppler shift on the problem. We consider several algorithms aiming to solve the problem. Hereby, the analysis will be split into two parts: Part I analyzes the impact of a Doppler shift on the baseband version of the incoming signal and the detection algorithms. Part II features an in-depth analysis of the effect of the Doppler shift on the passband signal reception and processing, especially the receive filtering, and the impact of the resulting ISI on the detection process. Therefore, the main contributions of the thesis can be listed as:

- A comprehensive comparison of several relevant detection algorithms is provided for different scenarios. As a reference, we consider an algorithm employing an optimal metric. As a result, it will be shown that a considered approximation of the optimal metric does not perform well in low SNR scenarios, which is the regime in which satellite-based IoT applications are expected to operate.
- We furthermore contribute a detailed discussion of the effects of a large frequency offset on the processing of a passband signal and the impact of the resulting ISI on the presented detectors. Hereby, additionally to a comparison of the presented schemes in different scenarios, we provide an analytic approximation for the algorithms of the simple correlator, the bank of correlators and the swiveled correlator, which accurately estimate their performance, also including the effects of ISI.

# 2. Background and System Model

This chapter will help clarify the system model considered in this thesis. It also provides some fundamentals and prior work on frame synchronization.

## 2.1. System Model and Architecture

IoT systems present certain challenges and requirements on the network. Certainly challenging is the servicing of massive amounts of devices. Although the large coverage area of a satellite allows the connection of a virtually infinite amount of devices, the load and traffic management can pose difficulties. An overview of the considered architecture is given in Figure 2.1. The most important aspect is that heaps of devices will be accessing the network over the same channel, which requires the selection of an appropriate medium access control (MAC) protocol.

For this, the protocol needs to suit the characteristics and requirements of the IoT. The devices are unsynchronized and transmit their data in packets, and, depending on the application, often at sporadic points in time. This results in the traffic being bursty and spontaneous. Such scenarios are typically well suited for random access protocols, which aim at sharing the resources between the users, in contrast to e.g. time-division multiplexing (TDM), where users are assigned different timeslots to transmit, thereby avoiding interference. A random access protocol particularly suitable to a large number of devices with low activity is ALOHA.

Pure ALOHA [Abr70] was the first random access protocol ever developed and uses a blind access approach. This means that any terminal can transmit at any time without considering further information about the channel. This is very applicable for satellite transmission scenarios, as the terminals are usually not in the coverage of each other and can therefore not use any carrier sensing methods. Such an approach will eventually be subject to interference of packets and potentially experience unsuccessful recovery at the satellite. In IoT, this problem is of limited severity since most devices carry out tasks that involve sensing and data gathering, which are typically either not time-critical and able to retransmit data without further consequences, or can tolerate packet losses altogether.

A key task of the receiver is to detect incoming packets. To illustrate the task and the

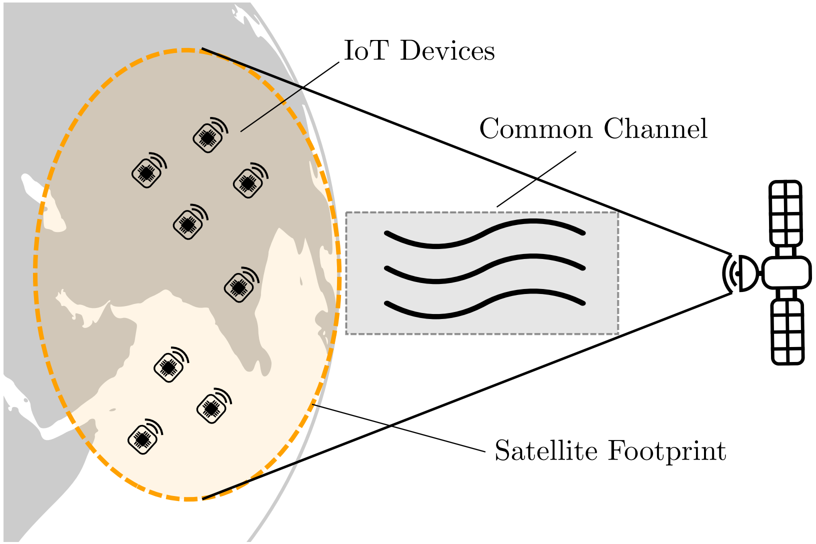

Figure 2.1.: Assumed network architecture in an IoT via satellite scenario. The terminals in the satellites footprint share a common channel.

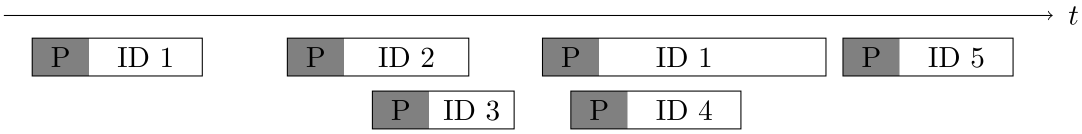

Figure 2.2.: Exemplary timeline for packet traffic. A packet consists of data (white) and a known synchronization sequence (shaded). The origin of the packet is denoted by an identification number. The timeline illustrates different scenarios of interference concerning frame synchronization.

problems that can occur and prevent correct detection Figure 2.2 shows an example input packet traffic to the satellite. Hereby, the origin of the packet is denoted by an identification number. A packet consists of the transmitted data (white) and a known preamble (shaded), whose purpose will be clarified later. For now it is sufficient to know that the preamble is required to successfully detect the packet. The first packet of the bunch does not interfere with other packets and therefore represents the easiest scenario for detection. The second packet's preamble is not overlapping with other packets and therefore also matches the scenario of easy detection. The data of the second packet is interfering with the third packet, which can cause problems and hinder a successful reception. The preamble of the third packet is interfered by the second packet and therefore will be more difficult detect. The preambles of packets four and five are overlapping, which increases the difficulty to detect both packets and may lead to failed detection. Of course, more than two packets may overlap and further prevent correct detection and reception.

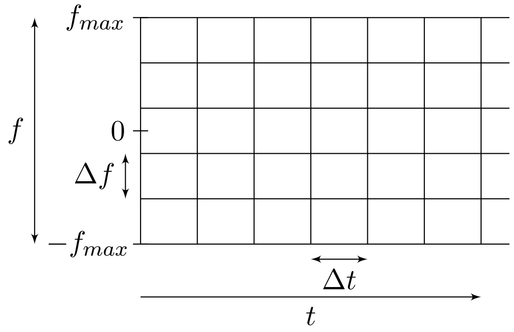

Figure 2.3.: Visualization of frame synchronization with large frequency offsets as a 2D-search problem. The start of a packet is located in one of the grid cells. It is the task of the receiver to identify the correct cell.

Additionally to the problems arising from interference, in the case of a direct satellite link the received signal can be affected by a large Doppler shift. This creates a second unknown, which makes frame synchronization similar to a two-dimensional search problem. This is visualized in Figure 2.3. The search space is a two-dimensional grid that spans infinitely in time with a resolution of $\Delta t$ and spans frequencies up to the maximum expected Doppler shift $f_{\text{max}}$ in both positive and negative direction around the carrier frequency $f_c$. The time resolution $\Delta t$ depends on the symbol time and the oversampling factor and the frequency resolution $\Delta f$ is to be chosen as a trade-off between accuracy and complexity, which will be addressed later in this thesis. The start of a packet is located in one of the grid cells and it is the task of the receiver to locate the packet in the two-dimensional grid.

## 2.2. Background on Frame Synchronization

The problem of detecting the start of a frame has been studied for a long time and solved in a variety of ways. A core concept used by almost all synchronization schemes is the usage of a likelihood function $L(\mu)$, which is a measure for the likelihood that the start of the frame is located at time $\mu$. The design of the likelihood function is a key success criterion that has a large influence on the performance of the detector and depends on the setting and on the available information and resources. The embodiments range from the simple energy detector, which aims to pick up an increase in the energy of the received signal when a frame starts, to the better performing and widely used preamble-based detectors. Here a fixed sequence of symbols, referred to as synchronization sequence or preamble, is known to the transmitter and the receiver and prepended to every packet, as indicated in Figure 2.2. The receiver can then make use of the known sequence to

improve the quality of the output of the likelihood function. Several of such algorithms will be presented in Chapter 4.
The output of the likelihood function then has to be evaluated and interpreted, to determine the presence of packets. Hereby, four outcomes are possible, which are known as correct rejection, successful detection, false alarm and missed detection in literature:

**Correct rejection.** The preamble is absent and the receiver correctly does not detect a packet. This is the desired decision for absent preambles.

**Successful detection.** The preamble is present and the correct sample is identified as the start of the packet. This is the desired decision for present preambles.

**False alarm.** The receiver claims detection based on the output of the likelihood function, although the preamble is absent. From a receiver perspective, this is undesired and leads to the further processing and decoding of the received signal although there is no packet. This results in a waste of resources and may lead to congestions.

**Missed detection.** The preamble is present in the incoming signal, but the detector fails to identify the sequence, which leads to the loss of the packet. The severity of a packet loss depends on the criticality of the application. Some applications, e.g. periodic sensor updates, may tolerate a certain amount of missed detections, while lost packets may have severe consequences in critical applications, such as disaster warning systems.

Mainly two methods can be used to evaluate the output of the likelihood function, which are maximum likelihood (ML) detection and hypothesis testing. Both will be presented and evaluated concerning their applicability in the IoT setting in the following.

### 2.2.1. Maximum Likelihood Detection

The essence of the ML detector is to examine a window of $P$ symbols, where $P$ is typically equal to the length of one frame, and select the time position $\hat{\mu}$, which maximizes the likelihood function. This point in time will then be assumed as the start of the frame. This approach is very promising for scenarios with a fixed frame length and certainty of the presence of a frame start, as is common for continuous transmissions of periodic frames. In bursty settings, several challenges arise using the ML detector, which will now be highlighted.
Let us assume an ML frame detector is employed in a random access scenario, with a timeline similar to the one presented in Figure 2.2. The preamble length is set to $K$ symbols and the length of a packet is not fixed and unknown. The likelihood function

evaluates $K$ consecutive received samples and, therefore, produces a metric for every possible position of the preamble. An exemplary evolution of the metric is depicted in Figure 2.4a. The positions of incoming packets are marked with an arrow. The ML detector now examines batches of $P$ symbols, indicated in the figure by the dashed, vertical lines, and selects the sample corresponding to the largest metric as the start of the packet. In the figure, successful detections are marked with green, solid circles, false alarms are marked with blue, dotted circles and missed packets are marked with red, dashed circles.

It can be seen that in the first window, one packet is present and it is successfully detected, as the likelihood function produced the largest output for the corresponding sample. A characteristic of random access transmissions is that there may be a longer period of time without an incoming packet, followed by multiple packets arriving in a short time period. This is shown in the batches two and three, where two packets arrive in window two and no packet arrives in the third window. The ML detector always selects the highest output of one window as the start of a packet, for which reason in window two it will only successfully detect one packet and miss the other, and in window three it will produce a false alarm.

### 2.2.2. Hypothesis Testing

Hypothesis testing in general is a method to decide between two (or more) statistical hypotheses. Hereby, the considered hypotheses represent different realizations of random variables. In a binary case, the test shall then be used to decide whether some observed data is more likely to be generated by random variables corresponding to the first hypothesis, typically known as null hypothesis, or by the alternative hypothesis. Applied to frame synchronization, the observed data are the samples of the incoming signal, the null hypothesis is that the preamble is absent and the alternative hypothesis is that the preamble is present. Therefore, based on the samples of the incoming signal, the hypothesis test decides if the analyzed output was more likely to be generated by noise, which represents the null hypothesis or by the presence of a preamble, corresponding to the alternative hypothesis.

In literature, the application of hypothesis testing to the frame synchronization problem is also known as sequential frame synchronization [CM06]. As the name suggests, the output of the likelihood function is evaluated sequentially for every time step $\mu$ and compared with a threshold $\lambda$. If the output surpasses the threshold, a detection is assumed. If the output is smaller than the threshold, the next time step is examined.

To analyze the workflow of a detector based on hypothesis testing in a random access

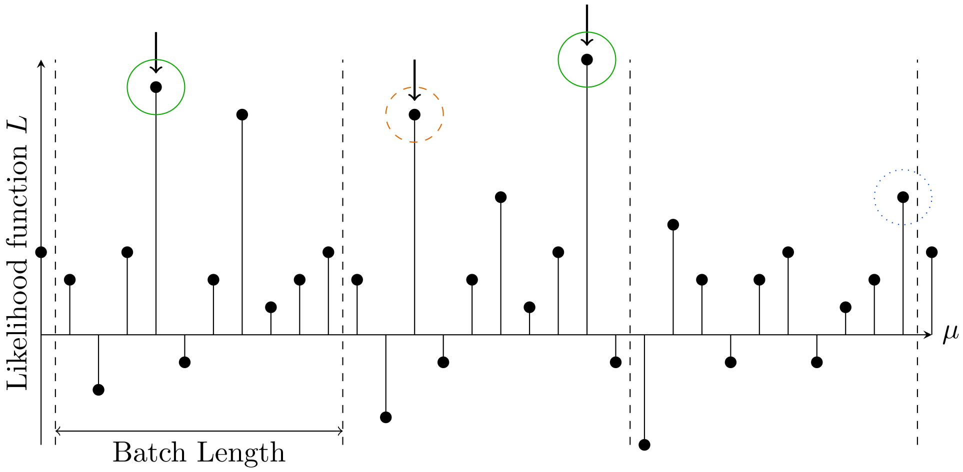

(a) Exemplary ML Detection Output

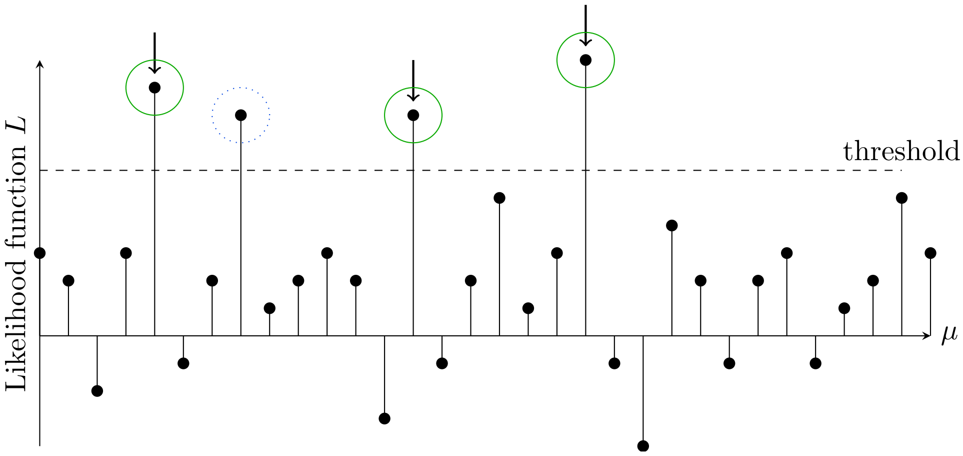

(b) Exemplary Hypothesis Testing Detection Output

Figure 2.4.: Comparison of the workflow and output of the ML detector and hypothesis testing. The likelihood function evaluates $K$ consecutive symbols, where $K$ is the preamble length, and produces an output for every possible position $\mu$ of the preamble. Successful detections are indicated by green, solid circles, false alarms by blue, dotted circles and missed detections by red, dashed circles.

scenario, we will carry out a similar example as for ML detection. The same setting as previously described is assumed. The same likelihood function is employed, so that the exemplary output stream given in Figure 2.4b is equivalent to the one passed to the ML detector in the previous section. In contrast to the ML detector, the detector based on hypothesis testing decides about the presence of a packet for each sample individually, and assumes a detection was made if the threshold is surpassed. In the figure, the threshold level is indicated by the dashed, horizontal line. For the first incoming packet, the output of the likelihood function surpasses the threshold, and the detection is successful. A few samples later, a false alarm occurs, as the threshold was surpassed although no preamble was present. This may happen if incoming noise causes a large output of the likelihood function, which is otherwise only achieved by the presence of a preamble. In sequential detection, the threshold can be optimized to allow a tradeoff between false alarms and correct detections. This can be useful when dealing with different traffic loads to adaptively control the ability to correctly detect more packets at the expense of more false alarms.

### 2.2.3. Related Work

In a pioneering work on frame synchronization, [Mas72], Massey proved that the ML detector in combination with a certain derived likelihood function is optimal, considering a continuous transmission of frames with periodically embedded preambles in an additive white Gaussian noise (AWGN) channel. He explicitly states that the solution does not apply to the synchronization of bursty transmissions. Robertson extended the analysis of the ML detector to other channel models and modulation schemes in [Rob95]. A discussion of a setting with aperiodically inserted preambles and therefore unknown frame lengths in a continuous transmission was performed by Chiani in [CM06], which derived an optimal hypothesis testing framework for the given setting. It is notable that the metric derived for the case of unknown frame lengths was equivalent to the metric found for the case of periodically embedded preambles in [Mas72]. A true bursty transmission scenario was regarded in [SCW08].

In a later work, [Chi10], Chiani extended the discussion to consider imperfectly synchronized channels with phase offsets and very small frequency uncertainty in the recovered baseband symbols. This introduced optimal metrics for both ML and hypothesis testing frameworks in the regarded setting. The work in [CL02] considered imperfect synchronization and larger frequency offsets for an ML detection framework. A more recent approach, presented in [WRKH18], featured a discussion of an optimal hypothesis testing framework for large frequency offsets and a possible, lower complexity realization, which we will analyze in depth. The analysis in [CPV06] and [PVVC$^+$10] included an approximation of the effects of ISI due to imperfect receive filtering for very small frequency shifts.

Considering the problem of frame synchronization in the application of IoT via satellite, several aspects have not been sufficiently explored. A major challenge is the correct packet detection under large Doppler shifts, which has been considered in [CL02] and [WRKH18]. The latter provided an optimal metric and a possible, low complexity approximation. However, the discussion was limited to high SNR scenarios, which may not be given in the setting considered in this thesis. Furthermore, in a realistic communications system, the unknown frequency offset makes it impossible to apply a (perfectly) matched receive filter, which results in the introduction of ISI. This has only been approximated for very small frequency offsets in [CPV06] and [PVVC$^+$10], whereas a detailed discussion for larger offsets is missing.

It seems that, in literature, the usage of hypothesis testing frameworks is more common for bursty transmission scenarios. Additionally, due to the strong unpredictability of random access scenarios, it seems more natural to employ a synchronization algorithm that sequentially makes a decision for every sample, as is the case for hypothesis testing. In the first part of the thesis we will present a discussion of an optimal hypothesis testing framework and a comparison of several practical detection schemes for a simplified setting in baseband. Hereby, different SNR scenarios will be considered. The second part will feature an analysis of the ISI arising from imperfect receive filtering for large frequency offsets and the resulting effects on the frame detection algorithms.

# Part I.

# Analysis in a Baseband Environment

# 3. Optimal Frame Synchronization for Bursty Transmissions

For the first part of this thesis, we will analyze the problem of frame synchronization with a potentially large frequency shift under some simplifying assumptions, which are often considered in literature and which will be described in detail in the first part of this chapter. This allows us to derive an optimal metric for a detection strategy based on hypothesis testing. Furthermore, we are able to derive an approximation to this optimal metric and compare it with other relevant detection schemes. We can also accurately model and predict the performance of some of the presented schemes.

## 3.1. Setting Description

As mentioned in Chapter 2, we assume that a packet consists of a fixed-length, known preamble and data of unspecified length. The preamble $c[k]$ is an $M$-ary phase-shift keying (PSK) modulated symbol sequence of length $K$. In this simplified setting we assume that the signal is transmitted over an AWGN channel and that it may be affected by a Doppler shift $F_d$ and an initial phase offset $\phi$ due to unsynchronized oscillators in the devices. In this case, the received signal is given by

$$r[k] = c[k]\, e^{j(2\pi k F_d T_S + \phi)} + n[k], \quad k \in \{0, K-1\}. \tag{3.1}$$

Hereby, $T_S$ is the symbol period, $n[k]$ is zero-mean complex white Gaussian noise with a variance of $\sigma_n^2 = \frac{N_0}{2}$ in each dimension, where $N_0$ is the one-sided power spectral density (PSD) of the noise, and k is the time index.

For the remainder of the thesis we will characterize the Doppler effect by the normalized frequency shift $f_d = F_d T_S$, or its representation in $\frac{\text{radians}}{\text{sample}}$ as $\theta = 2\pi F_d T_S$, therefore we have

$$r[k] = c[k]\, e^{j(2\pi k f_d + \phi)} + n[k] = c[k]\, e^{j(\theta k + \phi)} + n[k]. \tag{3.2}$$

This enables us to present our discussion independent of the symbol rate of the system.

Both the Doppler shift $\theta$ and the phase offset $\phi$ can be viewed as realizations of their random variables (RVs) $\Theta$ and $\Phi$. For the analytic discussion of the thesis, they will be assumed to be uniformly distributed, i.e., $\Theta \sim \mathcal{U}(-2\pi f_{\text{max}}, 2\pi f_{\text{max}}), \Phi \sim \mathcal{U}(-\pi, \pi)$. Therefore, we can define the probability density functions (PDFs) of these RVs as:

$$f_\Theta(\theta) = \begin{cases} \frac{1}{4\pi f_{\text{max}}} & \theta \in [-2\pi f_{\text{max}}, 2\pi f_{\text{max}}] \\ 0 & \text{otherwise,} \end{cases} \qquad f_\Phi(\phi) = \begin{cases} \frac{1}{2\pi} & \phi \in [-\pi, \pi] \\ 0 & \text{otherwise.} \end{cases} \tag{3.3}$$

Unless otherwise specified, the maximum Doppler shift will be assumed to be $f_{\text{max}} = 0.5$, therefore $\Theta \sim \mathcal{U}(-\pi, \pi)$. A more realistic approach than assuming a uniform Doppler shift will be considered in Chapter 8.

## 3.2. Optimal Likelihood Ratio Test

Recalling the background on hypothesis testing given in Chapter 2 and taking into account the setting we defined above, we can now formulate the two hypotheses regarding frame detection:

$$\begin{aligned} &\mathcal{H}_0 : r[k] = n[k], \quad k \in \{0, K-1\} \\ &\mathcal{H}_1 : r[k] = c[k]\, e^{j(\theta k + \phi)} + n[k], \quad k \in \{0, K-1\}. \end{aligned} \tag{3.4}$$

Hereby, the null hypothesis $\mathcal{H}_0$ describes the case in which the incoming signal does not contain the preamble and is only defined by noise. The alternative hypothesis $\mathcal{H}_1$ accounts for the cases in which the signal contains the Doppler affected preamble and therefore stands for the location of the start of the packet. In a practical setting, there are actually more than these two possibilities, since only a fraction of the preamble may be contained in the input signal, or it may overlap with signals from other terminals. However, we disregard these cases for the sake of simplicity. In general, this will be a valid assumption when considering low SNR scenarios, as are typical for satellite-based IoT applications, and a properly chosen preamble with very good autocorrelation properties. This means that the auto-correlation function (ACF) of the preamble yields a large output for the central sample and very small output for the side lobes. Therefore, the correlation output of a partially contained preamble is expected to be very low, hereby being dominated by the noise and subsumed by the $\mathcal{H}_0$ hypothesis.[1]

The decisions for either of the two hypothesis are indicated by $\mathcal{D}_0$ and $\mathcal{D}_1$, respectively. To make this decision, the Neyman-Pearson (NP) lemma [NP33] demonstrates that the

---

[1] For continuous transmissions it was empirically confirmed in [CM06], that partially contained preambles generally cause for a lower amount of false alarms and therefore less disturbance than random data.

most powerful test, i.e., the optimal decision rule, is given by a likelihood-ratio test (LRT), where the ratio of the PDFs of the two hypothesis are compared to a threshold $\lambda$. If the ratio stays below the threshold the null-hypothesis $\mathcal{H}_0$ will be accepted, whereas it will be rejected if the threshold is exceeded. The likelihood function corresponding to the optimal LRT can be formulated as

$$L_{\mathrm{O}}(\mu) = \frac{f_{\mathbf{R}}(\mathbf{r}|\mathcal{H}_1)}{f_{\mathbf{R}}(\mathbf{r}|\mathcal{H}_0)} \underset{\mathcal{H}_0}{\overset{\mathcal{H}_1}{\gtrless}} \lambda, \tag{3.5}$$

where $\mathbf{r} = (r[\mu+0], r[\mu+1], ..., r[\mu+K-1])$ is the vector of incoming samples, which represent realizations of the RVs $\mathbf{R} = (R[\mu+0], R[\mu+1], ..., R[\mu+K-1])$, where the randomness originates from the noise.

Following the approach given by [WRKH18], in this idealized environment it is possible to find expressions for these PDFs and also find a closed form expression for the optimal LRT. A brief overview of the methods used to obtain a solution will be presented here, while a detailed derivation can be found in Appendix A.1.

To obtain an expression for the PDF of the null hypothesis $f_{\mathbf{R}}(\mathbf{r}|\mathcal{H}_0)$ we can use the properties of AWGN, since the samples only contain noise. Therefore, the RVs in $\mathbf{R}$ are independent and identically distributed (i.i.d.) and each of them follows a complex Gaussian distribution:

$$f_{R[\mu+k]}(r[\mu+k]|\mathcal{H}_0) = \frac{1}{\pi\sigma_n^2}\ e^{-\frac{1}{\sigma_n^2}|r[\mu+k]|^2}. \tag{3.6}$$

Using the independence, their joint PDF is given as

$$f_{\mathbf{R}}(\mathbf{r}|\mathcal{H}_0) = \frac{1}{(\pi\sigma_n^2)^K}\ e^{-\frac{1}{\sigma_n^2}\sum\limits_{k=0}^{K-1}|r[\mu+k]|^2}. \tag{3.7}$$

Regarding the PDF of the alternative hypothesis $f_{\mathbf{R}}(\mathbf{r}|\mathcal{H}_1)$, we know that the received signal $\mathbf{r}$ contains the Doppler and phase shifted preamble and noise. As the Doppler shift and phase offset are also RVs and their distributions are known, integrating over their distributions renders them given. Therefore, we can express the PDF of $\mathcal{H}_1$ in terms of the conditional PDF of $\mathbf{R}$ given $\Phi$ and $\Theta$, and the PDFs of $\Phi$ and $\Theta$ as

$$f_{\mathbf{R}}(\mathbf{r}|\mathcal{H}_1) = \int\limits_{-2\pi f_{\max}}^{2\pi f_{\max}} \int\limits_{-\pi}^{\pi} f_{\mathbf{R}|\Phi,\Theta}(\mathbf{r}|\mathcal{H}_1, \phi, \theta)\ f_{\Phi}(\phi)\ f_{\Theta}(\theta)\ d\phi\ \ d\theta. \tag{3.8}$$

We can now follow the same approach as for the PDF of $\mathcal{H}_0$, except that the argument is now not only characterized by $\mathbf{r}$, but also by the preamble $\mathbf{c} = (c[0], c[1], ..., c[K-1])$, the phase offset $\phi$ and the Doppler shift $\theta$. The only remaining RV is the noise, for which an expression can be found by solving Equation (3.4) for $n[k]$. The resulting PDF then corresponds to a nonzero mean complex Gaussian distribution:

$$f_{\mathbf{R}|\Phi,\Theta}(\mathbf{r}|\mathcal{H}_1,\phi,\theta) = \frac{1}{(\pi\sigma_n^2)^K}\, e^{-\frac{1}{\sigma_n^2}\sum\limits_{k=0}^{K-1}\left|r[\mu+k]-c[k]e^{j(\theta k+\phi)}\right|^2}. \tag{3.9}$$

Inserting the found expressions (3.7), (3.8), (3.9) and the PDFs of $\Phi$ and $\Theta$ given in Equation (3.3) into the optimal LRT yields

$$\begin{aligned} L_{\mathrm{O}}(\mu) &= \frac{\int\limits_{-\pi}^{\pi}\int\limits_{-2\pi f_{\max}}^{2\pi f_{\max}} f_{\mathbf{R}|\Phi,\Theta}(\mathbf{r}|\mathcal{H}_1,\phi,\theta)\; f_\Phi(\phi)\; d\phi\;\; f_\Theta(\theta)\; d\theta}{f_{\mathbf{R}}(\mathbf{r}|\mathcal{H}_0)} \overset{\mathcal{H}_1}{\underset{\mathcal{H}_0}{\gtrless}} \lambda \\ &= \frac{\frac{1}{8\pi^2 f_{\max}}\int\limits_{-\pi}^{\pi}\int\limits_{-2\pi f_{\max}}^{2\pi f_{\max}} \frac{1}{(\pi\sigma_n^2)^K} e^{-\frac{1}{\sigma_n^2}\sum\limits_{k=0}^{K-1}\left|r[\mu+k]-c[k]e^{j(\theta k+\phi)}\right|^2} d\phi\; d\theta}{\frac{1}{(\pi\sigma_n^2)^K}\; e^{-\frac{1}{\sigma_n^2}\sum\limits_{k=0}^{K-1}|r[\mu+k]|^2}} \overset{\mathcal{H}_1}{\underset{\mathcal{H}_0}{\gtrless}} \lambda. \end{aligned} \tag{3.10}$$

This expression can be simplified (see Appendix A.2 for details), to finally describe the optimal LRT as

$$L_{\mathrm{O}}(\mu) = \frac{1}{4\pi f_{\max}} \int\limits_{-2\pi f_{\max}}^{2\pi f_{\max}} I_0\left(\frac{2}{\sigma_n^2}\left|\sum_{k=0}^{K-1} r[\mu+k]\, c^*[k]\, e^{-j\theta k}\right|\right)\, d\theta \overset{\mathcal{H}_1}{\underset{\mathcal{H}_0}{\gtrless}} \lambda, \tag{3.11}$$

where $I_0(x)$ is the modified Bessel function of the first kind and zeroth order. This is defined in [Wat95] as

$$I_0(x) = \frac{1}{2\pi}\int_{-\pi}^{\pi} e^{x\cos(\phi)}\, d\phi. \tag{3.12}$$

The argument of the Bessel function in Equation (3.11) corresponds to the absolute value of the correlation of the received signal and a variably frequency shifted preamble [2]. The complete expression can, however, not be easily implemented, as it involves the evaluation of the Bessel function, which is very complex for the given argument. This is shown in Appendix A.2 by using the series representation of the Bessel function. A

---

[2] Integrating over all possible frequencies can be viewed as correlating the incoming signal with infinitely many, differently frequency shifted preambles and summing the results. This therefore definitely includes the correlation of the Doppler shifted preamble in the received signal with the equally shifted local preamble, which corresponds to the autocorrelation and gives a large output.

possible approach is to approximate the expression by only regarding the first few terms of the infinite series. This approach was also taken in [WRKH18] and will be further analyzed later in the thesis. It will also be compared to the optimal LRT and several other detection schemes presented in the next chapter.

# 4. Comparison of relevant Synchronization Algorithms

In this chapter we will present several relevant synchronization algorithms, which, in contrast to the optimal LRT presented in the previous chapter, are more easily implementable. Hereby, we will stick to the approach of describing the algorithms with a likelihood function, which is then compared to a threshold $\lambda$ to decide whether the frame start was found or not.

## 4.1. Simple Correlator

The simple correlator is a widely used detector in practice and one of the simplest preamble-based schemes. As introduced in Section 2.2, we assume that a preamble is prepended to a packet that can then be used by the receiver to correctly identify the start of a frame. In the case of the simple correlator, in order to locate the preamble the receiver correlates the incoming sample stream with the known preamble and then takes the absolute value of the result. The corresponding block diagram is shown in Figure 4.1. The likelihood function can therefore be expressed as

$$L_{\mathrm{C}}(\mu) = \left| \sum_{k=0}^{K-1} r[\mu+k]\, c^*[k] \right| . \tag{4.1}$$

Since the received signal has an unknown phase and frequency shift, this is also referred to as noncoherent correlation in literature and may also be referred to as such in the thesis.

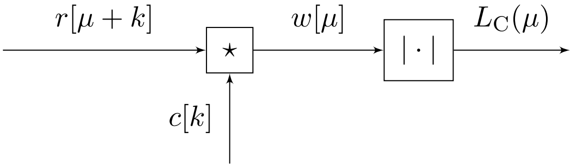

Figure 4.1.: Block diagram of the simple correlator.

As mentioned in Section 3.1, we assume that the preamble has very good correlation properties. This means that the correlation of the input stream with the preamble will result in a very high output if the preamble is present and aligned, while the correlation with any other sequence or a misaligned preamble will produce a very small output. However, due to this property and the dependency of the correlation on the phase, a large Doppler shift can severely decrease the output of the correlation for aligned preambles and therefore affect the performance. The effect of a Doppler shift on the output of the simple correlator in the case of aligned preambles will now be mathematically analyzed.

At the correct sample, which we will denote with $\mu = 0$, the incoming signal $\mathbf{r}$ contains the frequency shifted preamble superimposed to noise, as described in Equation (3.1), and is correlated with the known preamble $\mathbf{c}$. The correlation output for fully overlapping preambles is given as

$$\begin{aligned} w[0] &= \sum_{k=0}^{K-1} r[k]\, c^*[k] \overset{(3.1)}{=} \sum_{k=0}^{K-1} \left(e^{j(2\pi f_d k+\phi)} c[k] + n[k]\right) c^*[k] \\ &= \sum_{k=0}^{K-1} e^{j(2\pi f_d k+\phi)}\, c[k]\, c^*[k] + \sum_{k=0}^{K-1} n[k]\, c^*[k]. \end{aligned} \tag{4.2}$$

It can be seen that due to the additive property of the noise the result can be split into the correlation of the preamble with a Doppler shifted version of itself and the correlation of the preamble with the noise. The first term has a very characteristic influence on the output, which will shortly be presented, and it will also play a role in the further discussion of the other correlation-based synchronization schemes. For these reasons, we will define it as an auxiliary function:

$$R_0(f_d) = \sum_{k=0}^{K-1} e^{j(2\pi k f_d+\phi)}\, c[k]\, c^*[k]. \tag{4.3}$$

We can further simplify this expression using the property $z^* z = |z|^2$ for complex numbers and the property $|c[k]|^2 = E_S$ for PSK symbols, where $E_S$ is the symbol energy. Furthermore, without loss of generality, we assume that symbols have unit energy, i.e., $E_S = 1$. From here it can already be established that $R_0$ does not depend on the specific preamble, but only on its length and the frequency and phase shift. Using some further modifications presented in Appendix A.3, $R_0$ can be simplified to

$$R_0(f_d) = \sum_{k=0}^{K-1} e^{j(2\pi k f_d+\phi)} = \frac{\sin(K\pi f_d)}{\sin(\pi f_d)}\, e^{j((K-1)\pi f_d+\phi)}. \tag{4.4}$$

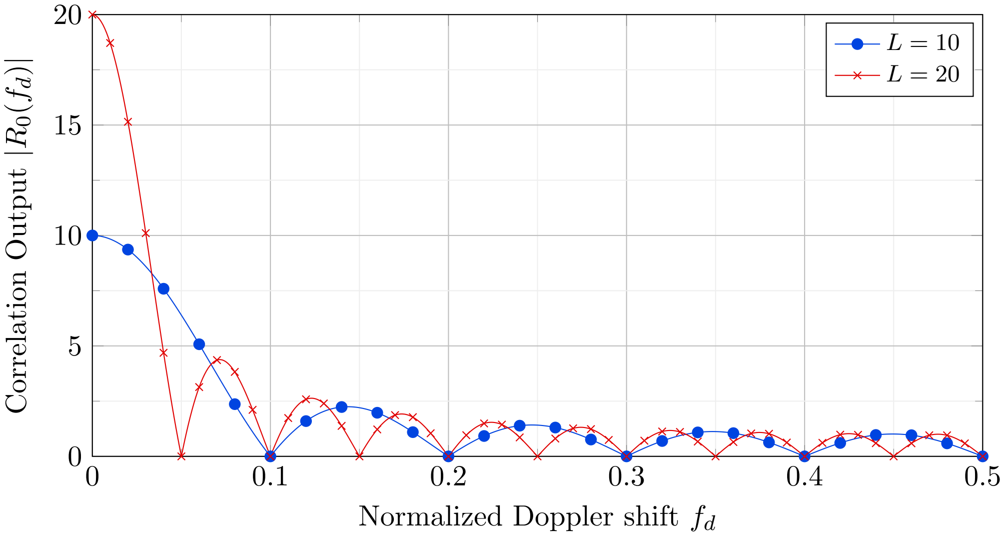

Figure 4.2.: Magnitude of $R_0(f_d)$ for different preamble lengths $K = 10$ and $K = 20$. Restricted to positive frequencies as function is symmetric.

It becomes apparent that the absolute value of $R_0$ only depends on the preamble length $K$ and the Doppler shift $f_d$. We are now interested in the effect of the Doppler shift on the output of the simple correlator. In a noiseless scenario, i.e., $n[k] = 0$, for all $k$, the output simplifies to the absolute value of $R_0$. Therefore, $|R_0|$ can give us an idea of how the simple correlator behaves in different Doppler shifts. It is plotted across the range of possible Doppler shifts and for different preamble lengths $K$ in Figure 4.2.

Mainly two characteristics can be identified when comparing the correlation output for the different preamble lengths. For a normalized Doppler shift of $f_d = 0$, it can be seen that the amplitude of the output corresponds to the preamble length. Therefore, longer preambles induce a larger correlation output, which in turn leads to an improved performance against noise and interference. The second characteristic involves the behavior of the output across the range of frequency shifts, which shows that the amplitude of the output decreases rapidly with growing Doppler shifts. Furthermore, this effect is increased for longer preambles. We can identify that the correlation output is zero for $f_d = \frac{1}{K}$, for which a detection is definitely impossible. A reliable detection is therefore only possible for Doppler shifts well below $\frac{1}{K}$, for which the output of the correlation is still large. In this sense, we define the bandwidth of a correlator to be the maximum Doppler shift for which a reliable detection is still possible. This depends on the scenario, i.e., the SNR, and the requirements of the applications, but it is definitely far less than $\frac{1}{K}$.

Summarizing, we can identify a tradeoff concerning the preamble length, where longer preambles lead to an increased robustness against noise, but in turn reduce the bandwidth against frequency shifts. However, also with short preambles the simple correlator is not able to reliably detect packets for large Doppler shifts. It is therefore necessary to consider other synchronization schemes, which are more robust against frequency shifts, as will be done in the next sections.

## 4.2. Bank of Correlators

The most straightforward approach to cover a greater range of Doppler shifts is by simply operating several simple correlators at different center frequencies. This algorithm is known as bank of correlators and the idea is to evenly space $N$ simple correlators in the expected Doppler range ($[-f_{\max}, f_{\max}]$) and hereby ensure that one of the correlators operates inside its bandwidth. As the output of the simple correlator decreases very quickly with growing frequency shifts, a larger number of parallel correlators, also known as branches, will lead to better performance. This can be expressed by the resolution of the bank of correlators, which is the frequency difference between two adjacent branches:

$$\Delta f = 2\frac{f_{\max}}{N-1}^{1}. \tag{4.5}$$

The likelihood function of the bank of correlators can therefore be expressed as

$$L_{\mathrm{B}}(\mu) = \max_{i}\left(\left|\sum_{k=0}^{K-1} e^{-j2\pi k(f_{\max}-(i-1)\Delta f)}\, r[\mu+k]\, c^{*}[k]\right|\right), \quad i \in \{1, N\}. \tag{4.6}$$

The corresponding block diagram is shown in Figure 4.3. The algorithm takes the incoming signal $\mathbf{r}$ as an input and passes it to $N$ branches. The first step is to apply a different frequency shift to the incoming signal for every branch. The frequency shifted signals are then supplied to a simple correlator in each branch, which was analyzed in the previous section. At least one of those correlators will operate on a frequency shifted preamble which is inside its bandwidth and, depending on the noise, will therefore likely produce a reliable output. The output of the bank of correlators will then be the maximum of the outputs of each branch. It is notable that the algorithm also outputs an estimate of the Doppler shift $\tilde{f}[\mu]$, which can be derived from the index of the branch that caused the largest output. This can then be used for the correction and further processing of the data part of the detected packet.

---

[1] In the special case of $f_{\max} = 0.5$, the two outermost branches will be shifted by $e^{-j\pi k}$ and $e^{j\pi k}$ respectively, which is equivalent. Thus, one of the branches is redundant. It is therefore desirable to redistribute the branches between $[-f_{\max}, f_{\max}(1-\frac{1}{N})]$. The resolution is then given as $\Delta f = 2\frac{f_{\max}}{N}$.

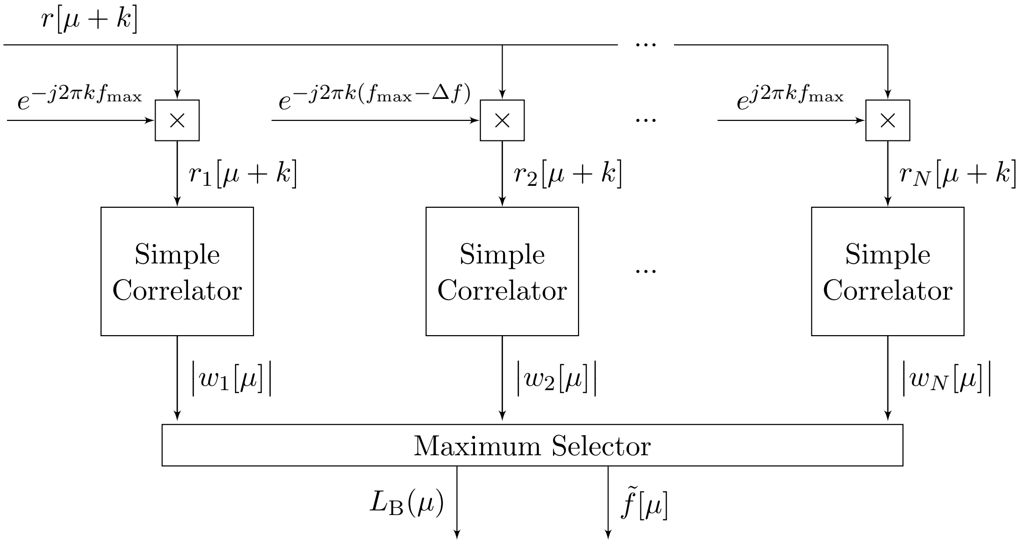

Figure 4.3.: Block diagram of the bank of correlators in baseband.

Regarding the analysis of the output, by applying different frequency shifts to every branch, the branch with the frequency shift closest to the actual Doppler shift experienced by the signal will have a maximum residual frequency offset of $\hat{f}_r = \frac{1}{2}\Delta f$. The actual residual frequency offset $f_r$ will always be smaller than this, i.e., $|f_r| \leq \hat{f}_r$. However, due to noise, this does not mean that this branch will also give the highest output. But it can be used to get more information on the expected output of the algorithm for different Doppler shifts, similar to the analysis for the simple correlator. For this, we again consider the correct sample $\mu = 0$, where the Doppler affected preamble is fully contained in the incoming signal. For the branch with the frequency shift closest to the actual Doppler shift, let us assume this is the $i$-th branch, a lot of the initial frequency offset is corrected and only a residual offset remains. This gives

$$\begin{aligned} |w_i[0]| &= \left| \sum_{k=0}^{K-1} e^{j(\pm 2\pi k f_r + \phi)} \, c[k] \, c^*[k] + \sum_{k=0}^{K-1} n[k] \, c^*[k] \right| \\ &= \left| R_0(f_r) + \sum_{k=0}^{K-1} n[k] \, c^*[k] \right| . \end{aligned} \tag{4.7}$$

In a noiseless scenario, this branch will give the highest output and therefore the complete output of the bank of correlators can also be characterized by $R_0$, but in contrast to the simple correlator the frequency argument $f_r$ has a much smaller range. The maximum residual frequency was already presented earlier, hence, the range of $f_r$ can be given as

$$f_r \in [-\hat{f}_r, \hat{f}_r] = [-\frac{\Delta f}{2}, \frac{\Delta f}{2}]. \tag{4.8}$$

By adjusting the number of branches $N$, the range of residual frequencies can be controlled and, recalling the shape of $R_0$, the output of the closest branch can be kept in an operating window that allows a reliable detection. Virtually, this means that increasing the number of branches leads to an increase in performance. In fact, we can see that if we were to use an infinite number of correlators, i.e., $N = \infty$, the maximum residual frequency offset would go to zero. This would lead to a scenario of a fully compensated Doppler shift.

Although increasing the number of branches reduces the residual frequency offset and therefore significantly improves the performance, it also results in a complexity increase, as every added branch implies an additional simple correlator that needs to be operated. Although this tradeoff also has its advantages in certain scenarios, it fails to provide a good solution in very low SNR scenarios, where it is necessary to employ very long preambles in order to increase the correlation output with respect to the noise. As discussed for the simple correlator, longer preambles lead to a shorter bandwidth of the simple correlator, which has to be counteracted in the bank of correlators by employing more branches and increasing the complexity. Due to this large complexity in low SNR, the bank of correlators may not be feasible to be executed on a satellite.

## 4.3. Swiveled Correlator

### 4.3.1. Description

While the previous two correlators rely on the output of the correlation of the incoming signal and the preamble to be detectable against the noise, the idea of the swiveled correlator is to detect the Doppler shift in the incoming preamble. The algorithm was first presented in [SKMB90] and is used in the S-MIM system [DGdRHG14]. Since then it has been referenced and analyzed in [SSS$^+$00, WRKH17], however we will extend the discussion by deriving an analytic model for the considered setting, also including the effects of ISI in Part II of the thesis.

The principle workflow of the algorithm is to firstly split the local preamble into $N$ parts of length $M = \frac{K}{N}$. These preamble fragments can be denoted as

$$\mathbf{c}_n = (c[(n-1)M],\, c[(n-1)M+1], ...,\, c[nM-1]), \tag{4.9}$$

where $n \in \{1, N\}$ is the index of the respective branch. The incoming signal $\mathbf{r}$ will then be correlated with the respective preamble fragment in each branch. The outputs will be aligned in time by means of a delay. The idea of the swiveled correlator is then to combine the partial correlation outputs by applying several phase shifts, so that the signals add up constructively. This can be efficiently implemented using a fast Fourier transform (FFT). The corresponding block diagram is depicted in Figure 4.4.

For a better understanding of the algorithm, we can analyze the effect for each processing step. First, the subsequences of the incoming signal are noncoherently correlated with the partial preamble corresponding to each branch. Formally, we have

$$w_n[\mu] = \sum_{k=(n-1)M}^{nM-1} r[\mu + k]\, c^*[k]. \tag{4.10}$$

If the input signal only contains noise, then the output of all branches will have a random phase. If the input signal contains the full preamble, the idea of the partial correlation in each branch is to eliminate the phase of the PSK-modulated symbols, so that only the Doppler shift $f_d$, the constant initial phase offset $\phi$ and the phase of the disturbing noise remains in the input signal. Therefore, disregarding the distortion by the noise, the phase difference between the outputs of two adjacent branches is equivalent to the Doppler shift experienced over the length of the subsequence, i.e., $f_d M$. This Doppler induced phase shift shall be detected by a subsequent FFT, taken over the aligned outputs of the branches, i.e., over the dimension $n$ (and not $k$, which is the temporal dimension). A general expression for the output of the $i$-th FFT bin can be given as

$$v_i[\mu] = \sum_{n=1}^{N} w_n[\mu]\, e^{-j2\pi \frac{n}{N} i}. \tag{4.11}$$

Combining Equations (4.10) and (4.11), as well as selecting the bin with the highest absolute value, yields the full expression of the likelihood function of the swiveled correlator:

$$L_{\mathrm{S}}(\mu) = \max_i \left( \left| \sum_{n=1}^{N} \sum_{k=(n-1)M}^{nM-1} r[\mu + k]\, c^*[k]\, e^{-j2\pi \frac{n}{N} i} \right| \right), \quad i \in \{1, N\}. \tag{4.12}$$

Similar to the previous algorithms, in order to obtain information on the behavior of the swiveled correlator across different Doppler shifts, we will analyze the found expressions in case of a fully contained preamble. Therefore, assuming $\mu = 0$ and starting from Equation (4.10), the output of the partial correlations in case of a present preamble can

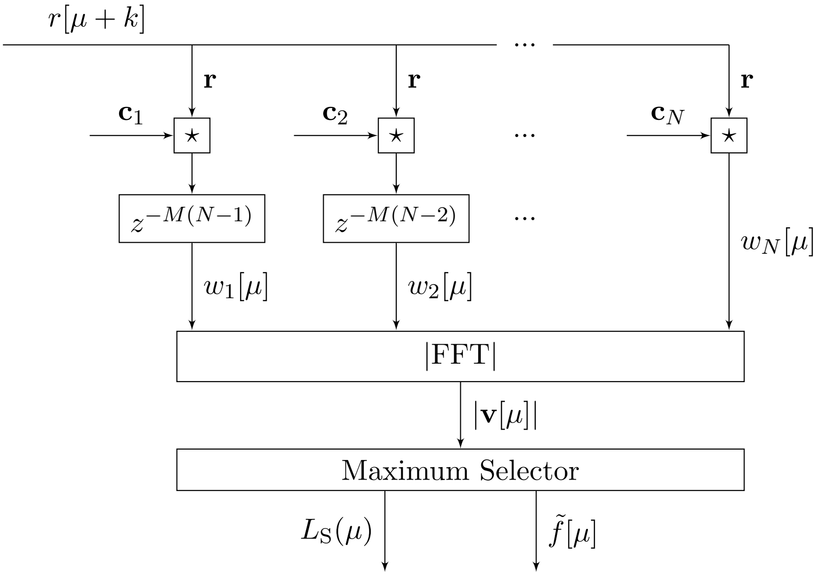

Figure 4.4.: Block diagram of the swiveled correlator. The preamble is split into $N$ fragments of length $M = \frac{K}{N}$.

be given as

$$\begin{aligned} w_n[0] &= \sum_{k=(n-1)M}^{nM-1} e^{j(2\pi k f_d+\phi)}\, c[k]\, c^*[k] + \sum_{k=(n-1)M}^{nM-1} n[k]\, c^*[k] \\ &= e^{j2\pi f_d (n-1)M} \sum_{k=0}^{M-1} e^{j(2\pi k f_d+\phi)} + \sum_{k=(n-1)M}^{nM-1} n[k]\, c^*[k]. \end{aligned} \tag{4.13}$$

Hereby, we can observe that the Doppler induced phase difference between adjacent branches $w_n$ and $w_{n+1}$ is $e^{j2\pi f_d M}$. Thus, we will only be able to unequivocally detect normalized frequency shifts in the range $f_d \in \left(-\frac{1}{2M}, \frac{1}{2M}\right]$. For larger frequency offsets $|f_d| > \frac{1}{2M}$, the swiveled correlator will still give a large output and detect a peak, however, there will be several possible frequencies ($f_d + i\frac{1}{M}$, $i \in \mathbb{Z}$) that are indistinguishable. This prohibits the determination of a reliable estimate of the Doppler shift in cases for $|f_d| > \frac{1}{2M}$.

We can rewrite Equation (4.13) using $R_0(f_d)$ given in Equation (4.4):

$$w_n[0] = e^{j2\pi f_d (n-1)M} R_0^{(M)}(f_d) + \sum_{k=(n-1)M}^{nM-1} n[k]\, c^*[k], \tag{4.14}$$

where $R_0$ is adjusted to the length of the partial correlation:

$$R_0^{(M)}(f_d) = \frac{\sin(M\pi f_d)}{\sin(\pi f_d)}\; e^{j((M-1)\pi f_d + \phi)}. \tag{4.15}$$

This indicates that the outputs of the partial correlations suffer from the same noncoherent correlation loss experienced by the simple correlator. A more detailed interpretation follows shortly. The next step is the FFT, which, given the output of the branches in Equation (4.14), can be computed as

$$v_i[0] = R_0^{(M)}(f_d) \sum_{n=1}^{N} e^{j2\pi f_d (n-1)M} e^{-j2\pi \frac{n}{N} i} + \sum_{n=1}^{N} \sum_{k=(n-1)M}^{nM-1} n[k]\, c^*[k]\, e^{-j2\pi \frac{n}{N} i}. \tag{4.16}$$

The summation in the first term is very similar to the summation in $R_0$, and it also has a very characteristic influence on the expected output of the swiveled correlator, for which reason we will also define it as an auxiliary function:

$$K_{0,i}(f_d) = \sum_{n=1}^{N} e^{j2\pi f_d (n-1)M} e^{-j2\pi \frac{n}{N} i}. \tag{4.17}$$

Since the expression is very similar to $R_0$, we can follow the same methods presented in Appendix A.3 to simplify the expression to

$$K_{0,i}(f_d) = \frac{\sin(\pi(f_d K - i))}{\sin(\frac{\pi}{N}(f_d K - i))}\; e^{j\pi\left((N-1)(f_d M - \frac{N+1}{N} i\right)}. \tag{4.18}$$

In a noiseless case, the output of the swiveled correlator is then finally given by

$$|K_0(f_d) R_0^{(M)}(f_d)|, \tag{4.19}$$

where

$$K_0(f_d) = \max_i \left(|K_{0,i}(f_d)|\right). \tag{4.20}$$

Figure 4.5 shows a plot of the expected output of the swiveled correlator for different subsequence lengths. It is important to note the shape of the curves only depends on $M$, i.e., the ratio of $K$ to $N$, and varying $K$ only affects the scale of the curves. The effect of the noncoherent correlation loss $R_0$ is shown by the envelopes, which are given in the figure by the dashed curves. Hereby, it can be seen that noncoherently combining longer subsequences leads to a greater loss for smaller frequency shifts, as was also emphasized for the simple correlator. It is notable that $M = 1$ corresponds to the case where subsequences of length 1 are correlated, i.e., each symbol of the preamble is processed in a

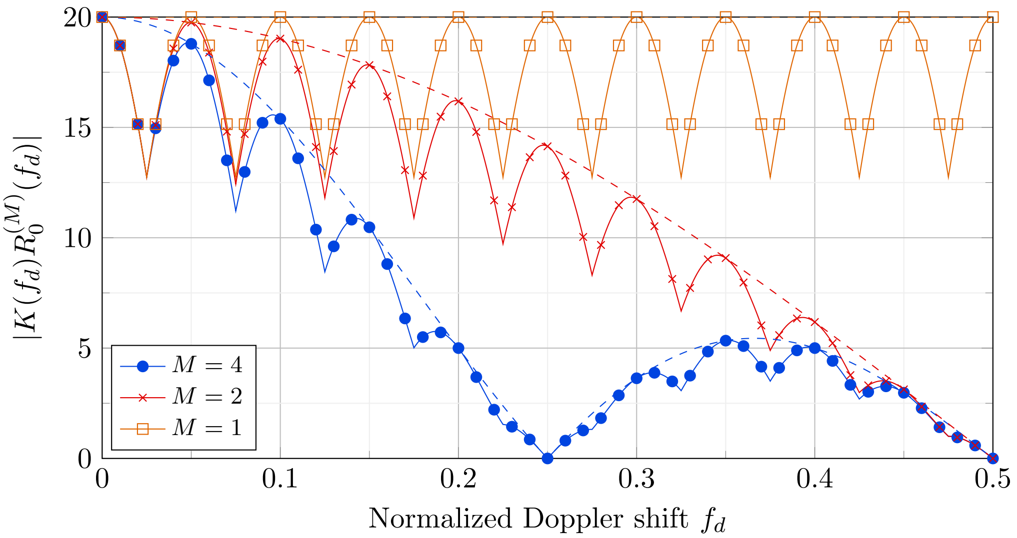

Figure 4.5.: Comparison of the swiveled correlator output for different subsequence lengths. A preamble length of $K = 20$ symbols was used. The dashed curves represent the envelope of the plots and correspond to the influence of $R_0^{(M)}(f_d)$.

separate branch. Therefore, this configuration does not suffer from noncoherent correlation loss, which is indicated in the figure by a corresponding constant envelope. The decay of $R_0$ is fairly moderate for small frequency shifts, which indicates that in scenarios with small maximum frequency shifts, the subsequences can be chosen to be longer. This corresponds to a smaller number of branches $N$ and therefore lower complexity. However, in this thesis the focus is on large frequency shifts, for which reason only the case of $N = K$ will be practical. A similar conclusion about the maximum length of the subsequence to reduce correlation losses is found in [CPV06], where a design rule for the maximum subsequence length depending on the frequency offset is derived. Although this rule is only valid for small Doppler shifts, it supports the idea of operating with very short subsequences for large Doppler shifts.

Additionally to the noncoherent correlation loss, it can be seen that the output dips quite significantly in between two adjacent bins. This is the effect of $K_0(f_d)$ and is due to the discreteness of the FFT and the finite number of input samples. If the Doppler shift of the input sequence does not coincide exactly with the center frequency of a bin of the FFT, then some of the energy will be contained in other bins. The effect is most prominent in the middle of two adjacent frequencies, where the energy is equally shared between the two bins. In literature, the difference between the maximum output and the minimum output is also referred to as the scalloping loss. A common method to counteract scalloping loss and increase the minimum output of the FFT is zero-padding, which will now be more closely discussed.

### 4.3.2. Zero-Padding

Zero-padding can help to improve the performance of the FFT by interpolating between the FFT bins and therefore effectively adding more bins in the same frequency range. To analyze the benefit of zero-padding we perform the same discussion for the output of the swiveled correlator again, this time assuming that the $N$ branch outputs will be fed into the FFT together with a padding of $Z$ zeros. A characteristic of the FFT is that it produces as many output bins as it is given input bins, in this case it will be $N+Z$, and therefore $i \in \{1, N+Z\}$. The output of the $i$-th bin can now be computed with

$$v_i[\mu] = \sum_{n=1}^{N+Z} w_n[\mu]\, e^{-j2\pi \frac{n}{N+Z} i}. \tag{4.21}$$

Given that $w_n[\mu] = 0$, for all $n > N$, we can adjust the limit of the sum to

$$v_i[\mu] = \sum_{n=1}^{N} w_n[\mu]\, e^{-j2\pi \frac{n}{N+Z} i}. \tag{4.22}$$

Therefore, the likelihood function of the swiveled correlator can be generalized to

$$L_{\mathrm{S}}(\mu) = \max_i \left( \left| \sum_{n=1}^{N} \sum_{k=(n-1)M}^{nM-1} r[\mu+k]\, c^*[k]\, e^{-j2\pi \frac{n}{N+Z} i} \right| \right), \quad i \in \{1, N+Z\}. \tag{4.23}$$

Considering a fully contained preamble and following a similar evaluation as for the discussion without zero-padding, we can express the expected output of the zero-padded swiveled correlator in a noiseless scenario by

$$\begin{aligned} |K_Z(f_d) R_0^{(M)}(f_d)| &= |R_0^{(M)}(f_d)| \max_i(|K_{Z,i}(f_d)|) \\ &= |R_0^{(M)}(f_d)| \max_i \left( \left| \frac{\sin(\pi N(f_d M - \frac{i}{N+Z}))}{\sin(\pi(f_d M - \frac{i}{N+Z}))} \right| \right). \end{aligned} \tag{4.24}$$

In order to show the benefit of zero-padding, we compare the two approaches in Figure 4.6. The dashed curves show the expected output for different subsequent lengths without zero-padding. Here, the scalloping loss is very dominant. The effect of zero-padding can be seen by comparing the dashed curves to the solid curves, which employ a zero-padding ratio $\frac{Z}{N} = 2$. It can clearly be seen that the dips between adjacent peaks are much less

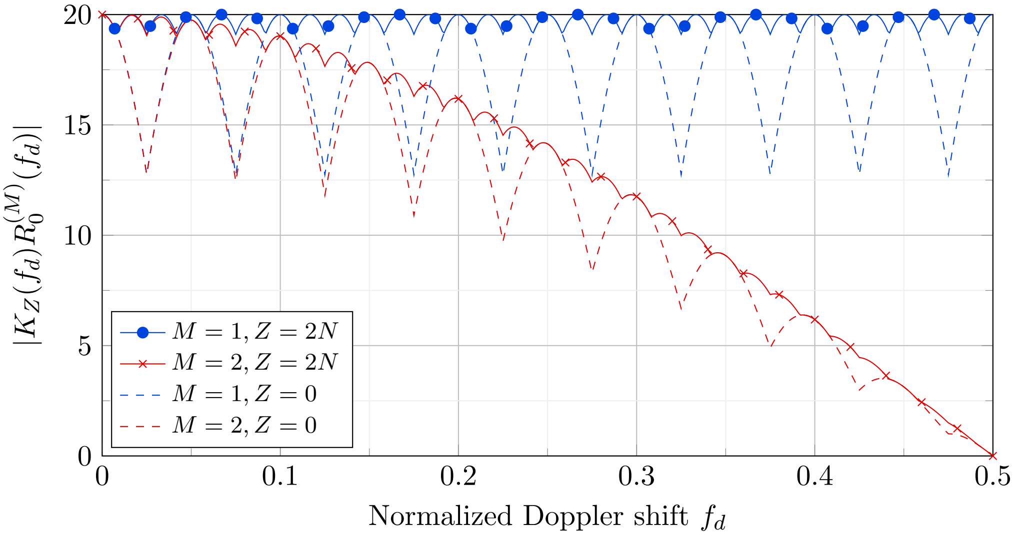

Figure 4.6.: Comparison of the effect of zero-padding on the swiveled correlator output. The assumed preamble length is $K = 20$. A comparison is performed for two different number of branches, $N = 20$ and $N = 10$.

severe and that therefore the scalloping loss is much smaller. To establish how many zeros should be added as a tradeoff between performance and complexity, an expression of the normalized scalloping loss depending on the amount of zeros can be found:

$$S_L(Z) = \max(K_Z) - \min(K_Z) = 1 - \frac{1}{N}\frac{\sin(\frac{N\pi}{2(N+Z)})}{\sin(\frac{\pi}{2(N+Z)})}. \tag{4.25}$$

As it is not immediately visible from the equation how the scalloping loss behaves for different amounts of zero-padding, we can try to find a polynomial approximation using the Taylor expansion of the sine-function. The first order approximation evaluates to zero, for which reason a meaningful estimate is given by the second order approximation:

$$S_L^{(2)}(Z) = \pi^2 \frac{1 - N^2}{\pi^2 - 24(N+Z)^2}. \tag{4.26}$$

Assuming a fixed number of branches $N$, it can be seen that the second order approximation is reciprocal with respect to $Z$. Therefore, it can be stated that the initial gain of adding several zeros has a large effect, however, by further increasing $Z$ the benefit becomes smaller and smaller. The effect is depicted in Figure 4.7, which shows the exact expression of the scalloping loss and the second order taylor expansion.

It can be seen that there is still a slight gap between the exact expression and the second order approximation for small amounts of zero-padding, whereas it becomes closer for

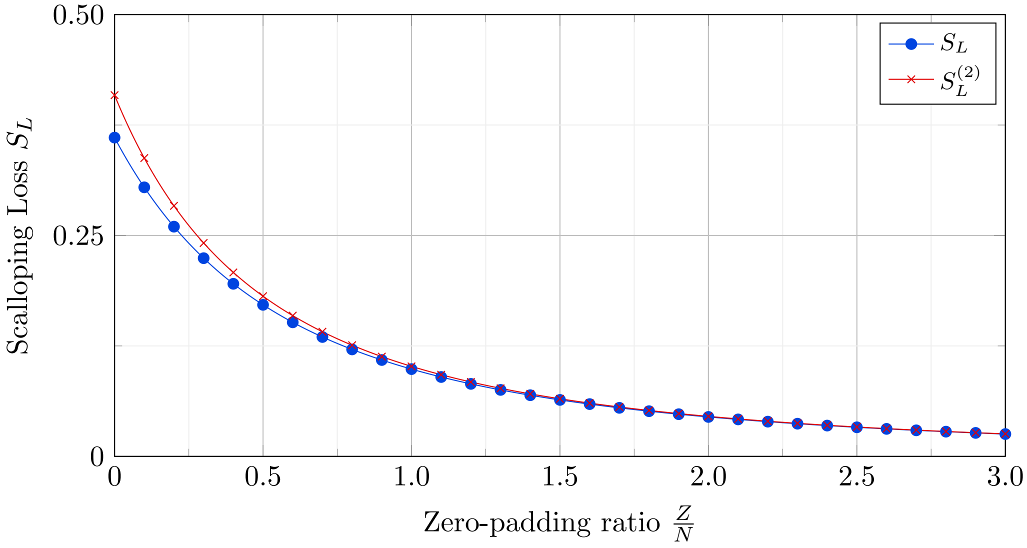

Figure 4.7.: Behavior of scalloping loss for different amounts of zero-padding.

higher zero-padding ratios $\frac{Z}{N}$. Given the reciprocal shape, it becomes clear that the scalloping loss cannot be eliminated, as was possible for the noncoherent correlation loss by choosing $M = 1$, but it can be reduced very effectively. As zero-padding can be implemented very efficiently [AML05] and therefore does not cause a large increase in complexity, for the remainder of the thesis we assume a zero-padding factor $\frac{Z}{N} = 3$. The scalloping loss then resolves to less then 3 % of the amplitude of the output of the swiveled correlator and even larger zero-padding ratios only provide minor improvement.

## 4.4. Second-order Approximation of the Optimal Detector

Another different approach was already mentioned in Chapter 3 and involves the approximation of the optimal LRT to make it implementable. In contrast to the previously presented schemes, this approach is not initially based on a correlation of the incoming signal with a preamble, but it is derived from the optimal decision rule. This idea was presented in [WRKH18] and showed a close to optimal performance in the analyzed setting, i.e., the performance loss to the optimal LRT was very small. It was found that the improvement of approximations higher than the second order is very little and therefore the second order approximation is a good tradeoff between performance and complexity. In this section we will therefore present this second order approximation and extend the expression to account for arbitrary maximum Doppler shifts $f_{\max}$. We will then also extend the analysis made in [WRKH18] to other scenarios later in this chapter.

Similar to the derivation of the optimal LRT, the derivation of a simplified, closed-form expression of the second order approximation is quite elaborate and therefore presented in Appendix A.2. For a general maximum Doppler shift $f_{\max}$ we have

$$\begin{aligned}L_{\mathrm{A}}(\mu) = \sum_{k_1=0}^{K-1}\sum_{l_1=0}^{K-1}\sum_{k_2=0}^{K-1}\sum_{l_2=0}^{K-1} & r[\mu+k_1]\ r^*[\mu+l_1]\ c^*[k_1]\ c[l_1] \\ & \cdot r[\mu+k_2]\ r^*[\mu+l_2]\ c^*[k_2]\ c[l_2]\ \mathrm{sinc}\left(2f_{\max}\left(k_1-l_1+k_2-l_2\right)\right). \end{aligned} \tag{4.27}$$

When the maximum Doppler shift is fixed to $f_{\max} = 0.5$, a much simpler expression can be found, since the sinc-function simplifies to the Dirac-delta function for integers $k$:

$$\mathrm{sinc}(k) = \delta[k], \quad \text{for all } k \in \mathbb{Z}. \tag{4.28}$$

Since this only has nonzero contribution for $k \neq 0$, several terms drop out and [WRKH18] shows that $L_{\mathrm{A}}(\mu)$ can be simplified to

$$L_{\mathrm{A}}(\mu) = \sum_{m=1}^{K-1}\left|\sum_{k=m}^{K-1} r^*[\mu+k]\,c[k]\,r[\mu+k-m]\,c^*[k-m]\right|^2. \tag{4.29}$$

Hereby, the inner sum is also referred to as the double correlation of lag $m$ in literature. Therefore, $L_{\mathrm{A}}(\mu)$ corresponds to the sum of the absolute square of all possible double correlations with lag $m$. For simplicity, we will also refer to this detection scheme as the double correlator.

## 4.5. Choi-Lee Detector

A very similar detection scheme was presented in [CL02]. It was shown that the derived metric performs well in scenarios with moderate frequency offsets and phase uncertainty. Although the detector was derived in an ML framework, the metric was shown to also perform well when used for hypothesis testing [WRKH18]. It has since been widely used as a reference in literature [Chi10],[WRKH17],[PVVC$^+$10]. The metric is given as:

$$\begin{aligned}L_{\mathrm{CL}}(\mu) = \sum_{m=1}^{K-1}\Bigg\{ & \left|\sum_{k=m}^{K-1} r^*[\mu+k]\,c[k]\,r[\mu+k-m]\,c^*[k-m]\right|^2 \\ & - \sum_{k=m}^{K-1} |r[\mu+k]|^2 |r[\mu+k-m]|^2 \Bigg\}. \end{aligned} \tag{4.30}$$

The first part hereby corresponds to $L_{\mathrm{A}}(\mu)$ and therefore the double correlation, and the second part is an energy, or data, correction term. This detector was derived for a continuous transmission of periodic frames, so the data correction term is supposed to reduce the influence of random data or partially contained preambles on the false alarm rate. Although we disregarded these cases for the derivation of the optimal LRT, we will later simulate the approaches considering partially contained preambles to review the validity of our assumption.

## 4.6. Comparison and Simulation Results

### 4.6.1. Means of Comparison

In order to compare the presented algorithms, we want to emphasize the employed metrics and methods. In the given setting, the most prominent metrics are the probability of false alarm $P_{\mathrm{fa}}$ and the probability of correct detection $P_{\mathrm{d}}$ or missed detection $P_{\mathrm{m}}$. In the hypothesis testing framework, these depend on the employed threshold $\lambda$ and therefore offer a tradeoff, where increasing the threshold leads to an increase in $P_{\mathrm{fa}}$ and $P_{\mathrm{d}}$, and vice versa. $P_{\mathrm{fa}}$ is defined as the probability that hypothesis $\mathcal{H}_1$ was chosen although $\mathcal{H}_0$ was true, i.e.,

$$P_{\mathrm{fa}} = \Pr\Big[\mathcal{D}_1 | \mathcal{H}_0\Big]. \tag{4.31}$$

As discussed, when employing hypothesis testing the hypothesis $\mathcal{H}_1$ is chosen if the output of the likelihood function $L(\mu)$ surpasses the threshold $\lambda$. Therefore, the equation can be rewritten as

$$P_{\mathrm{fa}} = \Pr\Big[L(\mu) > \lambda | \mathcal{H}_0\Big]. \tag{4.32}$$

Likewise, the probability of missed detection $P_{\mathrm{m}}$ corresponds to choosing hypothesis $\mathcal{H}_0$ when $\mathcal{H}_1$ is true, where $\mathcal{H}_0$ is chosen if the threshold is not exceeded:

$$P_{\mathrm{m}} = \Pr\Big[\mathcal{D}_0 | \mathcal{H}_1\Big] = \Pr\Big[L(\mu) < \lambda | \mathcal{H}_1\Big]. \tag{4.33}$$

As a correct detection is the complementary event to a missed detection, the probability of correct detection can be defined as

$$P_{\mathrm{d}} = 1 - P_{\mathrm{m}} = \Pr\Big[\mathcal{D}_1 | \mathcal{H}_1\Big] = \Pr\Big[L(\mu) > \lambda | \mathcal{H}_1\Big]. \tag{4.34}$$

It corresponds to making the correct decision of choosing $\mathcal{H}_1$ when $\mathcal{H}_1$ holds true.

A very meaningful figure of merit to compare the algorithms in the hypothesis testing framework is the receiver operating characteristic (ROC) curve, which is widely used in literature [Chi10]. Hereby, the algorithms are evaluated with different thresholds $\lambda$, which lead to different combinations of $P_{\mathrm{fa}}$ and $P_{\mathrm{d}}$ or $P_{\mathrm{m}}$. These can then be plotted to obtain a curve, which shows all operating points of the algorithm in the given scenario. Depending on the required $P_{\mathrm{d}}$ and on the available resources, a certain threshold matching the requirements can then be chosen.

### 4.6.2. Discussion

To compare the algorithms, we carried out several simulations in different scenarios. The interesting factors include the behavior of the different detectors in high and low SNR and the performance in differently strong Doppler shifts. Furthermore, we want to verify the validity of the assumption made in the beginning of Chapter 3 to only consider fully contained preambles and treat incoming signals with partially contained preambles the same way as pure noise.

#### Simulation notes

In general, the two hypotheses and therefore $P_{\mathrm{fa}}$ and $P_{\mathrm{d}}$ can be simulated separately. For $\mathcal{H}_0$, a stream of noise was supplied to the detection schemes and averaged over a sufficient amount of iterations. For $\mathcal{H}_1$, uniformly random Doppler shifts and noise were applied to the preamble, before being passed to the detectors and averaged. Hereby, only the central sample of the correlation output will be analyzed, since we disregard cases with partially contained preambles. However, we will later provide simulations taking also such cases into account, which will give insight on the validity of this assumption.

For the simulation of the optimal LRT, we used Monte Carlo integration to integrate the output of the Bessel function over the frequency. For both the bank of correlators and the swiveled correlator, we want to use their ability to also estimate the experienced Doppler shift and only accept a correct detection if both the sample and the frequency were identified correctly. Because frequency shifts that lie towards the middle of two branches/bins will cause a similarly large output in both, we choose to soften the rule of correct detection to also accept directly adjacent branches/bins [2]. Therefore, the estimation of the Doppler shift in this setup has a maximum error of $3\Delta f$. Using this frequency estimation slightly decreases the performance of the two algorithms and therefore a comparison to other detectors that do not perform Doppler estimation might not be entirely fair. However, producing a reliable Doppler estimation can be very helpful, as will be further clarified in the second part of the thesis.

---

[2] In practice, depending on the frequency resolution of the algorithms and the requirements of the application, even more than one adjacent branch/bin will often be accepted, as this increases the performance of detection and still provides a good enough Doppler estimation.

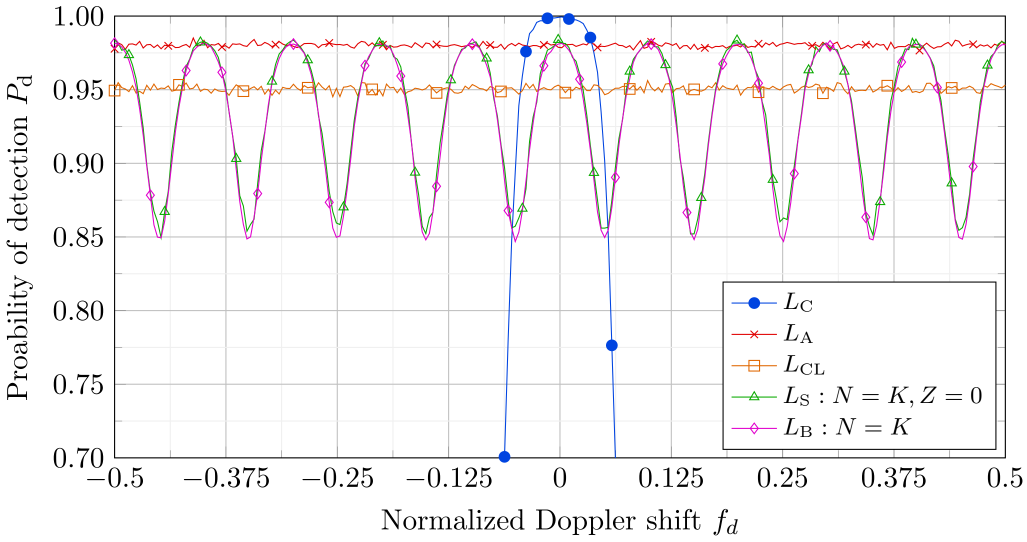

Figure 4.8.: Comparison of the detection performance across the normalized frequency offset in a high SNR scenario. $\frac{E_S}{N_0} = 1\,\text{dB}$, $K = 10$, $P_{\text{fa}} = 10^{-1} \pm 10^{-3}$.

### Performance across Doppler range

To confirm the expected behavior of the different algorithms in varying Doppler shifts with simulations, Figure 4.8 plots the detection performance against the frequency offset for an SNR of $\frac{E_S}{N_0} = 1\,\text{dB}$, a preamble length of $K = 10$ symbols and a probability of false alarm of $P_{\text{fa}} = 10^{-1} \pm 10^{-3}$. The parameters were chosen in a way to effectively visualize the behavior of the detection schemes. It shows the expected degradation of the simple correlator $L_C$ with larger frequencies, resembling the shape of $R_0(f_d)$. The bank of correlators $L_B$ uses several branches with this behavior at different frequencies and by choosing the one with the highest output, the performance shows a characteristic sine-shape. The same behavior can be seen for the swiveled correlator $L_S$, where the behavior comes from the scalloping loss of the FFT . Hereby, the length of the subsequence was chosen to $M = 1$. For longer subsequences, the swiveled correlator would show a stronger degradation towards larger frequencies, similar to the behavior in Figure 4.5. It is also notable that the performance of the bank of correlators and the swiveled correlator would greatly improve when using more resources, i.e., a larger number of branches for the bank of correlators or zero-padding for the swiveled correlator. We refrain from doing so for this figure in order to present the sinusoidal behavior. Finally, it can be seen that the approximation $L_A$ of the optimal LRT and the Choi-Lee detector $L_{CL}$ show a constant performance across all frequency shifts.

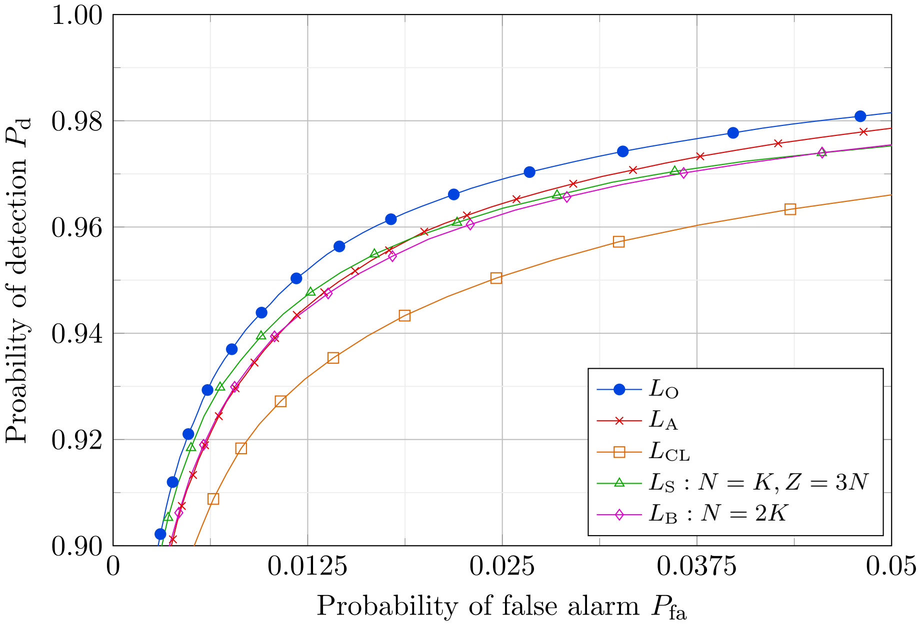

Figure 4.9.: Simulated ROC at high SNR. $\frac{E_S}{N_0} = 0\,\text{dB}$, $K = 15$, $f_{\max} = 0.5$.

### High SNR

For a first comparison of the different algorithms concerning their performance, we choose a high SNR environment, where short preambles can be used. The result of the simulation can be found in Figure 4.9, which shows the ROC curves of the detectors. It can be seen that the optimal LRT $L_O$, derived in Section 3.2, gives an upper bound on the performance of the other detection schemes, which confirms that it corresponds to the optimal decision rule. The second order approximation $L_A$, derived in Section 4.4, is very tight in this scenario and comes very close to the performance of the optimal test. Similarly the bank of correlators and the swiveled correlator with the given specifications show the same performance. The Choi-Lee detector $L_{CL}$ performs slightly worse, which can be attributed to the energy correction term. This is subtracted from the double correlation and therefore reduces the output, which slightly decreases the performance in this scenario.

### Low SNR

Concerning an application in IoT via satellite, a low SNR scenario may be more fitting as a basis for comparison, since satellite links are typically characterized by a low SNR. The effect of a lower SNR while employing a preamble of the same length as in the high SNR case is shown by the simulated ROC curves in Figure 4.10. Hereby, the performance of

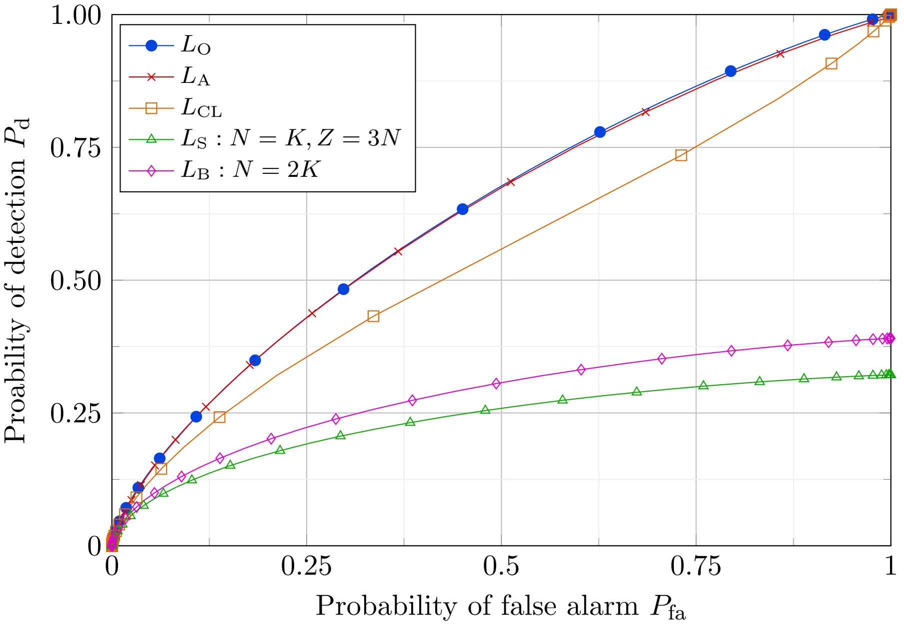

Figure 4.10.: Simulated ROC at low SNR with short preambles. $\frac{E_S}{N_0} = -9\,\mathrm{dB}$, $K = 15$, $f_\mathrm{max} = 0.5$.

all detectors drastically decreases, because the correlation output of the short preamble cannot be detected over the larger amount of noise. This emphasizes the argument discussed in Section 4.1, that in lower SNR environments, longer preambles have to be used, which leads to a shorter bandwidth of the correlation. At first glance, it is counterintuitive that the bank of correlators and the swiveled correlator do not reach a detection probability of 100 % for a false alarm probability of 100 %, but this is inflicted by additionally requiring a correct frequency estimation. Therefore, even if the threshold is set very low and all output branches would exceed the threshold, it is very unlikely that the correct branch has the highest output, which only then would be accepted as a correct detection.

Therefore, to account for the lower SNR, the preamble length needs to be increased if one wishes to detect the preamble with high probability. Figure 4.11 includes the ROC curves of the analyzed detectors in a low SNR scenario with a longer preamble. The optimal LRT again provides the best possible performance. However, its approximation $L_\mathrm{A}$ shows a large degradation compared to the high SNR scenario. While at high SNR the performance of $L_\mathrm{A}$ was very close to the optimal LRT and on a par with both the bank of correlators and the swiveled correlator, it performs even worse than the Choi-Lee correlator at low SNR. Also the performance disparity between the Choi-Lee correlator and the optimal LRT increases, while the bank of correlators and the swiveled correlator

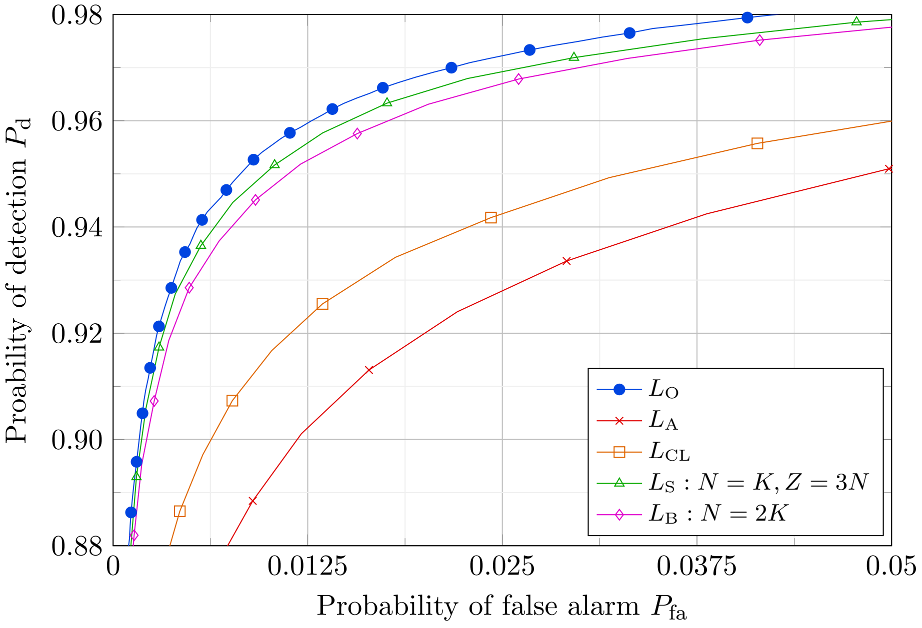

Figure 4.11.: Simulated ROC at low SNR. $\frac{E_S}{N_0} = -9\,\text{dB}$, $K = 150$, $f_{\max} = 0.5$.

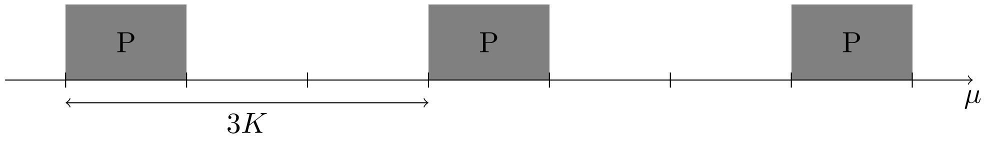

Figure 4.12.: Visualization of signal stream for the simulations considering partially contained preambles. A preamble was inserted every $3K$ symbols.

remain very close. We believe that the bad performance of the $L_A$ detector can be attributed to the approximation of the Bessel function. As this has not been observed before in literature, it deserves further attention and a precise explanation is subject to further investigation.

### Considering partially contained preambles

In a further simulation we want to examine the effect of including cases with partially contained preambles. Throughout the discussion of the detectors in this Chapter, we assumed that the ACF of the preamble was very good and therefore incoming signals with partially contained preambles were treated the same way as pure noise. The simulation now reveals whether this assumption was justified. For this, the probability of false alarm and probability of detection are simulated together, by creating a stream of noise and embedding preambles every $3K$ symbols, as illustrated in Figure 4.12. The stream is then

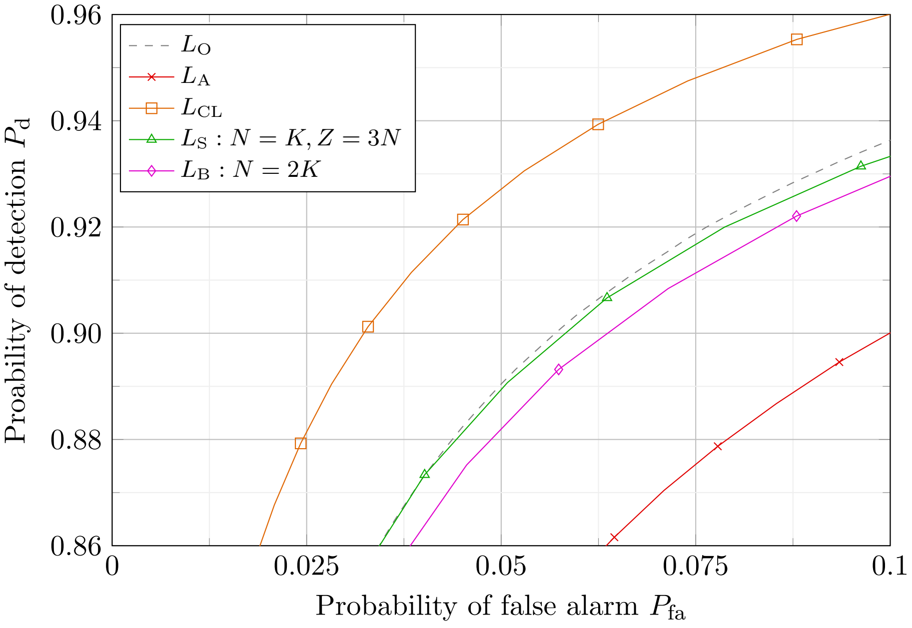

Figure 4.13.: Simulated ROC at high SNR considering partially contained preambles. $\frac{E_S}{N_0} = 0\,\mathrm{dB}$, $K = 15$, $f_{\max} = 0.5$.

passed through the detectors and correct detections and false alarms are averaged. The result is presented in Figure 4.13.

It is essential to point out that cases with partially contained preambles were disregarded in the derivation of the optimal LRT, for which reason the $L_O$ metric will not be optimal in this setting, and therefore may not be viewed as an upper bound. For this reason the curve is shown dashed. Nonetheless, we include it in the plot to see the effect of partially contained preambles and the assumption of disregarding them. Looking at the curves, it becomes apparent that all of the schemes lose in performance, indicating that partially contained preambles induce a higher probability of false alarm. It therefore may be worthwhile to consider partially contained preambles in the derivation of a modified optimal LRT for the given scenario in the future, at least for high SNR. It is notable that the performance of the Choi-Lee correlator suffers the least degradation. This is due to the energy correcting second term in the metric given in Equation (4.30). The increased probability of false alarm for the other schemes, comes from an increase in the energy of the incoming signal, due to the partially contained preamble. This increase in energy is countered by the energy correcting term of the Choi-Lee correlator, enhancing its performance with respect to the other detectors.

The simulation in a low SNR environment is given in Figure 4.14. The biggest difference to the high SNR case can be seen for the Choi-Lee correlator, which significantly drops

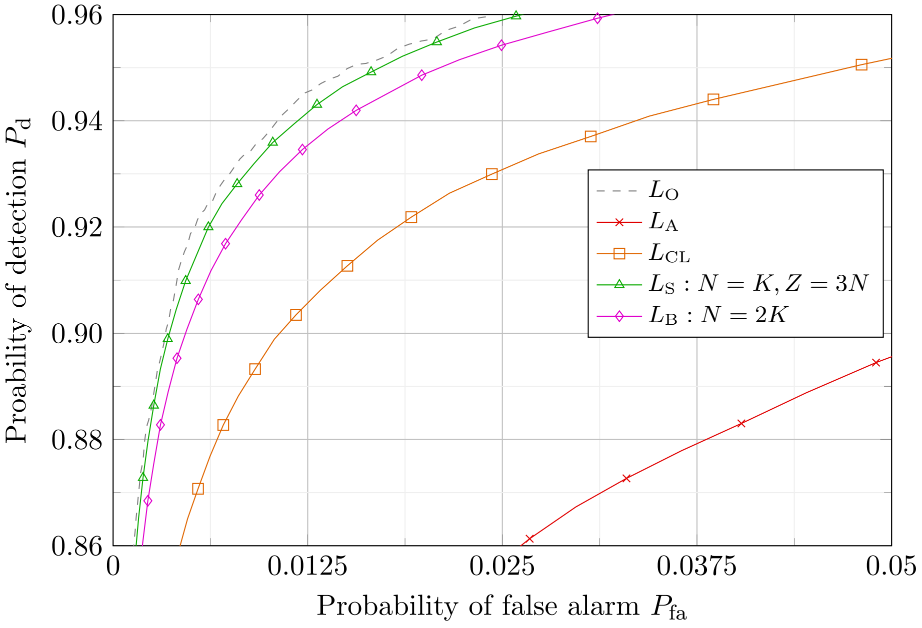

Figure 4.14.: Simulated ROC at low SNR considering partially contained preambles. $\frac{E_S}{N_0} = -9\,\mathrm{dB}$, $K = 150$, $f_\mathrm{max} = 0.5$.

in performance compared to the other schemes. The good performance at high SNR was due to the compensation of the signal energy. As the SNR is defined as the signal energy with respect to the noise energy, this compensation has a much smaller effect when the incoming signal is dominated by the noise. This is also emphasized by the correlation output, which, according to $R_0$, increases with growing preamble length and therefore causes for a much larger contribution than the signal energy on its own. This also explains why the performance loss of the other detectors, including the optimal LRT, is much smaller when comparing the low SNR scenarios with and without considering partially contained preambles to the high SNR equivalents. This suggests that the assumption of $\mathcal{H}_0$ subsuming cases with partially contained preambles is much more accurate for low SNR scenarios and therefore validates the assumption in the given satellite setting.

## 4.7. Summary

The considered detectors all showed close to optimal performance in a high SNR scenario, when disregarding partially contained preambles. It was shown that the bank of correlators and the swiveled correlator come very close to the optimal LRT in all scenarios, i.e., both high and low SNR and both with and without considering partially contained preambles, and therefore represent promising solutions. The approximation $L_\mathrm{A}$ of the optimal LRT significantly drops in performance when considering low SNR scenarios. The Choi-Lee correlator shows better results in a scenario with high SNR and considering partially contained preambles due to the energy correcting term, however, this benefit disappears for long preambles and low SNRs. Therefore, in the given satellite setting, which is characterized by low SNRs and long preambles, our experimental results show that the bank of correlators and the swiveled correlator outperform the other detectors, approaching the performance the optimal LRT.

# 5. Analytic Modeling of Correlation-based Algorithms

Additionally to the analysis of the output of the simple correlator, the bank of correlators and the swiveled correlator presented in Chapter 4, it is useful to derive models for the probability of false alarm, $P_{\mathrm{fa}}$, and the probability of correct detection, $P_{\mathrm{d}}$, in order to estimate and predict the performance of the mentioned algorithms in different scenarios. For this, the deterministic analysis of the expected output has to be complemented by a statistical discussion of the noise throughout the processing steps. For the simplified baseband representation assumed in the first part of this thesis, this discussion is known in literature, e.g. for the swiveled correlator in [SSS$^+$00]. Nonetheless, we present it as a basis for the later extension of the models accounting for ISI, which is novel.

## 5.1. Simple Correlator

### Probability of false alarm $P_{\mathrm{fa}}$

As mentioned in the previous chapter, we characterize a false alarm as the selection of hypothesis $\mathcal{H}_1$ although $\mathcal{H}_0$ was true. In the binary hypothesis testing framework, this means that the probability of false alarm is solely characterized by the noise:

$$r[\mu + k] = n[\mu + k]. \tag{5.1}$$

Recall that $n[\mu{+}k]$ is a circularly symmetric complex Gaussian RV, where each component has zero mean and a variance of $\sigma_n^2$. Hence, we have

$$\mathrm{Re}\,(n[\mu + k]) \sim \mathcal{N}(0, \sigma_n^2), \qquad \mathrm{Im}\,(n[\mu + k]) \sim \mathcal{N}(0, \sigma_n^2). \tag{5.2}$$

The output of the correlation is given as

$$w[\mu] = \sum_{k=0}^{K-1} n[\mu + k]\, c^*[k]. \tag{5.3}$$

Since we assume unit energy PSK symbols, i.e., $|c[k]|^2 = 1$, the correlation corresponds to the sum of $K$ complex Gaussian RVs. We can then use the linearity of expectation, which always holds, and the linearity of variance, which holds for uncorrelated RVs. For two RVs $X_i$ and $X_j$, this is formally described by

$$\begin{aligned} \mathrm{E}\Big[\sum_i X_i\Big] &= \sum_i \mathrm{E}[X_i] \\ \text{and} \quad \mathrm{Var}\Big[\sum_i X_i\Big] &= \sum_i \mathrm{Var}[X_i] + 2\sum_{\substack{i,j\\ i<j}} \mathrm{Cov}[X_i, X_j], \\ \text{where} \quad \mathrm{Cov}[X_i, X_j] &= 0, \quad \text{if } X_i \text{ and } X_j \text{ are uncorrelated.} \end{aligned} \tag{5.4}$$

We know that the RVs of $n[\mu + k]$ are i.i.d., and therefore, using the property that independent RVs are also uncorrelated, we have that $w[\mu]$ is a circularly symmetric Gaussian RV with per component variance $K\sigma_n^2$. The final processing step of the simple correlator is to then take the absolute value of the correlation output, i.e., $|w[\mu]|$. The absolute value of a circularly symmetric Gaussian random variable with zero mean and per component variance of $\sigma^2$ follows a Rayleigh distribution with scale parameter $\sigma$ [PP02]. Hence, we have

$$|w[\mu]| \sim \mathrm{Rayleigh}(\sqrt{K\sigma_n^2}). \tag{5.5}$$

For a Rayleigh distributed RV $x$, its PDF is given by

$$f_X(x) = \frac{x}{K\sigma_n^2}\, e^{-\frac{x^2}{2K\sigma_n^2}}. \tag{5.6}$$

The corresponding cumulative density function (CDF) is

$$F_X(x) = 1 - e^{-\frac{x^2}{2K\sigma_n^2}}. \tag{5.7}$$

An expression for the probability of false alarm can now be computed as the probability that the Rayleigh distributed output is larger than the previously defined threshold $\lambda$:

$$P_{\mathrm{fa}}(\lambda) = \Pr\Big[|w[\mu]| > \lambda\Big] = 1 - \Pr\Big[|w[\mu]| \leq \lambda\Big] = 1 - F_{\mathrm{Rayleigh}}(\lambda) = e^{-\frac{\lambda^2}{2K\sigma_n^2}}. \tag{5.8}$$

### Probability of correct detection $P_{\mathrm{d}}$

For the probability of correct detection, we analyze the hypothesis $\mathcal{H}_1$. In this case, we know from Equation (4.2) that the output is given as

$$w[0] = R_0(f_d) + \sum_{k=0}^{K-1} n[k]\, c^*[k]. \tag{5.9}$$

Hereby, we have already established above that the second term is a circularly symmetric Gaussian RV with zero mean and a per component variance of $K\sigma_n^2$. The first term is deterministic, i.e., it has zero variance. Using the rules given in (5.4), we get that $w[0]$ is a circularly symmetric Gaussian RV with mean $\mathrm{E}[w[0]] = R_0(f_d)$ and per component variance of $K\sigma_n^2$. We know that the absolute value of such a RV follows a Rice distribution [JBS06]:

$$|w[0]| \sim \mathrm{Rice}(s, \sqrt{K\sigma_n^2}), \quad \text{where } s(f_d) = |R_0(f_d)|. \tag{5.10}$$

The PDF of such a Rice distributed RV $x$ is given by

$$f_X(x) = \frac{x}{K\sigma_n^2}\, e^{-\frac{x^2+s^2(f_d)}{2K\sigma_n^2}}\, I_0\left(\frac{xs(f_d)}{K\sigma_n^2}\right). \tag{5.11}$$

The probability of correct detection can then be obtained by the probability that the Rice distributed output exceeds the threshold $\lambda$:

$$P_{\mathrm{d}}(\lambda) = \Pr\Big[|w[0]| > \lambda\Big] = \int_{\lambda}^{\infty} \frac{x}{K\sigma_n^2}\, e^{-\frac{x^2+s^2(f_d)}{2K\sigma_n^2}}\, I_0\left(\frac{xs(f_d)}{K\sigma_n^2}\right) dx. \tag{5.12}$$

## 5.2. Bank of Correlators

### Probability of false alarm $P_{\mathrm{fa}}$

The bank of correlators employs $N$ parallel branches with simple correlators operating at different center frequencies. From Section 5.1 we know that the outputs $|w_i[\mu]|$ of each branch are Rayleigh distributed with scale parameter $\sqrt{K\sigma_n^2}$. The algorithm then selects the maximum of those branches. The probability of false alarm is then given as the probability that the maximum of $N$ Rayleigh distributed RVs exceeds the threshold:

$$\begin{aligned} P_{\mathrm{fa}}(\lambda) &= \Pr\Big[\max_i(|w_i[\mu]|) > \lambda\Big] = \Pr\Big[|w_1[\mu]| > \lambda, |w_2[\mu]| > \lambda, ..., |w_N[\mu]| > \lambda\Big] \\ &= 1 - \Pr\Big[|w_1[\mu]| \le \lambda, |w_2[\mu]| \le \lambda, ..., |w_N[\mu]| \le \lambda\Big]. \end{aligned} \tag{5.13}$$

As a simplifying assumption, we can treat the different RVs as independent. This is generally not the case, since the outputs of the branches are all characterized by the same input noise realization and only differ in the applied frequency shift. Intuitively, the smaller this frequency shift becomes, the more dependent are the outputs of the adjacent branches. In the case of infinitely many branches and therefore infinitely small frequency differences, adjacent branches will be the same. The tightness of the approximation for a moderate amount of branches will be numerically analyzed later. Assuming the RVs are independent, the probability that no RV exceeds the threshold is equal to the product of the probabilities that each RV does not exceed the threshold. Additionally, the RVs are identically distributed, which lets us simplify the expression to

$$P_{\text{fa}}(\lambda) \approx 1 - \prod_{i=1}^{N} \Pr\Big[|w_i[\mu]| < \lambda\Big] = 1 - \left(F_{\text{Rayleigh}}(\lambda)\right)^N \overset{(5.7)}{=} 1 - \left(1 - e^{-\frac{\lambda^2}{2K\sigma_n^2}}\right)^N . \quad (5.14)$$

**Probability of correct detection $P_{\mathbf{d}}$**

Regarding the probability of correct detection, we again have to consider the signal content and noise. In contrast to the simple correlator, the bank of correlators can provide an estimate of the Doppler shift $\tilde{f}_d$, which can be used for the correction and further processing of the packet. Since this is very useful, we want to ensure a reliable Doppler estimation and therefore assume that a detection is only made correctly, if both the correct (time) sample and the correct (frequency) branch exceeded the threshold. Following the analysis of the simple correlator, it is intuitive that the correlation is likely to be highest in the branch with the frequency shift closest to the Doppler shift, however the effects of noise could lead to a wrongly estimated frequency. We can again use the results from Section 5.1 and establish that the output $|w_i[0]|$ of each branch is Rice distributed with parameters $s(f_d - i\Delta f)$ and $\sqrt{K\sigma_n^2}$. Hereby, the Rice parameter is modified by the center frequency of the branch.

A correct detection is made if the following two properties hold:

1) The output of the correct branch exceeds the threshold $\lambda$ to trigger the detection.

2) The output of the correct branch is larger than the output of all other $N-1$ branches to give a correct frequency estimation.

The second statement is equivalent to the correct branch being larger than the maximum of the other branches. Let us now assume that the $i$-th branch is the correct one, i.e., the one whose center frequency is closest to $f_d$, and denote its output with $x$. Recall that we defined the residual frequency offset in this branch as $f_r$ in Section 4.2. Therefore, we have that $x$ is Rice distributed with parameters $s(f_r)$ and $\sqrt{K\sigma_n^2}$. Furthermore, we denote the maximum output of the incorrect branches with $y$, which gives

$$x = |w_i[0]|, \qquad y = \max_{j \neq i}(|w_j[0]|). \tag{5.15}$$

We can now formally describe the probability of correct detection as

$$P_\mathrm{d}(\lambda) = \Pr\Big[x > \lambda, x > y\Big] = \int\limits_{\lambda}^{\infty} \int\limits_{0}^{x} f_{X,Y}(x, y)\, dy\, dx, \tag{5.16}$$

where $f_{X,Y}$ is the joint probability distribution of $X$ and $Y$. However, this is not available to us and we will therefore make some assumptions to derive an approximation. Due to the fast decay of the correlation output $R_0(f_d)$ (contained in the Rice factor), we can assume that the incorrect branches experience a very small correlation output. Therefore, we will approximate them as $(N-1)$ i.i.d. Rayleigh distributed RVs, which yields

$$F_Y(y) = \Pr\Big[Y < y\Big] = \left(1 - e^{-\frac{y^2}{2K\sigma_n^2}}\right)^{N-1}. \tag{5.17}$$

We will further approximate that $x$ and $y$ are independent, so that the joint probability distributions corresponds to the product of the distributions of each RV. The following then gives the formal derivation of an approximation of the probability of correct detection:

$$\begin{aligned} P_\mathrm{d}(\lambda) &\approx \int\limits_{\lambda}^{\infty} \int\limits_{0}^{x} f_Y(y) dy \; f_X(x) dx = \int\limits_{\lambda}^{\infty} F_Y(x) f_X(x) dx \\ &= \int\limits_{\lambda}^{\infty} \left(1 - e^{-\frac{x^2}{2K\sigma_n^2}}\right)^{N-1} \frac{x}{K\sigma_n^2} e^{-\frac{x^2+s^2(f_r)}{2K\sigma_n^2}} I_0\left(\frac{xs(f_r)}{K\sigma_n^2}\right) dx. \end{aligned} \tag{5.18}$$

It is notable that this approximation only holds for a moderate amount of branches for two reasons:

1) With this approximation only the correct branch is allowed to operate inside its specified bandwidth, as otherwise approximating incorrect branches as Rayleigh RVs is faulty. In other words, if the frequency difference between adjacent branches becomes very small, multiple simple correlators may operate inside their bandwidth and give a large correlation output. These branches can then not be characterized as Rayleigh RVs anymore and would also have to be considered as Rice distributed.

2) Furthermore, as mentioned earlier, the smaller the resolution of the bank of correlators, i.e., the frequency difference between two adjacent branches, the larger will be the error of approximating the branches as independent.

## 5.3. Swiveled Correlator

### Probability of false alarm $P_{\mathrm{fa}}$

For the swiveled correlator, the output of the correlation between the incoming noise and the preamble fragments is given by

$$w_n[\mu] = \sum_{k=(n-1)M}^{nM-1} n[\mu+k]\, c^*[k], \quad n \in \{1, N\}, \tag{5.19}$$

where $M = \frac{K}{N}$. Similarly to the analysis for the bank of correlators, we can establish that every $w_n[\mu]$ corresponds to the sum of $M$ circularly symmetric Gaussian RVs. Therefore, each $w_n[\mu]$ is also a circularly symmetric Gaussian RV with zero mean and per component variance of $M\sigma_n^2$. These are then fed as input to an FFT together with a padding of $Z$ zeros, for which Equation (4.22) gives the output of each bin as

$$v_i[\mu] = \sum_{n=1}^{N} w_n[\mu]\, e^{-j2\pi \frac{n}{N+Z} i}, \quad i \in \{1, N+Z\}. \tag{5.20}$$

As the complex exponential has unit magnitude, i.e., $|e^{j\varphi}| = 1$, $v_i[\mu]$ corresponds to the sum of $N$ circularly symmetric Gaussian RVs with zero mean and per component variance of $M\sigma_n^2$. Thus, $v_i[\mu]$ is a circularly symmetric Gaussian RV with zero mean and per component variance of $NM\sigma_n^2 = K\sigma_n^2$. The next step is to then take the absolute value of each bin. Hence, $|v_i[\mu]|$ is Rayleigh distributed with scale parameter $\sqrt{K\sigma_n^2}$. The PDF for each of the RVs is given by Equation (5.6). Similar to the bank of correlators, the probability of false alarm is given as the probability that the maximum of $(N+Z)$ Rayleigh distributed RVs exceeds the threshold $\lambda$:

$$P_{\mathrm{fa}}(\lambda) = \Pr\Big[\max_i(|v_i[\mu]|) > \lambda\Big] = 1 - \Pr\Big[|v_1[\mu]| \le \lambda, |v_2[\mu]| \le \lambda, ..., |v_{N+Z}[\mu]| \le \lambda\Big]. \tag{5.21}$$

We will rely on approximating this by assuming that the $(N+Z)$ Rayleigh RVs are independent. Equivalently to the reasoning for the bank of correlators, this can be formally expressed as

$$P_{\mathrm{fa}}(\lambda) \approx 1 - \prod_{i=1}^{N+Z} \Pr\Big[|v_i[\mu]| < \lambda\Big] = 1 - F_{\text{Rayleigh}}^{N+Z}(\lambda) \overset{(5.7)}{=} 1 - \left(1 - e^{-\frac{\lambda^2}{2K\sigma_n^2}}\right)^{N+Z}. \quad (5.22)$$

**Probability of correct detection $P_{\mathrm{d}}$**

According to Equations (4.14),(4.22) and (4.24), the output of each FFT bin for a fully contained preamble in the incoming signal is given by

$$v_i[0] = R_0^{(M)}(f_d) K_{Z,i}(f_d) + \sum_{n=1}^{N} \sum_{k=(n-1)M}^{nM-1} n[k]\, c^*[k]\, e^{-j2\pi \frac{n}{N+Z} i}, \quad i \in \{1, N+Z\}. \quad (5.23)$$

Hereby, we can see that the first term is deterministic for a given Doppler shift. We also know from the derivation of $P_{\mathrm{fa}}$ above, that the second term is a circularly symmetric Gaussian RV. Therefore, the output of each bin, $v_i[0]$, is a circularly symmetric Gaussian RV with mean $R_0^{(M)}(f_d)K_{Z,i}(f_d)$ and per component variance of $K\sigma_n^2$. The absolute value of such a RV is Rice distributed:

$$|v_i[0]| \sim \mathrm{Rice}(s', \sigma), \quad \text{where } s'(f_d, i) = |R_0^{(M)}(f_d) K_{Z,i}(f_d)| \quad \text{and } \sigma = \sqrt{K\sigma_n^2}. \quad (5.24)$$

In contrast to the bank of correlators, the Rice factor now depends on the Doppler shift $f_d$ and not on the difference between $f_d$ and the center frequency of the respective branch. Again, we will assume that a correct detection occurs if 1) the output of the correct bin exceeds the threshold and 2) the output of the correct bin is larger than the outputs of all other bins. Let us now assume that the $i$-th bin is the correct one and we will denote its output with $x$. Furthermore, we will denote the maximum output of the incorrect bins with $y$, hence we have

$$x = |v_i[0]|, \qquad y = \max_{j \neq i}(|v_j[0]|). \quad (5.25)$$

We can now formally describe the probability of correct detection as

$$P_{\mathrm{d}}(\lambda) = \Pr\Big[x > \lambda, x > y\Big] = \int_{\lambda}^{\infty} \int_{0}^{x} f_{X,Y}(x, y)\, dy\, dx. \quad (5.26)$$

As was the case for the bank of correlators, the joint PDF is unknown, and we will make some assumptions to obtain an approximation for $P_{\mathrm{d}}$. Equivalent to the assumptions made for the approximation of the bank of correlators, we assume that the incorrect bins are i.i.d. Rayleigh distributed. This yields a similar result as the one presented in Equation (5.17):

$$F_Y(y) = \Pr\Big[Y < y\Big] = \left(1 - e^{-\frac{y^2}{2K\sigma_n^2}}\right)^{N+Z-1}, \tag{5.27}$$

with the difference of having $(N+Z-1)$ Rayleigh RVs. We will also further approximate that the correct bin is independent from the incorrect bins, i.e., $x$ is independent of $y$. The approximation of the probability of correct detection for the swiveled correlator can then be found equivalently to the approximation for the bank of correlators given in Equation (5.18):

$$P_{\mathrm{d}}(\lambda) \approx \int_{\lambda}^{\infty} \left(1 - e^{-\frac{x^2}{2K\sigma_n^2}}\right)^{N+Z-1} \frac{x}{K\sigma_n^2} e^{-\frac{x^2+s'^2(f_d)}{2K\sigma_n^2}} I_0\left(\frac{xs'(f_d)}{K\sigma_n^2}\right) dx, \tag{5.28}$$

where $s'(f_d) = |R_0^{(M)}(f_d)K_Z(f_d)|$.
For the same reasons as given for the bank of correlators, we expect the considered approximation to be tight for a moderate amount of zero-padding.

## 5.4. Numerical Results

We will now validate the tightness of the presented analytic models for the three detection schemes by comparing them to simulations. Hereby, we expect that the model for the simple correlator is exact, since we do not make any approximations. For the bank of correlators and the swiveled correlator, we expect the approximations to be tight in configurations with a moderate amount of branches/bins.

Figure 5.1 shows the analytic and simulated ROC curve for the simple correlator, in a high SNR scenario. Hereby, a maximum Doppler shift of $f_{\max} = 0.05$ was assumed, as the performance of the simple correlator decreases for larger Doppler shifts. It can be seen that the two curves coincide, which suggests that the model is indeed exact. Furthermore, this also holds for low SNR scenarios, but a similar performance can then only be achieved by increasing the preamble length and reducing the maximum Doppler shift.

To verify the tightness of the approximations made for the bank of correlators and the swiveled correlator, we can analyze $P_{\mathrm{fa}}$ and $P_{\mathrm{d}}$ separately. Figure 5.2 compares the probability of false alarm $P_{\mathrm{fa}}$ of the analytic model and the simulation for the bank of correlators. It can be seen that the model is very tight for a moderate number of branches $N = K$. Increasing the number of branches to $N = 4K$, and therefore reducing

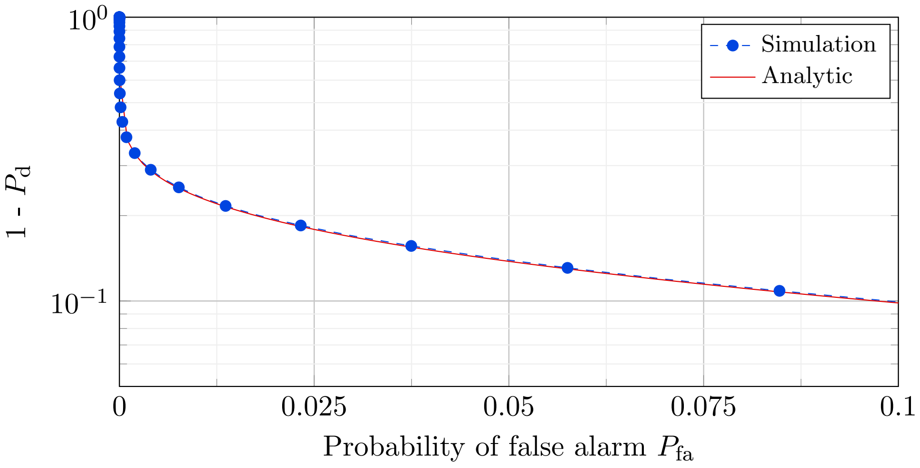

Figure 5.1.: ROC curve comparison of the analytic model and simulation for the simple correlator. $\frac{E_S}{N_0} = 0\,\mathrm{dB}, K = 15, f_{\max} = 0.05$.

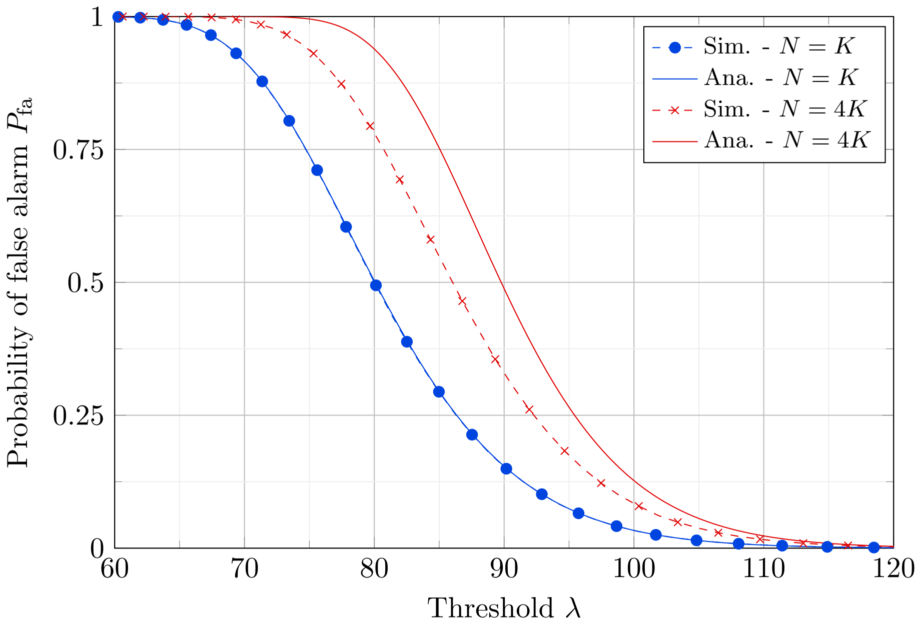

Figure 5.2.: $P_{\mathrm{fa}}$ comparison of th analytic model and simulation for the bank of correlators. $\frac{E_S}{N_0} = -9\,\mathrm{dB}, K = 150, f_{\max} = 0.5$.

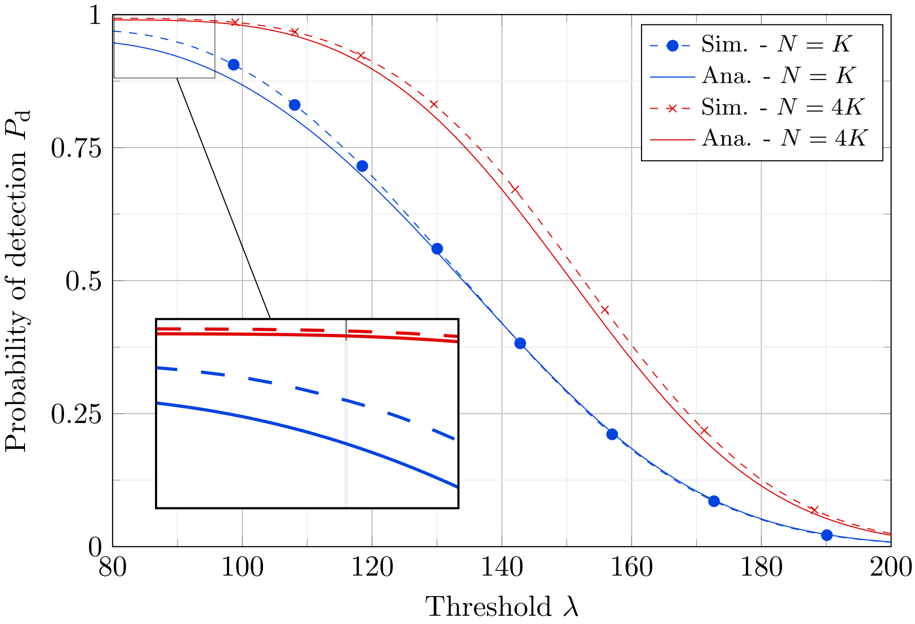

Figure 5.3.: $P_d$ comparison of th analytic model and simulation for the bank of correlators. $\frac{E_S}{N_0} = -9\,\text{dB}, K = 150, f_{\max} = 0.5$.

the frequency difference in adjacent branches, leads to a reduction in tightness. This is in line with the expectations, that the assumption of the branch outputs being independent becomes loose for a large number of branches. A very similar behavior was observed for the swiveled correlator.

Figure 5.3 plots the probability of detection $P_d$ of the bank of correlators across the threshold range. It can be seen that the analytic model is not exact, but still tight. Hereby, the analytic model considers the correct branch to be Rice distributed and the other branches to be i.i.d. Rayleigh. Therefore, we would also expect to see here, that the approximation is tighter for a moderate number of branches. Comparing the curves in the figure, it can be observed that this is true for low probability of detections of up to around 75 %, whereas for high probabilities the analytic model for a large number of branches becomes tighter. This is highlighted by the magnified part of the figure. This effect comes from also accepting Doppler estimates in adjacent branches of the correct branch. As mentioned earlier, since Doppler shifts in between two center frequencies cause an equally large output in the corresponding branches, we also consider Doppler estimates from one adjacent branch as a correct detection. This slightly increases the probability of detection with respect to the analytic model. The effect is reduced for a larger amount of branches, since the ratio of accepted frequency estimates to unaccepted frequency estimates becomes smaller. Also this effect could be observed for the swiveled

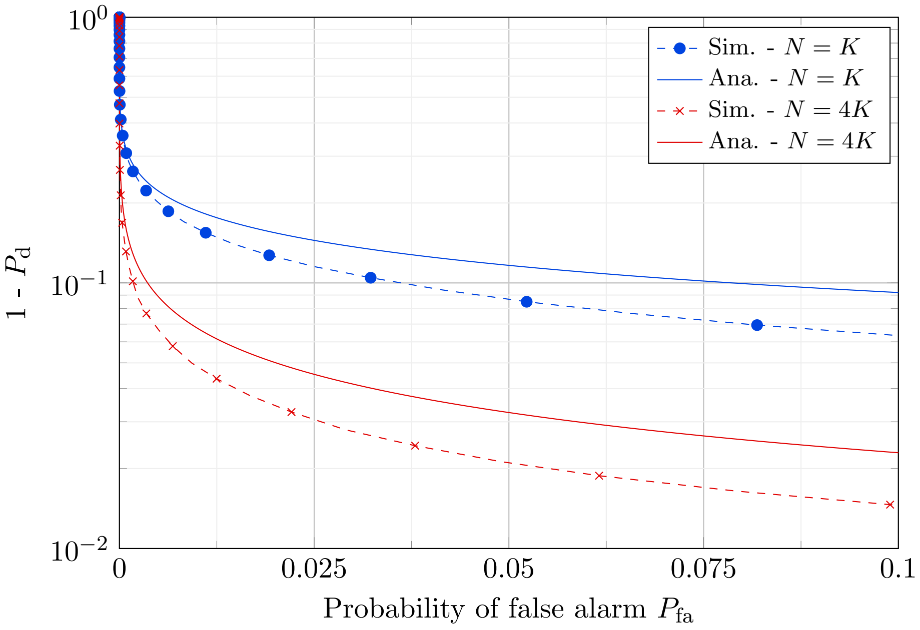

Figure 5.4.: ROC curve comparison of the analytic model and simulation for the bank of correlators. $\frac{E_S}{N_0} = -9\,\mathrm{dB}, K = 150, f_\mathrm{max} = 0.5$.

correlator, which was expected considering we made the same approximating assumptions for both schemes.

The combination of $P_\mathrm{fa}$ and $P_\mathrm{d}$ for the bank of correlators is shown as the ROC curve in Figure 5.4. Hereby, the analytic model is compared to a simulation in a low SNR scenario. It can be seen that both the models for a moderate amount of branches $N = K$ and the model for a larger number of branches $N = 4K$ are reasonably accurate. Hereby, the inaccuracy of the model with a moderate amount of branches comes from $P_\mathrm{d}$ and therefore from accepting frequency estimates of adjacent branches, while for the model with a large number of branches the inaccuracy comes from $P_\mathrm{fa}$ and therefore the assumption of independent branch outputs. The same behavior can be seen in Figure 5.5 for the swiveled correlator. It can also be noted that, in general, due to accepting multiple branches/bins, the analytic model underestimates the performance of the detector and a slightly better performance is observed in the simulations.

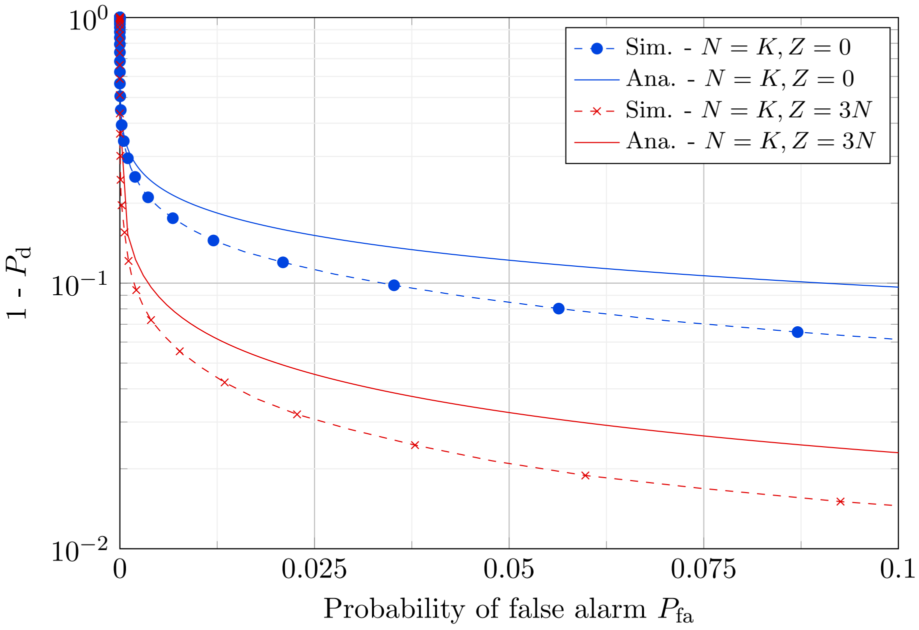

Figure 5.5.: ROC curve comparison of the analytic model and simulation for the swiveled correlator. $\frac{E_S}{N_0} = -9\,\mathrm{dB}, K = 150, f_\mathrm{max} = 0.5$.

# Part II.

# Discussion of Realistic Effects on Frame Synchronization

# 6. Passband Signal Processing with Frequency Offset

The second part of this thesis will contain a more realistic discussion of the problem of frame synchronization in the presence of a large Doppler shift. We will hereby deviate from the simplified environment that was assumed in the first part of the thesis, and in most related works in literature, and present a discussion of the impact of a frequency offset on the processing of a passband signal and the effect of the resulting ISI on the frame detection algorithms. We will start by shortly presenting the setting for the second part of thesis, focusing on differences to the first part and what effects they have.

## 6.1. Setting Description

A schematic representation of the processing chain in a practical communication system is given in Figure 6.1. Several processing steps irrelevant to the considered problem, such as coding, are omitted for simplicity. The incoming data bits $b[m] \in \{0, 1\}$ are firstly mapped to symbols $a[n]$ of the employed modulation scheme. The major difference to the setting in the first part of the thesis, is that in a practical transmission the resulting complex symbol stream has to undergo pulse shaping in order to create a waveform $x[k]$, which can actually be transmitted by an antenna. The pulse shaping filter employed in the course of the discussion is the square-root raised cosine (SRRC) pulse, which together

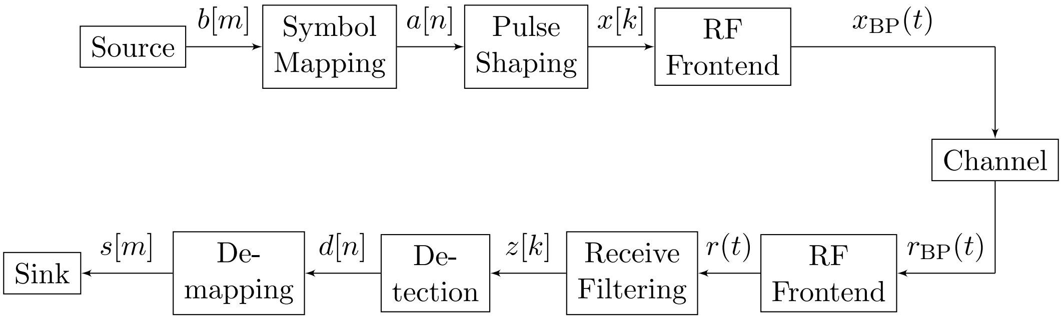

Figure 6.1.: Block diagram of the processing steps a communication system.

with another SRRC filter at the receiver creates a matched filter, satisfying the Nyquist criterion for ISI-free transmission. The frequency response of the SRRC filter is

$$P(f) = \begin{cases} \sqrt{T_S} & |f| \leq \frac{1-\beta}{2T_S} \\ \sqrt{\frac{T_S}{2}} \sqrt{1 + \cos(\frac{\pi T_S}{\beta} \left[|f| - \frac{1-\beta}{2T_S}\right])} & \frac{1-\beta}{2T_S} < |f| \leq \frac{1+\beta}{2T_S} \\ 0 & \text{otherwise,} \end{cases} \tag{6.1}$$

where $\beta$ is the roll-off factor. A plot of this frequency response is given in Figure 6.3.

After the pulse shaping, which can also be referred to as transmit filtering, the sample stream $x[k]$ is passed to the radio frequency (RF) frontend, where it is upconverted to the carrier frequency $f_c$ and transmitted by an antenna. The transmitted passband signal is denoted as $x_{\text{BP}}(t)$. We assume it is then affected by the channel in the same way we described it in the first part of the thesis, i.e., it experiences a possibly large and unknown Doppler shift and AWGN.

At the receiver, the incoming signal is then captured by an antenna in the RF frontend and downconverted from the carrier frequency. Since the actual carrier frequency of the received signal $r_{\text{BP}}(t)$ is affected by the Doppler shift, it is unknown at the receiver, which will cause a residual frequency offset to remain in the downconverted signal $r(t)$. At this point, the signal can be expressed generally as

$$r(t) = \sum_{m=0}^{X-1} a[m]\, p(t - mT_S)\, e^{j\left(2\pi f_d \frac{t}{T_S} + \phi\right)} + n_{\text{BP}}(t), \tag{6.2}$$

where $X$ is the length of the transmitted symbol stream, $p(t)$ is the impulse response of the pulse shaping filter, $f_d$ is the residual frequency offset due to Doppler and the noise $n_{\text{BP}}(t)$ has a constant PSD of $\frac{N_0}{2}$. The signal then has to be receive filtered, which is typically done using a matched filter to ensure ISI-free recovering of the signal. However, an uncorrected Doppler shift can affect the output of the receive filter.

## 6.2. Effect of Frequency Offset on Receive Filtering

In the process of converting an incoming waveform into a symbol stream, the downconverted incoming signal is first sampled. Hereby, the receiver may employ oversampling and pass the sample stream through a receive filter. The oversampled output of the receive filter can then be downsampled to symbol rate, where each sample corresponds to an incoming symbol. We hereby assume perfect timing synchronization is possible. The recovered symbol stream then mathematically corresponds to the downsampled output of the convolution of the sample stream with the impulse response of the filter:

$$\begin{aligned} z[k] &= (r * g)[k] \\ &= \left( \sum_{m=0}^{X-1} a[m] \int\limits_{-\infty}^{\infty} g(t)\, p\big((k-m)T_S - t\big)\, e^{-j2\pi f_d \frac{t}{T_S}}\, dt \right) e^{j(2\pi k f_d + \phi)} + n[k], \end{aligned} \tag{6.3}$$

where

$$n[k] = \int\limits_{-\infty}^{\infty} g(t)\, n_{\mathrm{BP}}(kT_S - t) dt$$

is the sampled and filtered noise, which now has a per component variance of $\sigma_n^2 = \frac{N_0}{2}$, $g(t)$ is the impulse response of the receive filter and $g(t) = p^*(-t)$ holds in the case of a matched filter.

The work in [PM96] presents the idea of splitting this representation of the filter output into several components:

$$z[k] = \left( a[k]\mathcal{I}_0(f_d) + \sum_{\substack{m=0 \\ m \neq k}}^{X-1} a[m]\mathcal{I}_{k-m}(f_d) \right) e^{j(2\pi k f_d + \phi)} + n[k], \tag{6.4}$$

where

$$\mathcal{I}_n(f_d) = \int\limits_{-\infty}^{\infty} g(t)\, p(nT_S - t)\, e^{-j2\pi f_d \frac{t}{T_S}}\, dt = \int\limits_{-\infty}^{\infty} G(f + \frac{f_d}{T_S})\, P(f)\, e^{j2\pi f n T_S} df. \tag{6.5}$$

Hereby, $G(f + \frac{f_d}{T_S} = G(f + F_d)$ is the frequency response of the receive filter, shifted in frequency by $F_d$. The set of functions $\mathcal{I}_n(f_d)$ describe the effect of the loss in symbol quality due to the Doppler shift. $\mathcal{I}_0(f_d)$ is an expression for the amplitude of the target symbol, which is attenuated in comparison to the Doppler free case, while $\mathcal{I}_n(f_d)$ for $n \neq 0$ gives the amplitude of the n-th adjacent symbol, hereby describing the impact of ISI. The detailed derivation of Equations (6.3), (6.4) and (6.5) is given in Appendix A.4. A visualization of the effect of a frequency offset on the absolute value of the impulse response of the matched filter pair is shown in Figure 6.2. It is indicated how the values of $\mathcal{I}_n$ help to interpret the loss in signal quality. It also shows the twofold effect of, firstly, the attenuation of the amplitude of the target symbol, and additionally, the increase in amplitude of adjacent symbols at the time of the target symbol, $t = 0$.

It is possible to find an analytical, closed form solution for $\mathcal{I}_n(f_d)$ by using the frequency response of the transmit filter $P(f)$ and the shifted frequency response of the receive filter

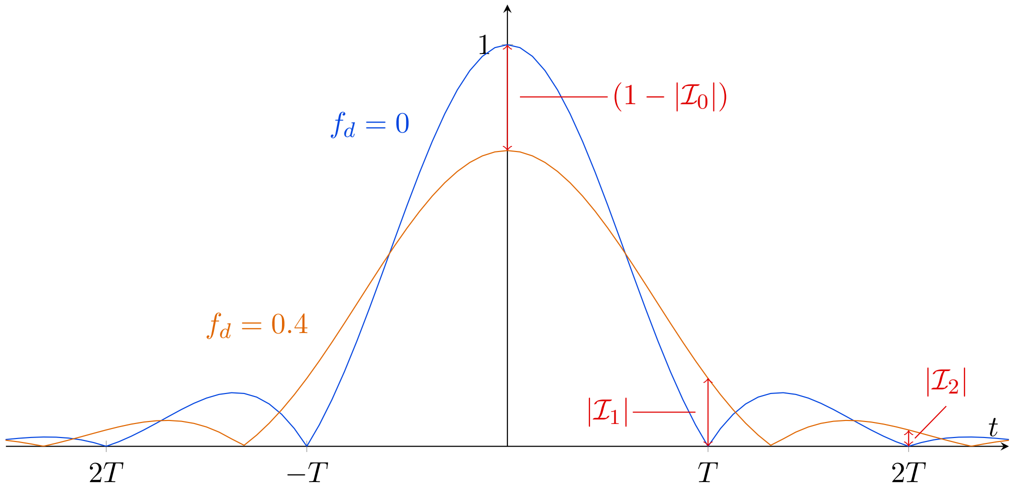

Figure 6.2.: Visualization of the ISI effects $\mathcal{I}_n$ on the absolute value of the impulse response of a combined SRRC matched filter pair.

$G(f+F_d)$. This is intuitive, since, due to the Doppler shift, the transmit and receive filter virtually operate at different frequencies. For the case of using a SRRC pulse shaping filter with frequency response given in (6.1), and a corresponding matched filter at the receiver with frequency response $G(f) = P(f)$, the shifted frequency response of the SRRC receive filter is

$$G(f+F_d) = \begin{cases} \sqrt{T_S} & |f+F_d| \leq \frac{1-\beta}{2T_S} \\ \sqrt{\frac{T_S}{2}}\sqrt{1+\cos(\frac{\pi T_S}{\beta}\left[|f+F_d| - \frac{1-\beta}{2T_S}\right])} & \frac{1-\beta}{2T_S} < |f+F_d| \leq \frac{1+\beta}{2T_S} \\ 0 & \text{otherwise.} \end{cases} \tag{6.6}$$

Both frequency responses are defined as piecewise functions, for which reason the product of the two is also a piecewise function. Therefore, the solution for $\mathcal{I}_n(f_d)$ can be computed by integrating the sub-functions over the corresponding intervals. The boundaries of the intervals correspond to the locations where one of the frequency responses changes its behavior. This is visualized in Figure 6.3. It has to be considered that these sections are only valid for $|f_d| < \beta$.

The piecewise integrals can be solved analytically to derive a closed form expression of the attenuation of the target symbol and the additional ISI components dependent on the Doppler shift. The detailed construction and solution of the integral is presented in Appendix A.5. For $n = 0$ the solution of the integral simplifies to

$$|\mathcal{I}_0(f_d)| = 1 - \beta - |f_d| + \frac{4\beta}{\pi}\sin\left(\left|\frac{\pi f_d}{2\beta}\right|\right) + (\beta - |f_d|)\cos(\frac{\pi f_d}{2\beta}). \tag{6.7}$$

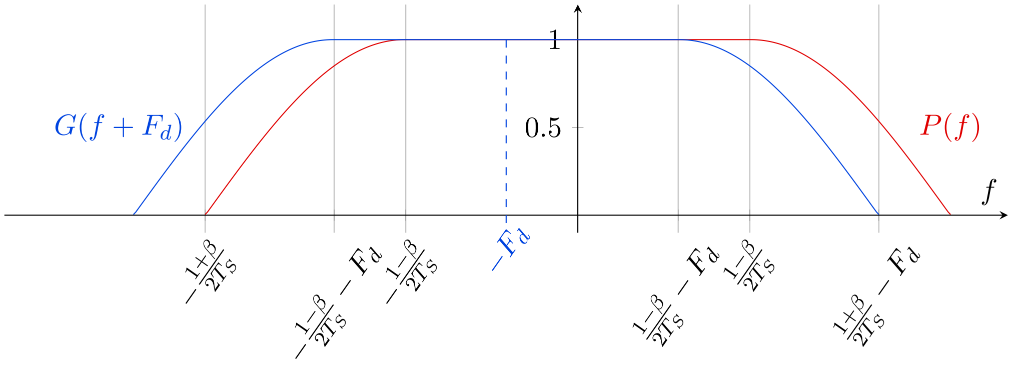

Figure 6.3.: Frequency analysis of a SRRC filter pair. $P(f)$ is the transmit filter and $G(f+F_d)$ is the receive filter, virtually operating at a shifted frequency.

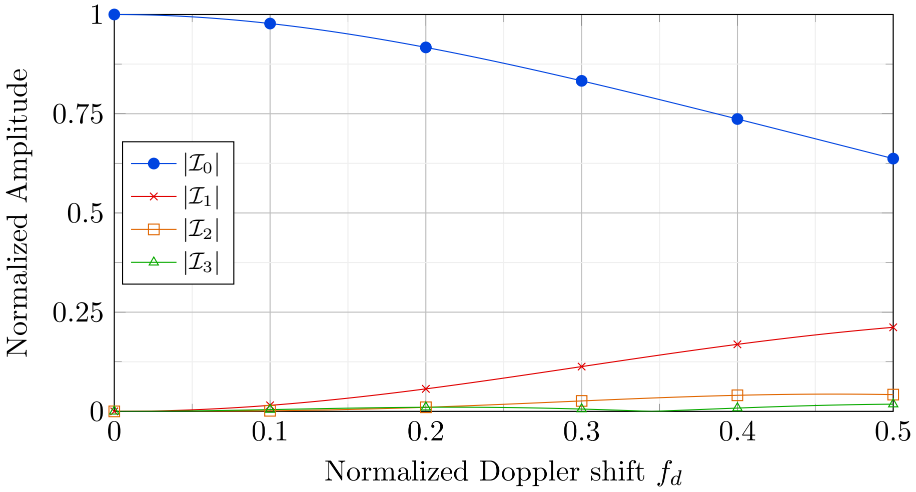

Figure 6.4.: $\mathcal{I}_0(f_d)$ up to $\mathcal{I}_3(f_d)$ as a function of the normalized Doppler shift, for a SRRC matched filter pair with roll-off $\beta = 0.5$.

The functions $\mathcal{I}_0(f_d)$ to $\mathcal{I}_3(f_d)$ are plotted in Figure 6.4 for a matched filter pair of SRRC pulses with a roll-off factor of $\beta = 0.5$. It can be seen that both the attenuation of the target symbol and the ISI from adjacent symbols are rather moderate for very small Doppler shifts, but become worse for Doppler shifts in the order of tenths of the bandwidth. Additionally, it can be noted that the amplitude of the ISI decreases significantly with growing distance between the observed symbol and the interfering symbol, suggesting that the immediate neighbors have the largest impact. In the remainder of the thesis, we will now refer to both the effects of attenuation and ISI simply as ISI.

# 7. Effect of ISI on Frame Synchronization

Let us know analyze the effect of ISI and the thereby distorted incoming symbols on the problem of frame synchronization. We will derive analytic models for the simple correlator, the bank of correlators and the swiveled correlator. Furthermore, we will also compare the detection schemes presented in Chapter 4 considering their performance and complexity.

## 7.1. Analytic Modeling

We will now conduct a similar analysis to the one presented in Chapter 5, only this time considering the effects of ISI. The discussion of the probability of false alarm $P_{\mathrm{fa}}$ follows the lines of what was presented in Chapter 5, since the noise is not affected by ISI. Therefore, the analytic models for $P_{\mathrm{fa}}$ can be found in Equations (5.8) for the simple correlator, (5.14) for the bank of correlators and (5.22) for the swiveled correlator. The discussion of the probability of correct detection $P_{\mathrm{d}}$ will be presented for each of the algorithms.

### 7.1.1. Simple Correlator

We now consider an ISI affected incoming symbol stream containing the preamble, which we get from Equation (6.4) by substituting the general symbols with the preamble:

$$z[k] = \left( c[k]\mathcal{I}_0(f_d) + \sum_{\substack{m=0 \\ m\neq k}}^{K-1} c[m]\mathcal{I}_{k-m}(f_d) \right) e^{j(2\pi k f_d + \phi)} + n[k]. \tag{7.1}$$

This signal is then correlated with the local preamble, which results in

$$w[0] = \mathcal{I}_0(f_d)\left(\sum_{k=0}^{K-1} e^{j(2\pi k f_d+\phi)} c[k]\, c^*[k]\right) \\ + \sum_{\substack{m=-\infty \\ m\neq k}}^{\infty} \mathcal{I}_{k-m}(f_d)\left(\sum_{k=0}^{K-1} e^{j(2\pi k f_d+\phi)} c[k-m]\, c^*[k]\right) + \sum_{k=0}^{K-1} n[k]\, c^*[k]. \quad (7.2)$$

This can be simplified to

$$w[0] = \mathcal{I}_0(f_d) R_0(f_d) + \sum_{\substack{m=-\infty \\ m\neq 0}}^{\infty} \mathcal{I}_m(f_d) R_m(f_d) + \sum_{k=0}^{K-1} n[k]\, c^*[k] \quad (7.3)$$

by expanding the definition of $R_0(f_d)$ given in Equation (4.3) to a more general expression:

$$R_n(f_d) = \sum_{k=0}^{K-1} e^{j(2\pi k f_d+\phi)} c[k-n]\, c^*[k], n \in \mathbb{Z}. \quad (7.4)$$

Hereby, $R_n$ gives a general description of the $n$-th sample of the correlation of the preamble with a frequency shifted version of itself. Note, that only $R_0$ is independent of the specific preamble employed. The different terms of the output of the correlation given in Equation (7.3) can be interpreted as follows: the first term corresponds to the correlation of the attenuated and Doppler shifted target symbols of the preamble with the local preamble. The second term describes the correlation of the ISI components of the neighboring symbols with the local preamble. The last term is the correlation of the local preamble with the noise. Moving on, we can find that the first two terms of $w[0]$, $\mathcal{I}_0(f_d)$ and $R_0(f_d)$, are deterministic for a given Doppler shift and the noise term is a circularly symmetric Gaussian RV. Therefore, $w[0]$ is a circularly symmetric Gaussian RV with mean

$$\mathrm{E}\left[w[0]\right] = \mathcal{I}_0(f_d) R_0(f_d) + \sum_{\substack{m=-\infty \\ m\neq 0}}^{\infty} \mathcal{I}_m(f_d) R_m(f_d)$$

and per component variance of $K\sigma_n^2$. Its absolute value is then Rice distributed:

$$|w[0]| \sim \mathrm{Rice}(\nu, \sqrt{K\sigma_n^2}), \quad \text{where } \nu(f_d) = |\mathcal{I}_0(f_d) R_0(f_d) + \sum_{\substack{m=-\infty \\ m\neq 0}}^{\infty} \mathcal{I}_m(f_d) R_m(f_d)|. \quad (7.5)$$

The probability of correct detection again corresponds to the probability that this Rice distributed RV exceeds the threshold $\lambda$:

$$P_{\mathrm{d}}(\lambda) = \Pr\Big[|w[0]| > \lambda\Big] = \int_{\lambda}^{\infty} \frac{x}{K\sigma_n^2}\, e^{-\frac{x^2+\nu^2(f_d)}{2K\sigma_n^2}}\, I_0\left(\frac{xs(f_d)}{K\sigma_n^2}\right) dx. \tag{7.6}$$

Since the Rice factor $\nu(f_d)$ depends on $R_n(f_d)$ and this is generally not independent of the specific preamble, the above expression also depends on the specific preamble. Furthermore, computing expressions for $\mathcal{I}_n(f_d)$ and $R_n(f_d)$ becomes cumbersome for long preambles, for which reason we approximate the Rice factor as

$$\tilde{\nu}(f_d) = |\mathcal{I}_0(f_d) R_0(f_d)|. \tag{7.7}$$

We expect this approximation to be tight. We can therefore give a general approximation of the probability of correct detection that is independent of the preamble:

$$P_{\mathrm{d}}(\lambda) \approx \int_{\lambda}^{\infty} \frac{x}{K\sigma_n^2}\, e^{-\frac{x^2+\tilde{\nu}^2(f_d)}{2K\sigma_n^2}}\, I_0\left(\frac{x\tilde{\nu}(f_d)}{K\sigma_n^2}\right) dx. \tag{7.8}$$

### 7.1.2. Bank of Correlators

For the bank of correlators we will again consider $N$ parallel branches. However, the bank of correlators has the distinct advantage that it is easily possible to shift the frequency for each branch before the receive filter. The corresponding block diagram is depicted in Figure 7.1. Although this increases the complexity, as also $N$ receive filters have to operated, it significantly reduces the effects of ISI and therefore increases the performance for large Doppler shifts, which will be emphasized using simulations in the next section. Instead of the receive filter dealing with Doppler shifts between $[-f_{\max}, f_{\max}]$, the receive filter of the correct branch only has a maximum frequency offset of $\hat{f}_r = \frac{f_{\max}}{N-1}$. This significantly reduces ISI in the correct branch.

We know from our previous discussion that the output $|w_i[0]|$ of each branch (combination of receive filter and simple correlator) is Rice distributed with parameters $\nu(f_d-(i-1)\Delta f)$ (or $\tilde{\nu}$ for an approximation of the Rice factor) and $\sqrt{K\sigma_n^2}$. For the correct branch, the Rice factor will be $\nu(f_r)$ (or $\tilde{\nu}(f_r)$), while we will again approximate the other branches with i.i.d. Rayleigh RVs with scale parameter $\sqrt{K\sigma_n^2}$. The rest of the discussion is equivalent to the one presented for $P_{\mathrm{d}}$ of the bank of correlators in Chapter 5, which

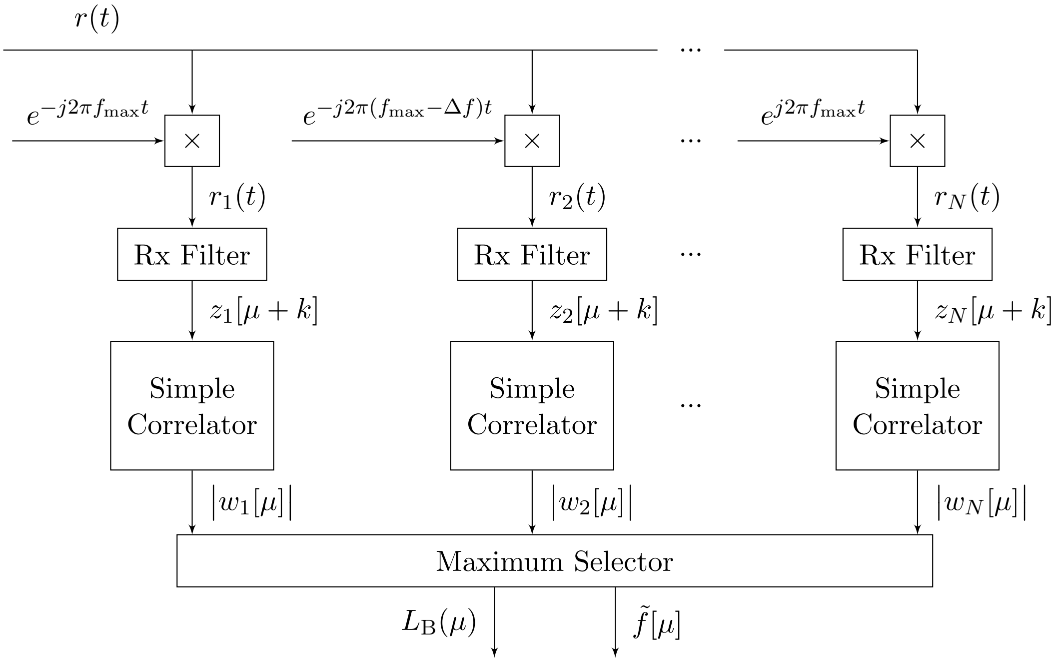

Figure 7.1.: Block diagram of the bank of correlators including the receive filters in every branch.

ultimately leads to an approximation of the probability of detection as

$$P_{\mathrm{d}}(\lambda) = \int_{\lambda}^{\infty} \left(1 - e^{-\frac{x^2}{2K\sigma_n^2}}\right)^{N-1} \frac{x}{K\sigma_n^2} e^{-\frac{x^2+\tilde{\nu}^2(f_r)}{2K\sigma_n^2}} I_0\left(\frac{x\tilde{\nu}(f_r)}{K\sigma_n^2}\right) dx. \tag{7.9}$$

### 7.1.3. Swiveled Correlator

For the swiveled correlator the discussion will become significantly more complex, due to the partial correlation with preamble fragments. For the sake of simplicity, we will approximate the incoming symbol stream by neglecting the actual ISI effects and only considering the attenuation of the target symbol, i.e.,

$$z[k] = c[k]\mathcal{I}_0(f_d)e^{j(2\pi k f_d+\phi)} + n[k]. \tag{7.10}$$

This is equivalent to the approximation made for the Rice factor in Section 7.1.1. The outputs of the partial correlations are then given by

$$w_n[0] = \mathcal{I}_0(f_d)R_0^{(M)}(f_d)e^{j2\pi f_d(n-1)M} + \sum_{k=(n-1)M}^{nM-1} n[k]\, c^*[k], \quad n \in \{1, N\} \tag{7.11}$$

while the output for each bin of the subsequent FFT will be

$$v_i[0] = \mathcal{I}_0(f_d)R_0^{(M)}(f_d)K_{Z,i}(f_d) + \sum_{n=1}^{N} \sum_{k=(n-1)M}^{nM-1} n[k]\, c^*[k]e^{-j2\pi\frac{n}{N+Z}i}, \quad i \in \{1, N+Z\}. \tag{7.12}$$

Again, the first term is deterministic for a given Doppler shift and the second term is a circularly symmetric Gaussian RV. Therefore, the absolute value of the outputs are Rice distributed:

$$|v_i[0]| \sim \mathrm{Rice}(\tilde{\nu}', \sqrt{K\sigma_n^2}), \quad \text{where } \tilde{\nu}'(f_d) = |\mathcal{I}_0(f_d)R_0^{(M)}(f_d)K_{Z,i}(f_d)|. \tag{7.13}$$

From here, the discussion is equivalent to the one presented for the swiveled correlator without ISI in Chapter 5. The approximation of $P_\mathrm{d}$ therefore corresponds to

$$P_\mathrm{d}(\lambda) \approx \int_{\lambda}^{\infty} \left(1 - e^{-\frac{x^2}{2K\sigma_n^2}}\right)^{N+Z-1} \frac{x}{K\sigma_n^2} e^{-\frac{x^2+\tilde{\nu}'^2(f_d)}{2K\sigma_n^2}} I_0\left(\frac{x\tilde{\nu}'(f_d)}{K\sigma_n^2}\right) dx, \tag{7.14}$$

where $\tilde{\nu}'(f_d) = |\mathcal{I}_0(f_d)R_0^{(M)}(f_d)K_Z(f_d)|$.

### 7.1.4. Numerical Results

We now want to verify the presented models and approximation by simulation, similar to the discussion of the numerical results in Chapter 5. For all simulations in this section, the pulse shaping and receive filters were implemented as finite impulse response (FIR) filters with a span of 11 symbols and a roll-off factor of $\beta = 0.5$.

Figure 7.2 compares the analytic model of the simple correlator to the simulation in a high SNR scenario. In contrast to the discussion in baseband, the analytical model is now an approximation, where only the effect of $\mathcal{I}_0$ was considered and $\mathcal{I}_n, n \neq 0$, were assumed to be 0. Therefore, the model is not exact, but the simulation shown in the figure suggests that it is very tight. Furthermore, for the simple correlator the correlation loss $R_0$ dominates the loss due to ISI $I_0$, as it is far more severe already for relatively small Doppler shifts.

The same argument can be made for the bank of correlators. Hereby, the correct branch experiences only a minor amount of ISI and the loss of $R_0$ dominates. The incorrect branches experience more ISI, but anyway operate outside their bandwidth, meaning that $R_0$ is so small we approximate the output as a Rayleigh RV. Additionally, since the ISI experienced by the correct branch is very small, the absolute performance of the bank of correlators also does not change from the baseband discussion in Section 5.4.

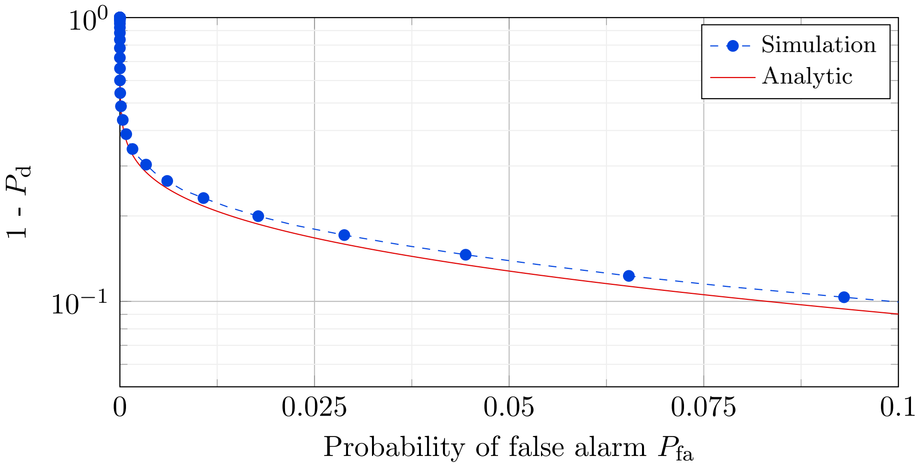

Figure 7.2.: ROC curve comparison of the analytic model and simulation for the simple correlator considering ISI. $\frac{E_S}{N_0} = 0\,\mathrm{dB}, K = 15, f_\mathrm{max} = 0.05$.

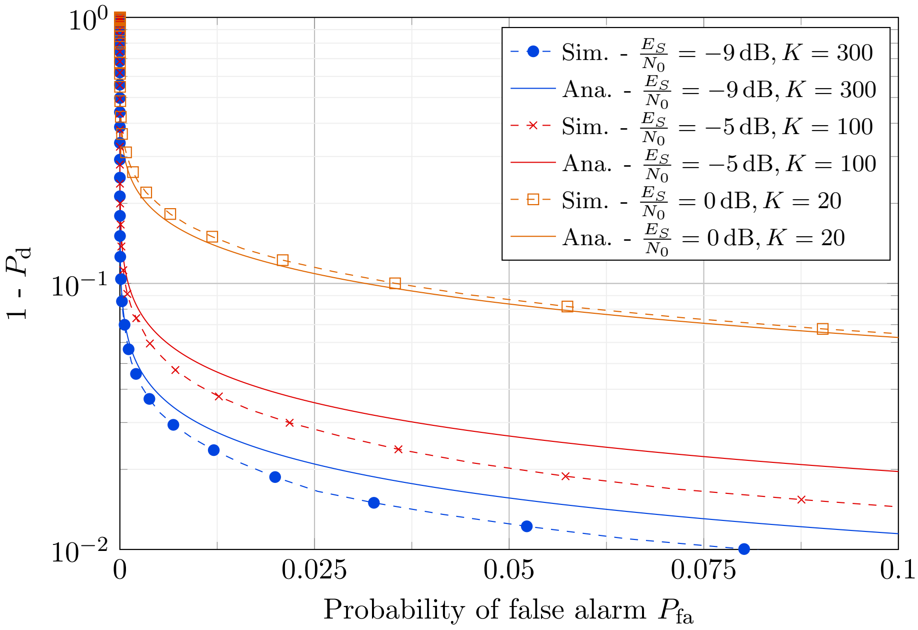

Figure 7.3.: ROC curve comparison of the analytic model and simulation for the swiveled correlator considering ISI. The swiveled correlator was configured with $N = K$ branches, therefore, $M = 1$, and a padding of $Z = N$ zeros. The maximum Doppler shift was $f_\mathrm{max} = 0.5$.

Finally, for the swiveled correlator the ISI losses actually dominate over $R_0$ for subsequence lengths of $M = 1$. Therefore, by approximating the Rice factor with the effects of $\mathcal{I}_0$ and $R_0$ and disregarding the interference from adjacent symbols, the modeled output of the correct bin will be (slightly) larger. However, during the discussion in the baseband setting in Section 5.4 we established that the analytic model gives a conservative approximation, meaning that the actual performance was observed to be slightly better than the model estimated. Therefore, the effects discussed in the baseband setting and the approximation of the Rice factor counteract eachother and the resulting model considering ISI is even slightly more tight than in the baseband setting. The comparison of the analytic model and the simulation is shown in Figure 7.3 for different scenarios. The experimental results show the tightness of the analytic model in several SNR scenarios.

## 7.2. Comparison and Discussion

To compare the different detection schemes in an ISI affected setting, we performed simulations in a similar manner as described in Section 4.6. The employed pulse shaping and receive filters were implemented as FIR filters with a span of 11 symbols and a roll-off factor of $\beta = 0.22$.

### Performance across Doppler range

Similar to the comparison in the first part of thesis, we want to examine the detection performance across the range of frequency offsets. This is plotted in Figure 7.4. The simple correlator $L_\mathrm{C}$ behaves very similarly to the baseband discussion without ISI. This can be attributed to the dominance of the correlation loss $R_0(f_d)$ over the loss due to ISI. The effect of ISI becomes apparent when considering the swiveled correlator $L_\mathrm{S}$, the double correlator $L_\mathrm{A}$ or the Choi-Lee detector $L_\mathrm{CL}$, which show a significant degradation in detection performance for larger frequency offsets. Also, the advantage of the bank of correlators $L_\mathrm{B}$ in the ISI affected setting becomes apparent: due to the frequency adjustment before the receive filter operation, the effect of ISI is limited on the frequency range of one branch. In other words, the receive filter of the correct branch operates with a small residual frequency offset, whereas the receive filter in the other detection schemes has to deal with the full range of Doppler shifts. Apart from the loss in between the branches due to the small bandwidth of the correlation, the detection performance of the bank of correlators is constant over the full Doppler range. The severity of the loss in between branches, and likely the scalloping loss of the swiveled correlator, can again be reduced by using more resources.

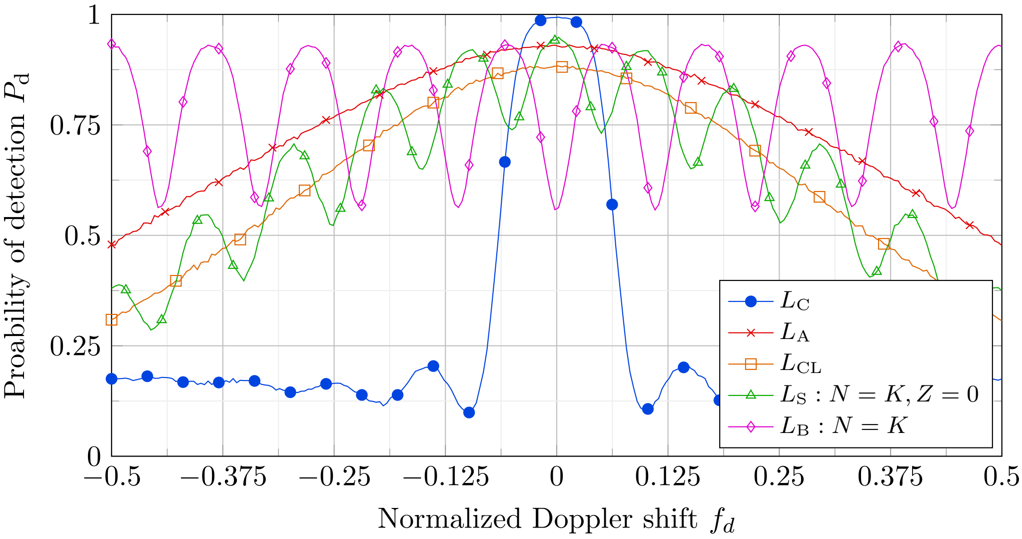

Figure 7.4.: Comparison of the detection performance across the normalized frequency offset in a high SNR scenario. $\frac{E_S}{N_0} = 2\,\mathrm{dB}$, $K = 10$, $P_\mathrm{fa} = 10^{-1} \pm 10^{-3}$.

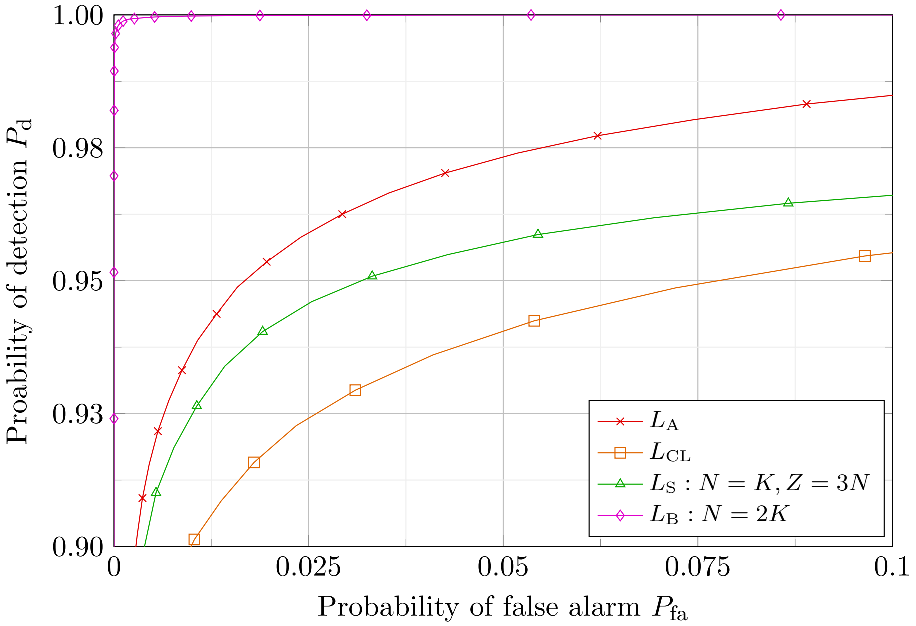

Figure 7.5.: Simulated ROC at high SNR considering ISI. $\frac{E_S}{N_0} = 0\,\mathrm{dB}$, $K = 30$, $f_\mathrm{max} = 0.5$.

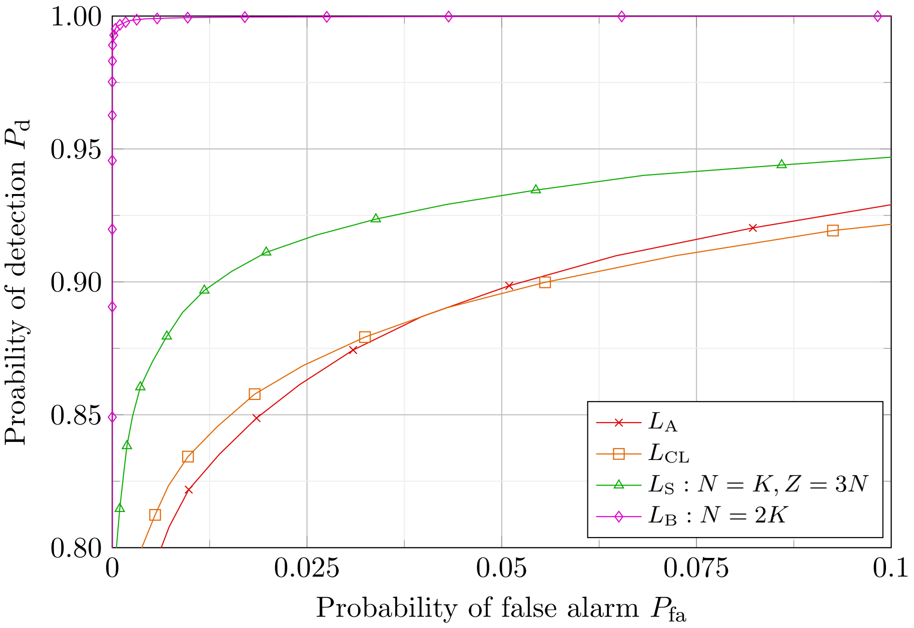

Figure 7.6.: Simulated ROC at low SNR considering ISI. $\frac{E_S}{N_0} = -9\,\mathrm{dB}$, $K = 250$, $f_\mathrm{max} = 0.5$.

### High SNR

Figure 7.5 shows the simulation results for a high SNR scenario of a passband transmission. It can be seen that the bank of correlators with a number of branches of $2K$ significantly outperforms the other detection schemes. This can be attributed to the use of a bank of receive filters, which greatly reduces the effects of ISI in the correct branch, so that again the correlation loss $R_0(f_d)$ dominates. The cost of reducing ISI is a much higher complexity. Regarding the other detection schemes, the double correlator performs better than the swiveled correlator and the Choi-Lee detector in this high SNR scenario.

### Low SNR

Again considering a low SNR scenario, which is more typical for a satellite link, Figure 7.6 shows that the double correlator $L_\mathrm{A}$ strongly loses in performance. This is in line with the findings of the baseband discussion in Part I, which showed that the $L_\mathrm{A}$ detector did not perform well in low SNR scenarios.

### Considering partially contained preambles

Similarly to the discussion in Part I, we can examine the effect of partially contained preambles. The simulation setup is hereby chosen equivalently, embedding a preamble

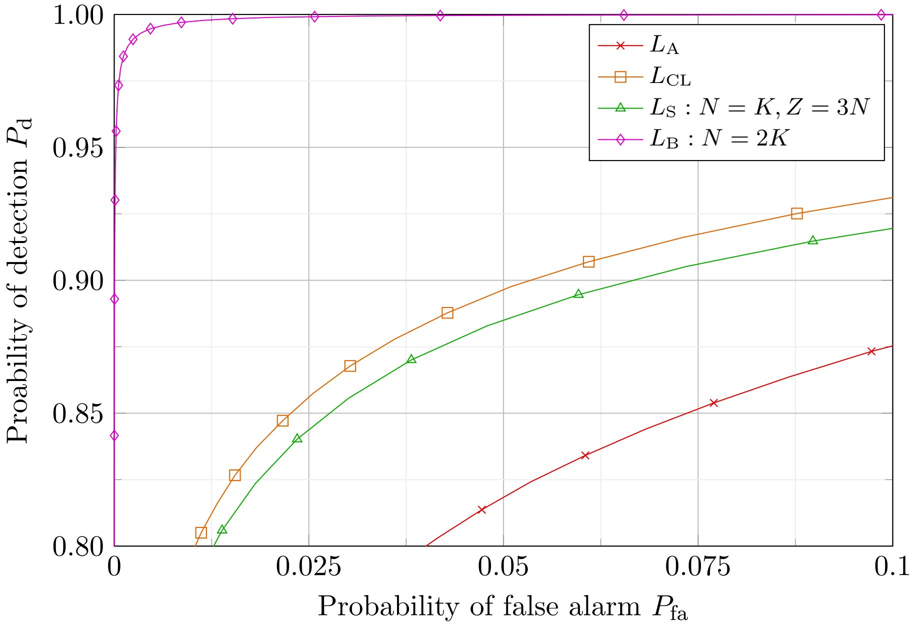

Figure 7.7.: Simulated ROC at high SNR considering ISI and partially contained preambles. $\frac{E_S}{N_0} = 0\,\mathrm{dB}$, $K = 30$, $f_\mathrm{max} = 0.5$.

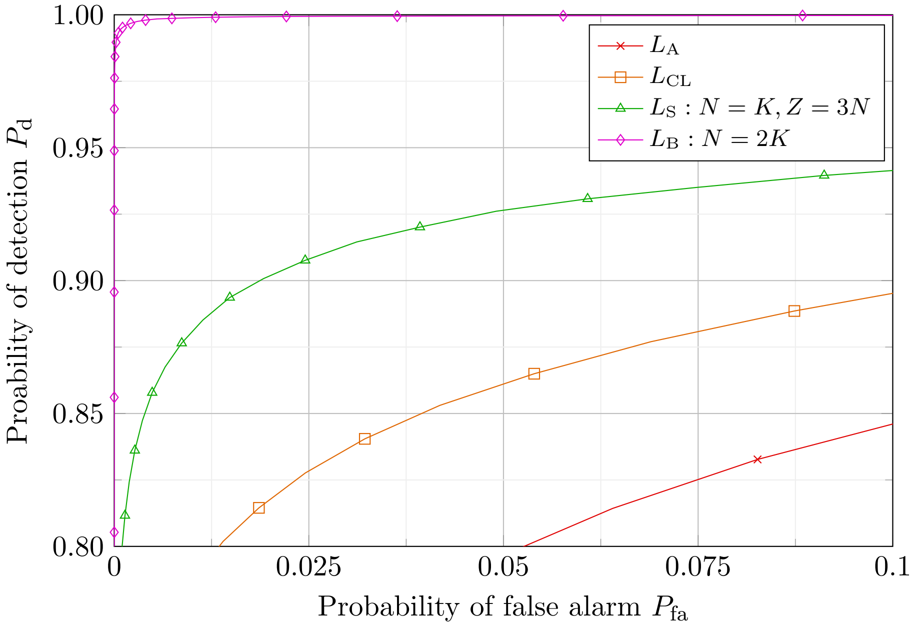

Figure 7.8.: Simulated ROC at low SNR considering ISI and partially contained preambles. $\frac{E_S}{N_0} = -9\,\mathrm{dB}$, $K = 250$, $f_\mathrm{max} = 0.5$.

every $3K$ symbols, as previously shown in Figure 4.12. This symbol stream will then be pulse shaped, impaired by Doppler shift and noise, received filtered, and then supplied to the detectors. The Simulated a high SNR environment shows that also in the ISI affected setting, the Choi-Lee detector suffers the smallest performance loss, actually performing similarly well as without partially contained preambles. This can again be attributed to the energy correction term.

Accordingly, the Simulated a low SNR environment, shown in Figure 7.8, reveals that the benefit of this energy correction term becomes smaller in low SNR environments, where the signal energy is anyway dominated by the noise. When comparing Figures 7.6 and 7.8, it becomes apparent that the performance of the swiveled correlator barely changes when considering partially contained preambles. This further validates the assumption of disregarding partially contained preambles in a low SNR satellite setting for the analytic modeling of the detection schemes presented in Section 7.1.

### Different tradeoffs between performance and complexity

The presented simulations confirmed that the bank of correlators corresponds to a detector design that achieves very good performance, but has a high complexity. On the other hand, the swiveled correlator performs significantly worse, but has a very low complexity. A possible method to find a tradeoff in between these two, i.e., a design with good performance and moderate complexity, could be to use a hybrid approach, which may be called bank of swiveled correlators. Hereby, the idea is to operate several receive filters and swiveled correlators at different center frequencies to reduce the effects of ISI in the correct branch and identify the correct branch with a maximum selector. This corresponds to exchanging the simple correlators in the branches of the bank of correlators with swiveled correlators. However, a much smaller amount of branches can be used, which will be elaborated in the following.

Essentially, the bank of correlators was presented in Chapter 4 as a method to mitigate the correlation loss $R_0(f_d)$. As discussed, the swiveled correlator already solves this problem in a different way. However, the performance of the swiveled correlator is significantly decreased by the effects of ISI, $\mathcal{I}_n(f_d)$, due to imperfect receive filtering. The losses due to ISI can be reduced by employing a bank of receive filters, as is done for the bank of correlators. However, the losses due to ISI, $\mathcal{I}_n(f_d)$, are much less severe than the correlation loss $R_0(f_d)$, especially for small frequency shifts. Additionally, they are independent of the preamble length and therefore do not become more severe for longer preambles used in low SNR scenarios, as is the case for the correlation loss. Therefore, already a small amount of receive filters, e.g. four or eight, could substantially reduce the losses due to ISI. For the standard bank of correlators, a configuration with such a small amount of branches would be impractical, since the residual frequency offset in each branch would still cause unacceptably large correlation losses. However, since the swiveled correlator is not subject to such large correlation losses, the reduced ISI by employing a a bank of swiveled correlators with a few branches with receive filters at different frequency shifts can significantly improve the performance, while still achieving a much lower complexity than the bank of correlators.

A comparison of different configurations corresponding to different tradeoffs between performance and complexity is left for further study. A more detailed analysis of this detection scheme is expected to be a relatively straightforward extension of the discussion in Section 7.1.

## 7.3. Complexity

An important aspect of the previous sections is that the bank of correlators can successfully reduce the effect of ISI by performing the receive filtering after the frequency shift in each branch. However, this significantly increases the computational complexity of the algorithm. Since the resources of a satellite are limited, the problem of frame detection is subject to constraints in the computational effort. It is generally desirable to find a tradeoff with good performance and low complexity. It is therefore important to also compare the regarded schemes considering their computational complexity. Hereby, it is necessary to consider different preamble lengths, since the preamble length has to be adjusted to the SNR in order to reach high detection probabilities.

A well-suited and commonly used figure of merit for such a comparison is the Big O notation of the number of operations with respect to the preamble length. Table 7.1 gives the computational complexity of each detector. The simple correlator, naturally, has the lowest complexity, corresponding to the length of the correlation, i.e., $\mathcal{O}(K)$. The bank of correlators employs $N$ parallel branches with simple correlators (and also receive filters) and is therefore $N$ times as complex. The number of branches $N$ is $\mathcal{O}(K)$, since the number of branches has to be increased for longer preambles in order to obtain a high detection probability. Therefore, the bank of correlators requires $\mathcal{O}(K^2)$ operations. Similarly, the double correlator and the Choi-Lee detector compute the sum of all possible double correlations, which also corresponds to $\mathcal{O}(K^2)$ operations. The swiveled correlator uses $N$ branches, in each of which a correlation of length $M$ is performed. This results in a complexity of $\mathcal{O}(K)$ operations for the correlation, which is succeeded by an FFT. The complexity of an FFT is $\mathcal{O}(K \log K)$ and therefore dominates over the correlation.

The Big O notation provides us a first insight into the complexity of the different schemes

| Detector | Operations |
|---|---|
| Simple correlator $L_{\mathrm{C}}$ | $\mathcal{O}(K)$ |
| Bank of correlators $L_{\mathrm{B}}$ | $\mathcal{O}(K^2)$ |
| Swiveled correlator $L_{\mathrm{S}}$ | $\mathcal{O}(K \log K)$ |
| Double correlator $L_{\mathrm{A}}$ | $\mathcal{O}(K^2)$ |
| Choi-Lee detector $L_{\mathrm{CL}}$ | $\mathcal{O}(K^2)$ |

Table 7.1.: Computational complexity of the considered detection schemes

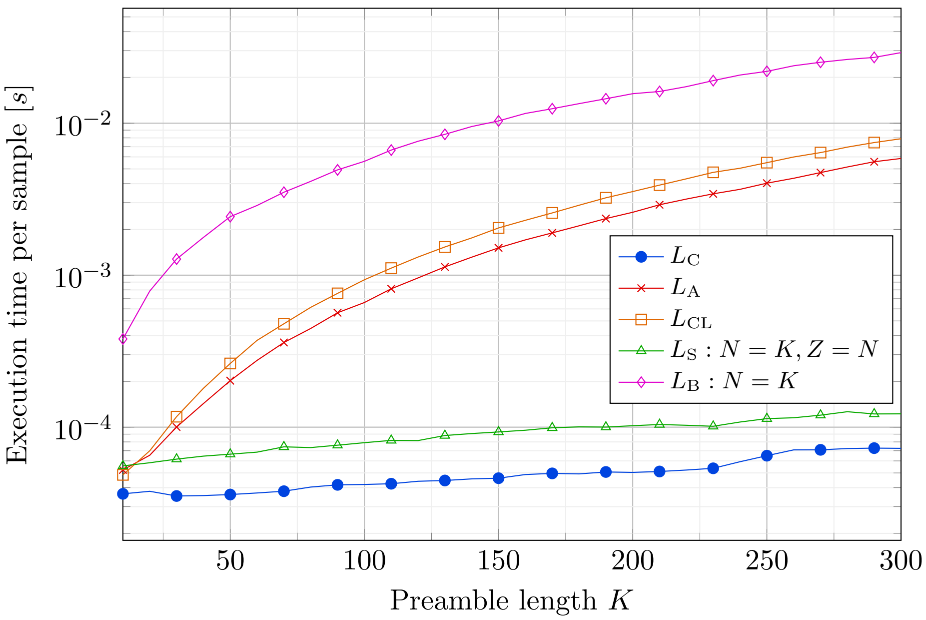

Figure 7.9.: Comparison of the execution time of software implementations of the detection schemes.

in the asymptotic regime where $K$ tends to infinity, i.e., for very large preamble lengths. However, in practical systems we can expect the preamble length to be at most in the order of a few thousands, more commonly a few hundred symbols. In this regime, we cannot expect asymptotic considerations to hold tightly, thus it is important to look at other, non-asymptotic measures for the complexity. For this reason, we simulated the expected execution time of the MATLAB software implementations of the detectors. Figure 7.9 plots the execution time per output sample across the preamble length. This shows, that for small preambles, the bank of correlators is already much more computationally expensive. This is mainly due to the bank of receive filters. It can also be seen that the Choi-Lee detector is slightly more complex than the double correlator, which comes from the additional computation of the data correction term. It becomes clear that the swiveled correlator has by far the lowest complexity of the detection schemes that can deal with large Doppler shifts.

It may be added that in a practical implementation other criteria, such as the possibility to parallelize the processing, might play an important role. A more detailed complexity analysis is left for further study.

## 7.4. Summary

When comparing the detection schemes in an ISI affected setting, it becomes clear that due the employment of a bank of receive filters, the bank of correlators outperforms the other schemes by far. The cost for the better performance is a significantly increased complexity. The comparison also reveals that the swiveled correlator is the least complex detector and, additionally, shows a better performance than the double correlator and the Choi-Lee detector in satellite characteristic low SNR scenarios. Furthermore, the benefit of simultaneously performing frame synchronization and obtaining an estimate for the Doppler shift (as can be done for the bank of correlators and the swiveled correlator) becomes clear: if a preamble is correctly detected, the Doppler estimate can be used to adjust the center frequency of the receive filter for the subsequent processing of the rest of the packet. This significantly reduces the effect of ISI and increases the probability of correctly decoding the data.

# 8. Simulations of Realistic Satellite Link

For the previous analysis and simulations we assumed a very controlled scenario, with constant SNR and a uniform Doppler shift between $f_d \in [-f_{\text{max}}, f_{\text{max}}]$, where usually $f_{\text{max}} = 0.5$. Such a large Doppler shift can be considered extreme and not particularly realistic in practical satellite transmission scenarios. Additionally, although we considered low SNR scenarios in the previous simulations and we tried to indicate towards the characteristics of a satellite transmission, we will now present some simulations for a realistic LEO satellite link. The parameters characterizing the link are listed in Table 8.1. To simulate the transmission from any terminal in the coverage of the satellite, we uniformly sample a point in the coverage area. We then compute the Doppler shift (see Appendix A.6 for details) and the SNR for this point. It is notable that the distribution of the Doppler shift is not anymore uniform. We then average over a significant amount of such transmissions to obtain the average performance of the detection schemes in the satellites coverage area. The results of the simulation are shown in Figure 8.1.

It can be seen that the bank of correlators with $2K$ parallel branches performs significantly better than all other detectors. This is again attributed to the mitigation of ISI losses by employing a bank of receive filters. A configuration using less resources, i.e., $K$ parallel branches, shows a significant decrease in performance due to stronger correlation losses. Hereby, the correlation loss $R_0$ still dominates the additional loss due to ISI. In this configuration it performs similarly well as the swiveled correlator with a subsequence length of $M = 1$ and a zero-padding ratio of $\frac{Z}{N} = 3$. While the Choi-Lee correlator

| Description | Symbol | Value |
|---|---|---|
| Carrier frequency | $f_c$ | 2 GHz |
| Symbol rate | $\frac{1}{T_S}$ | 250 kHz |
| Satellite altitude | $h$ | 575 km |
| Maximum slant range | $d_{\text{max}}$ | 1300 km |
| SNR at CoC | $\frac{E_s}{N_0}\big\rvert_{\text{CoC}}$ | $-6$ dB |
| SNR at EoC | $\frac{E_s}{N_0}\big\rvert_{\text{EoC}}$ | $-13$ dB |

Table 8.1.: Parameters of the considered LEO satellite link.

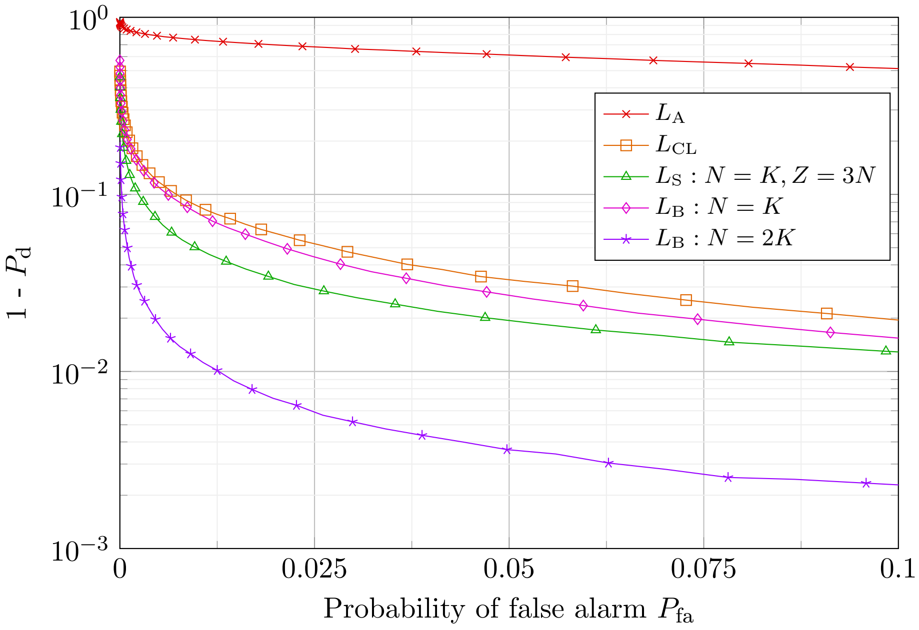

Figure 8.1.: Simulated ROC for a realistic LEO satellite link. The employed preamble length was $K = 350$ symbols. Other parameters are given in Table 8.1.

performs slightly worse than those two, the double correlator has a substantially lower detection probability. This emphasizes that the double correlator does not perform well in low SNR scenarios. However, it is interesting that the Choi-Lee detector performs significantly better than the the double correlator, considering it also uses the double correlation and subtracts a data correction term. Although this is intended to reduce the influence of random data surrounding the preamble, it seems like it also improves the performance in low SNR scenarios. The root cause of this could not be established in the narrow time frame of this thesis and therefore remains subject to further investigation.

# 9. Conclusion

The research presented in this thesis explored the problem of frame synchronization in a satellite setting, in which a large, possibly unknown Doppler shift cannot be precompensated and therefore decreases the performance of traditional synchronization algorithms. Additionally, the process of receive filtering is affected by the Doppler induced frequency offset and ISI occurs. Due to the highly dynamic nature of a random access setting, sequential frame detection techniques based on hypothesis testing were considered.

In the first part of the thesis, a simplified discussion of the problem considering a baseband representation of the incoming signal was performed. Hereby, in Chapter 3, the derivation of an optimal LRT in the considered setting was presented.

Chapter 4 introduced several relevant detection algorithms, including an approximation of the optimal LRT. It was also shown that a frequency offset in the incoming preamble leads to a substantial decrease of the correlation output, making detection less reliable in the presence of noise. The presented detectors aim to resolve this problem and were compared in different scenarios. It was shown that the approximation of the optimal LRT, which corresponds to a double correlation, significantly loses performance in low SNR environments. The swiveled correlator and the bank of correlators show close to optimal performance in all considered scenarios, where the swiveled correlator achieves a much lower complexity.

In Chapter 6 we conducted an in-depth study of the effects of ISI due to receive filtering when a frequency offset is present. While we identified in Chapter 7 that using a bank of matched filters for the bank of correlators solves the problem in a performant way, the complexity of the algorithm becomes unacceptably high. The swiveled correlator shows a good tradeoff between performance and complexity.

In Chapters 5 and 7, analytic models were derived for the simple correlator, the bank of correlators and the swiveled correlator for both cases with and without ISI. The developed approximations can quickly estimate and predict the performance of the algorithms. This can help to explore the parameter space and determine an approximate configuration of preamble length, number of branches and amount of zero-padding fitting to the requirements of the application. Making these design choices with an analytical model rather than elaborate simulations can speed up the development process.

Finally, the simulations of a realistic satellite link presented in Chapter 8 confirm that the findings established in a simplified scenario also apply to the characteristics of a realistic link.

### Future Work

The discussion of the frame synchronization problem in the given satellite setting is still somewhat incomplete and needs to be extended with further research. Given the findings we made in the thesis, we may indicate interesting issues to consider in the future. Additionally, some smaller peculiarities were identified in the course of the thesis, but remain unsolved.

In Chapter 4, it was identified that the approximation of the optimal LRT is not tight in low SNR scenarios. The origin of this loss may be the approximation of the Bessel function with a second order polynomial, which may only be tight in certain scenarios. However, this was not sufficiently investigated and deserves further attention. It could also be interesting to explore other low-complexity approximations for the Bessel function.

It became clear in Chapter 8, that the double correlator performs substantially worse than the Choi-Lee detector, although the two differ only in a data correction term. It is unclear why the data correction term, which is intended to reduce the influence of random data surrounding the preamble, increases the performance and deserves further research.

The comparison of the discussed detection schemes considering ISI conducted in Chapter 7 showed that the bank of correlators significantly outperforms the other methods. This can be attributed to the employment of a bank of matched filters, which reduces ISI effectively, but significantly increases the complexity. It could be worthwhile to investigate low-complexity alternatives to this problem. A first starting point could be the modification of the receive filter, e.g. increasing the bandwidth to capture more of the incoming signal. A very brief introduction to this is given in Appendix B.

The problem of frame synchronization in the considered random access satellite setting was discussed in a simplified manor by analyzing an isolated preamble. Therefore, further research has to be conducted considering also the data part of the packet. In the absence of multi-user interference, the data part could be used in addition to the preamble to detect the packet. In the simplest form, an additional energy detector would confirm the presence of the packet using the data part. However, it is unclear how effective this is in low SNR scenarios, given that the noise energy is dominating, and if other methods can be found to favorably use the data part of the packet for detection.

Furthermore, a very important aspect of frame synchronization in a random access setting is the influence of interference from other users. It is generally desirable to operate a system at a high load, so all resources are optimally used. However, this leads to the collision and interference of packets. The effect of incoming preambles interfering with random data or other preambles with possibly different frequency shifts is therefore an important subject of further research.

# A. Derivations and Proofs

## A.1. Derivation of the Optimal LRT

Starting from Equation (3.10),

$$L(\mu) = \frac{\frac{1}{8\pi^2 f_{\max}} \int\limits_{-\pi}^{\pi} \int\limits_{-2\pi f_{\max}}^{2\pi f_{\max}} \frac{1}{(\pi\sigma_n^2)^K} \cdot e^{-\frac{1}{\sigma_n^2} \sum\limits_{k=0}^{K-1} \left| r[\mu+k] - c[k] e^{j(\theta k+\phi)} \right|^2} \, d\phi \, d\theta}{\frac{1}{(\pi\sigma_n^2)^K} \cdot e^{-\frac{1}{\sigma_n^2} \sum\limits_{k=0}^{K-1} |r[\mu+k]|^2}} \underset{\mathcal{H}_0}{\overset{\mathcal{H}_1}{\gtrless}} \lambda, \tag{A.1}$$

we can use the independence of $r[\mu + k]$ on $\theta$ and $\phi$ to move the denominator inside the integral and reduce the constant factor to give

$$L(\mu) = \frac{1}{8\pi^2 f_{\max}} \int\limits_{-\pi}^{\pi} \int\limits_{-2\pi f_{\max}}^{2\pi f_{\max}} e^{-\frac{1}{\sigma_n^2} \sum\limits_{k=0}^{K-1} \left| r[\mu+k] - c[k] e^{j(\theta k+\phi)} \right|^2} \cdot e^{\frac{1}{\sigma_n^2} \sum\limits_{k=0}^{K-1} |r[\mu+k]|^2} \, d\phi \, d\theta. \tag{A.2}$$

In the next step the integrals can be combined:

$$L(\mu) = \frac{1}{8\pi^2 f_{\max}} \int\limits_{-\pi}^{\pi} \int\limits_{-2\pi f_{\max}}^{2\pi f_{\max}} e^{\frac{1}{\sigma_n^2} \left( \sum\limits_{k=0}^{K-1} |r[\mu+k]|^2 - \sum\limits_{k=0}^{K-1} \left| r[\mu+k] - c[k] e^{j(\theta k+\phi)} \right|^2 \right)} \, d\phi \, d\theta. \tag{A.3}$$

We can define $z_1 = r[\mu + k]$ and $z_2 = c[k]e^{j(\theta k+\phi)}$ and use the following rules of complex numbers:

$$\begin{aligned} |z_1 - z_2|^2 &= (z_1 - z_2)(z1 - z2)^* = (z_1 - z_2)(z_1^* - z_2^*) \\ &= z_1 z_1^* - z_1 z_2^* - z_2 z_1^* + z_2 z_2^* \\ &= |z_1|^2 + |z_2|^2 - 2\mathrm{Re}\left(z_1 z_2^*\right) \end{aligned}$$

to give

$$\begin{aligned}\left|r[\mu+k]-c[k]e^{j(\theta k+\phi)}\right|^2 &= |r[\mu+k]|^2+\left|c[k]e^{j(\theta k+\phi)}\right|^2-2\mathrm{Re}\left(r[\mu+k]\left(c[k]e^{j(\theta k+\phi)}\right)^*\right)\\ &= |r[\mu+k]|^2+\left|c[k]e^{j(\theta k+\phi)}\right|^2-2\mathrm{Re}\left(r[\mu+k]c^*[k]e^{-j(\theta k+\phi)}\right).\end{aligned} \tag{A.4}$$

Equation (A.4) can then be input into equation (A.3) to result in

$$L(\mu)=\frac{1}{8\pi^2 f_{\max}}\int\limits_{-\pi}^{\pi}\int\limits_{-2\pi f_{\max}}^{2\pi f_{\max}} e^{\frac{1}{\sigma_n^2}\left(\sum\limits_{k=0}^{K-1}|r[\mu+k]|^2-\sum\limits_{k=0}^{K-1}\left(|r[\mu+k]|^2+\left|c[k]e^{j(\theta k+\phi)}\right|^2-2\mathrm{Re}\left(r[\mu+k]c^*[k]e^{-j(\theta k+\phi)}\right)\right)\right)}\, d\phi\; d\theta \tag{A.5}$$

$$=\frac{1}{8\pi^2 f_{\max}}\int\limits_{-\pi}^{\pi}\int\limits_{-2\pi f_{\max}}^{2\pi f_{\max}} e^{\frac{1}{\sigma_n^2}\left(\sum\limits_{k=0}^{K-1}2\mathrm{Re}\left(r[\mu+k]c^*[k]e^{-j(\theta k+\phi)}\right)-\sum\limits_{k=0}^{K-1}\left|c[k]e^{j(\theta k+\phi)}\right|^2\right)}\, d\phi\; d\theta \tag{A.6}$$

$$=\frac{1}{8\pi^2 f_{\max}}\int\limits_{-\pi}^{\pi}\int\limits_{-2\pi f_{\max}}^{2\pi f_{\max}} e^{\frac{2}{\sigma_n^2}\sum\limits_{k=0}^{K-1}\mathrm{Re}\left(r[\mu+k]c^*[k]e^{-j(\theta k+\phi)}\right)}\, e^{-\frac{1}{\sigma_n^2}\sum\limits_{k=0}^{K-1}|c[k]|^2}\, d\phi\; d\theta \tag{A.7}$$

$$=\frac{1}{8\pi^2 f_{\max}}C(\mathbf{c},\sigma_n^2)\int\limits_{-\pi}^{\pi}\int\limits_{-2\pi f_{\max}}^{2\pi f_{\max}} e^{\frac{2}{\sigma_n^2}\sum\limits_{k=0}^{K-1}\mathrm{Re}\left(r[\mu+k]c^*[k]e^{-j(\theta k+\phi)}\right)}\, d\phi\; d\theta, \tag{A.8}$$

where $C(\mathbf{c},\sigma_n^2)=e^{-\frac{1}{\sigma_n^2}\sum_{k=0}^{K-1}|c[k]|^2}$. From equation (A.5) to (A.6) we use the associativity of the sum and simplify the resulting expression. Furthermore, in (A.6) it can be exploited that a complex exponential has unit magnitude:

$$\left|c[k]\cdot e^{j(\theta k+\phi)}\right|^2=|c[k]|^2\cdot\left|e^{j(\theta k+\phi)}\right|^2=|c[k]|^2. \tag{A.9}$$

Therefore, the result of (A.9) can be split into a separate exponential as given in (A.7). As this term is independent of $\theta$ and $\phi$ it can be moved outside the integral and was named $C(\mathbf{c},\sigma_n^2)$. Equation (A.8) corresponds to Equation (6) in [WRKH18], where some typing errors where corrected.

We can further simplify the expression by using the following rule of sums of complex numbers:

$$\mathrm{Re}\,(z) + \mathrm{Re}\,(w) = \mathrm{Re}\,(z+w)\,. \tag{A.10}$$

The argument of the exponential in A.8 can then be transformed:

$$\frac{2}{\sigma_n^2}\sum_{k=0}^{K-1} \mathrm{Re}\left(r[\mu+k]c^*[k]e^{-j(\theta k+\phi)}\right) = \mathrm{Re}\left(\frac{2}{\sigma_n^2}\sum_{k=0}^{K-1} r[\mu+k]c^*[k]e^{-j(\theta k+\phi)}\right). \tag{A.11}$$

This can also be expressed in terms of the magnitude and phase of the complex number:

$$\mathrm{Re}\left(\frac{2}{\sigma_n^2}\sum_{k=0}^{K-1} r[\mu+k]c^*[k]e^{-j(\theta k+\phi)}\right) = \rho\cdot\cos(\phi'), \tag{A.12}$$

$$\text{with } \rho = \frac{2}{\sigma_n^2}\left|\sum_{k=0}^{K-1} r[\mu+k]c^*[k]e^{-j(\theta k+\phi)}\right|$$

$$\text{and } \phi' = \arg\left(\frac{2}{\sigma_n^2}\sum_{k=0}^{K-1} r[\mu+k]c^*[k]e^{-j(\theta k+\phi)}\right) = \eta + \phi,$$

where $\eta$ contains the phase of the transmitted symbols, which for M-PSK follows a discrete uniform distribution depending on the modulation order, the phase due to the frequency shift $\theta k$ and the phase of the random noise. Since we integrate over $\phi$, it can take an arbitrary value and therefore also absorb $\eta$, so that integrating over $\phi$ and $\phi'$ is equivalent. We can therefore integrate over $\phi'$ instead of $\phi$, which results in

$$L(\mu) = \frac{1}{8\pi^2 f_{\max}} C(\mathbf{c},\sigma_n^2)\int_{-\pi}^{\pi}\int_{-2\pi f_{\max}}^{2\pi f_{\max}} e^{\rho\cdot\cos(\phi')}\,d\phi'\,d\theta \underset{\mathcal{H}_0}{\overset{\mathcal{H}_1}{\gtrless}} \lambda. \tag{A.13}$$

We can now solve the integral over $\phi'$ using the zeroth order modified Bessel function, given in [Wat95] as

$$I_0(\rho) = \frac{1}{\pi}\int_0^{\pi} e^{\rho\cdot\cos(\phi')}\,d\phi' = \frac{1}{2\pi}\int_{-\pi}^{\pi} e^{\rho\cdot\cos(\phi')}\,d\phi'. \tag{A.14}$$

We can also remove the random phase offset $\phi$ from $\rho$, since it does not depend on the index of the sum and has unit magnitude:

$$\begin{aligned} r &= \frac{2}{\sigma_n^2}\left|\sum_{k=0}^{K-1} r[\mu+k]c^*[k]e^{-j(\theta k+\phi)}\right| = \frac{2}{\sigma_n^2}\left|\sum_{k=0}^{K-1} r[\mu+k]c^*[k]e^{-j\theta k}e^{-j\phi}\right| \\ &= \frac{2}{\sigma_n^2}\left|e^{-j\phi}\sum_{k=0}^{K-1} r[\mu+k]c^*[k]e^{-j\theta k}\right| = \frac{2}{\sigma_n^2}\cdot 1\cdot\left|\sum_{k=0}^{K-1} r[\mu+k]c^*[k]e^{-j\theta k}\right| \\ &= \frac{2}{\sigma_n^2}\left|\sum_{k=0}^{K-1} r[\mu+k]c^*[k]e^{-j\theta k}\right|. \end{aligned} \tag{A.15}$$

Finally moving $C(\mathbf{c}, \sigma_n^2)$ to the threshold and applying the modified Bessel function leads us to the ultimate representation of the LRT

$$L(\mu) = \frac{1}{4\pi f_{\max}} \int_{-2\pi f_{\max}}^{2\pi f_{\max}} I_0\left(\frac{2}{\sigma_n^2}\left|\sum_{k=0}^{K-1} r[\mu+k]c^*[k]e^{-j\theta k}\right|\right) d\theta \underset{\mathcal{H}_0}{\overset{\mathcal{H}_1}{\gtrless}} \lambda. \tag{A.16}$$

## A.2. Approximation of the Optimal LRT

The optimal LRT and therefore the starting point for finding an approximation is given by

$$L(\mu) = \frac{1}{4\pi f_{\max}} \int_{-2\pi f_{\max}}^{2\pi f_{\max}} I_0\left(\frac{2}{\sigma_n^2}\left|\sum_{k=0}^{K-1} r[\mu+k]c^*[k]e^{-j\theta k}\right|\right) d\theta. \tag{A.17}$$

The first step is to expand the Bessel function using its series representation:

$$I_0(x) = \sum_{i=0}^{\infty} \frac{\left(\frac{1}{4}x^2\right)^i}{(i!)^2}, \tag{A.18}$$

which yields

$$\begin{aligned} L(\mu) = \frac{1}{4\pi f_{\max}} \int_{-2\pi f_{\max}}^{2\pi f_{\max}} 1 + \sum_{i=1}^{\infty}\left(\frac{1}{\sigma_n^2}\right)^{2i} \frac{1}{(i!)^2} \sum_{k_1=0}^{K-1}\sum_{l_1=0}^{K-1} \dots \sum_{k_i=0}^{K-1}\sum_{l_i=0}^{K-1} r[\mu+k_1]r^*[\mu+l_1] \\ \cdot c^*[k_1]c[l_1]r[\mu+k_i]r^*[\mu+l_i]c^*[k_i]c[l_i]\cdot e^{j\theta[(k_1-l_1)+\dots+(k_i-l_i)]}\, d\theta. \end{aligned} \tag{A.19}$$

After applying the sum rule of integrals we can once again exploit the independence of $\mathbf{r}$ and $\mathbf{c}$ on $\theta$ and move the terms outside the integral:

$$\begin{aligned} L(\mu) = \frac{1}{4\pi f_{\max}} \Bigg( \int\limits_{-2\pi f_{\max}}^{2\pi f_{\max}} 1 \, d\theta + \sum_{i=1}^{\infty} \left(\frac{1}{\sigma_n^2}\right)^{2i} \frac{1}{(i!)^2} \sum_{k_1=0}^{K-1} \sum_{l_1=0}^{K-1} \dots \sum_{k_i=0}^{K-1} \sum_{l_i=0}^{K-1} r[\mu+k_1] r^*[\mu+l_1] \\ \cdot c^*[k_1] c[l_1] r[\mu+k_i] r^*[\mu+l_i] c^*[k_i] c[l_i] \int\limits_{-2\pi f_{\max}}^{2\pi f_{\max}} e^{j\theta \sum\limits_{q=1}^{i} (k_q - l_q)} \, d\theta \Bigg). \end{aligned} \tag{A.20}$$

The next step is to solve the integral over the complex exponential. We can hereby use the general rules of solving integrals and the Euler's formula to find that

$$\begin{aligned} \frac{1}{4\pi f_{\max}} \int\limits_{-2\pi f_{\max}}^{2\pi f_{\max}} e^{j\theta k} d\theta &= \frac{1}{4\pi f_{\max}} \left[ \frac{1}{jk} e^{j\theta k} \right]_{-2\pi f_{\max}}^{2\pi f_{\max}} = \frac{1}{4\pi f_{\max}} \left( e^{j 2\pi f_{\max} k} - e^{-j 2\pi f_{\max} k} \right) \\ &= \frac{1}{j4\pi f_{\max}} \big( \cos(2\pi f_{\max} k) + j \, \sin(2\pi f_{\max} k) \\ &\qquad - \cos(2\pi f_{\max} k) + j \, \sin(2\pi f_{\max} k) \big) \\ &= \frac{\sin(2\pi f_{\max} k)}{2\pi f_{\max} k} = \operatorname{sinc}(2 f_{\max} k). \end{aligned} \tag{A.21}$$

Applying Equation (A.21) to (A.20) yields

$$\begin{aligned} L(\mu) = 1 + \sum_{i=1}^{\infty} \left(\frac{1}{\sigma_n^2}\right)^{2i} \frac{1}{(i!)^2} \sum_{k_1=0}^{K-1} \sum_{l_1=0}^{K-1} \dots \sum_{k_i=0}^{K-1} \sum_{l_i=0}^{K-1} r[\mu+k_1] r^*[\mu+l_1] c^*[k_1] c[l_1] \dots \\ r[\mu+k_i] r^*[\mu+l_i] c^*[k_i] c[l_i] \cdot \operatorname{sinc}\left( 2 f_{\max} \sum_{q=1}^{i} (k_q - l_q) \right). \end{aligned} \tag{A.22}$$

Since we compare the likelihood function to a threshold $\lambda$, the constant 1 can be absorbed by this threshold. We then follow the same approach as [WRKH18] and only consider the term $i = 2$. Thus, we have

$$\begin{aligned} L_{\mathrm{A}}(\mu) = \sum_{k_1=0}^{K-1} \sum_{l_1=0}^{K-1} \sum_{k_2=0}^{K-1} \sum_{l_2=0}^{K-1} r[\mu+k_1] \; r^*[\mu+l_1] \; c^*[k_1] \; c[l_1] \\ \cdot \, r[\mu+k_2] \; r^*[\mu+l_2] \; c^*[k_2] \; c[l_2] \; \operatorname{sinc}\left(2 f_{\max} \left(k_1 - l_1 + k_2 - l_2\right)\right). \end{aligned} \tag{A.23}$$

## A.3. Simplification of $R_0$

Regarding the simplification of $R_0(f_d)$, we can use $c[k]c^*[k] = |c[k]|^2 = E_S = 1$ to transform Equation (4.3) to

$$R_0(f_d) = \sum_{k=0}^{K-1} e^{j(2\pi k f_d + \phi)}. \tag{A.24}$$

We can use Euler's formula to transform the sum of complex exponential into sums of sines and cosines:

$$R_0(f_d) = \sum_{k=0}^{K-1} \cos(2\pi k f_d + \phi) + i \sum_{k=0}^{K-1} \sin(2\pi k f_d + \phi). \tag{A.25}$$

To evaluate the sums we can use the following series for sum of sines/cosines:

$$\sum_{k=0}^{K-1} \sin(\phi' + k\alpha) = \frac{\sin(\frac{K}{2}\alpha)\sin(\frac{K-1}{2}\alpha + \phi')}{\sin(\frac{\alpha}{2})}, \tag{A.26}$$

$$\sum_{k=0}^{K-1} \cos(\phi' + k\alpha) = \frac{\sin(\frac{K}{2}\alpha)\cos(\frac{K-1}{2}\alpha + \phi')}{\sin(\frac{\alpha}{2})}. \tag{A.27}$$

Applying these series to Equation (A.25) yields

$$R_0(f_d) = \frac{\sin(K\pi f_d)\cos((K-1)\pi f_d + \phi)}{\sin(\pi f_d)} + i\frac{\sin(K\pi f_d)\sin((K-1)\pi f_d + \phi)}{\sin(\pi f_d)}. \tag{A.28}$$

We can then factor out common terms:

$$R_0(f_d) = \frac{\sin(K\pi f_d)}{\sin(\pi f_d)}\left(\cos((K-1)\pi f_d + \phi) + i\,\sin((K-1)\pi f_d + \phi)\right). \tag{A.29}$$

Finally, applying the Euler's formula to Equation (A.29) gives the simplified expression for $R_0(f_d)$:

$$R_0(f_d) = \frac{\sin(K\pi f_d)}{\sin(\pi f_d)} e^{j((K-1)\pi f_d + \phi)}. \tag{A.30}$$

## A.4. Derivation of $\mathcal{I}_n$

The incoming downconverted passband signal is described in Equation (6.2) as

$$r(t) = \sum_{m=0}^{X-1} a[m]\, p(t - mT_S)\, e^{j\left(2\pi f_d \frac{t}{T_S} + \phi\right)} + n_{\mathrm{BP}}(t). \tag{A.31}$$

This signal is then filtered using a receive filter with impulse response $g(t)$. This mathematically corresponds to the convolution, for which we can use its distributivity and its associativity with scalar multiplication:

$$z'(t) = (r * g) = \sum_{m=0}^{X-1} a[m] \left( e^{j\left(2\pi f_d \frac{t}{T_S} + \phi\right)} p(t - mT_S) * g(t) \right) + n_{\mathrm{BP}}(t) * g(t). \tag{A.32}$$

Expanding the convolution yields

$$\begin{aligned} z'(t) &= \sum_{m=0}^{X-1} a[m] \int_{-\infty}^{\infty} g(\tau) p(t - \tau - mT_S) e^{j\left(2\pi \frac{f_d}{T_S}(t-\tau) + \phi\right)} \, d\tau + \int_{-\infty}^{\infty} g(\tau) n_{\mathrm{BP}}(t - \tau) \\ &= e^{j\left(2\pi f_d \frac{t}{T_S} + \phi\right)} \sum_{m=0}^{X-1} a[m] \int_{-\infty}^{\infty} g(\tau) p(t - \tau - mT_S) e^{-j2\pi \frac{f_d}{T_S}\tau} \, d\tau + \int_{-\infty}^{\infty} g(\tau) n_{\mathrm{BP}}(t - \tau) \, d\tau. \end{aligned} \tag{A.33}$$

The filtered signal is then downsampled to symbol rate, so each sample corresponds to a symbol of the transmitted signal. Hereby, perfect timing synchronization is assumed. Thus, by sampling at $t = kT_S$ we obtain

$$z[k] = e^{j(2\pi k f_d + \phi)} \sum_{m=0}^{X-1} a[m] \int_{-\infty}^{\infty} g(\tau) p((k - m)T_S - \tau) e^{-j2\pi \frac{f_d}{T_S}\tau} \, d\tau + \int_{-\infty}^{\infty} g(\tau) n_{\mathrm{BP}}(kT_S - \tau) \, d\tau. \tag{A.34}$$

Now, exchanging $\tau$ with $t$ yields

$$z[k] = e^{j(2\pi k f_d + \phi)} \sum_{m=0}^{X-1} a[m] \int_{-\infty}^{\infty} g(t) p((k - m)T_S - t) e^{-j2\pi \frac{f_d}{T_S} t} \, dt + \int_{-\infty}^{\infty} g(t) n_{\mathrm{BP}}(kT_S - t) \, dt. \tag{A.35}$$

This proves Equation 6.3.

As mentioned in Chapter 6, we now follow the approach of [PM96] by rephrasing this equation to

$$z[k] = \left( a[k] \mathcal{I}_0(f_d) + \sum_{\substack{m=0 \\ m \neq k}}^{X-1} a[m] \mathcal{I}_{k-m}(f_d) \right) e^{j(2\pi k f_d + \phi)} + n[k], \tag{A.36}$$

where

$$\mathcal{I}_n(F_d T_S) = \int_{-\infty}^{\infty} g(t) p(kT - t) e^{-j2\pi F_d t} \, dt. \tag{A.37}$$

Since the impulse responses of SRRC filters are infinite and the frequency responses are finite, to evaluate the integral it is desirable to transform the expression into the frequency domain. For this, let

$$u_1(t) = g(t)e^{j2\pi(-F_d)t} \qquad\qquad u_2^*(t) = p(kT_S - t). \tag{A.38}$$

We can then reformulate Equation (A.37) to

$$\mathcal{I}_n(F_dT_S) = \int\limits_{-\infty}^{\infty} g(t)p(kT_S - t)e^{-j2\pi F_d t}\,dt = \int\limits_{-\infty}^{\infty} u_1(t)u_2^*(t)\,dt. \tag{A.39}$$

The frequency domain representation can be obtained by applying Parseval's theorem:

$$\mathcal{I}_n(F_dT_S) = \int\limits_{-\infty}^{\infty} u_1(t)u_2^*(t)\,dt = \int\limits_{-\infty}^{\infty} U_1(f)U_2^*(f)\,df. \tag{A.40}$$

$U_1(f)$ and $U_2^*(f)$ can then be found by the Fourier transform of $u_1(t)$ and $u_2^*(t)$ respectively. Regarding the Fourier transform of $u_1(t)$, we can use the translation property of the Fourier transform:

$$\mathcal{F}\left(u_1(t)\right) = \mathcal{F}\left(g(t)e^{j2\pi(-F_d)t}\right) = G(f + F_d). \tag{A.41}$$

For the Fourier transform of $u_2^*(t)$ the modulation property can be used:

$$\mathcal{F}\left(u_2(t)\right) = \mathcal{F}\left(p(kT_S - t)\right) = P(-f)e^{j2\pi f kT_S}. \tag{A.42}$$

We can now exploit the symmetry of the frequency response of the SRRC filter, i.e., $P(-f) = P(f)$. Using this and applying Equations (A.41) and (A.42) to Equation (A.40), we obtain an expression for the ISI components in the frequency domain:

$$\mathcal{I}_n(F_dT_S) = \int\limits_{-\infty}^{\infty} G(f + F_d)P(f)e^{j2\pi f kT_S}\,df. \tag{A.43}$$

## A.5. Simplification of $\mathcal{I}_n$

The different ISI components $\mathcal{I}_n(f_d)$ can be computed with

$$\mathcal{I}_n(f_d) = \int\limits_{-\infty}^{\infty} g(t)\,p(kT_S - t)\,e^{-j2\pi f_d \frac{t}{T_S}}\,dt = \int\limits_{-\infty}^{\infty} G(f + \frac{f_d}{T_S})\,P(f)\,e^{j2\pi f kT_S}\,df. \tag{A.44}$$

From the frequency responses of the SRRC pulse shaping filter $P(f)$ given in Equation (6.1) and the frequency shifted receive filter $G(f+\frac{f_d}{T_S}) = G(f+F_d)$ given in Equation (6.6) we can identify seven sections for the case of $|F_d T_S| < \beta$:

$$S_1 = [-\infty, -\frac{1+\beta}{2T_S}], \quad S_2 = [-\frac{1+\beta}{2T_S}, -\frac{1-\beta}{2T_S} - F_d], \quad S_3 = [-\frac{1-\beta}{2T_S} - F_d, \frac{1-\beta}{2T_S}],$$
$$S_4 = [-\frac{1-\beta}{2T_S}, \frac{1-\beta}{2T_S} - F_d], \quad S_5 = [\frac{1-\beta}{2T_S} - F_d, \frac{1-\beta}{2T_S}], \quad S_6 = [\frac{1-\beta}{2T_S}, \frac{1+\beta}{2T_S} - F_d],$$
$$S_7 = [\frac{1+\beta}{2T_S} - F_d, \infty].$$

This is visualized in Figure 6.3. The integral in Equation (A.44) can then be split into several integrals over the given sections:

$$\begin{aligned}
\mathcal{I}_n(f_d) = & \int_{S_1} 0 \; df + \int_{S_4} T_S \; e^{j2\pi f k T_S} df + \int_{S_7}^{\infty} 0 \; df \\
& + \int_{S_2} \frac{T_S}{2} \sqrt{1+\cos\left(\frac{\pi T_S}{\beta}\left[-(f+F_d) - \frac{1-\beta}{2T_S}\right]\right)} \\
& \qquad \cdot \sqrt{1+\cos\left(\frac{\pi T_S}{\beta}\left[-f - \frac{1-\beta}{2T_S}\right]\right)} \; e^{j2\pi f k T_S} df \\
& + \int_{S_3} \frac{T_S}{\sqrt{2}} \sqrt{1+\cos\left(\frac{\pi T_S}{\beta}\left[-f - \frac{1-\beta}{2T_S}\right]\right)} \; e^{j2\pi f k T_S} df \\
& + \int_{S_5} \frac{T_S}{\sqrt{2}} \sqrt{1+\cos\left(\frac{\pi T_S}{\beta}\left[f + F_d - \frac{1-\beta}{2T_S}\right]\right)} \; e^{j2\pi f k T_S} df \\
& + \int_{S_6} \frac{T_S}{2} \sqrt{1+\cos\left(\frac{\pi T_S}{\beta}\left[f + F_d - \frac{1-\beta}{2T_S}\right]\right)} \\
& \qquad \cdot \sqrt{1+\cos\left(\frac{\pi T_S}{\beta}\left[f - \frac{1-\beta}{2T_S}\right]\right)} \; e^{j2\pi f k T_S} df.
\end{aligned} \tag{A.45}$$

The evaluation of the integrals is generally rather elaborate due to the complex exponential. For the case of $n = 0$ however, the complex exponential disappears. We will therefore exemplify the evaluation of the integrals for $I_0(f_d)$. We will denote each integral with $\mathcal{S}_i$, where $i$ corresponds to the section. The evaluation of $\mathcal{S}_1$, $\mathcal{S}_7$ and $\mathcal{S}_4$ is trivial:

$$\mathcal{S}_1 = \mathcal{S}_7 = \int_{S_7} 0 \; df = 0, \tag{A.46}$$

$$\mathcal{S}_4 = \int\limits_{-\frac{1-\beta}{2T_S}}^{\frac{1-\beta}{2}-F_d} T_S \, df = 1 - \beta - F_d T_S. \tag{A.47}$$

For the evaluation of $\mathcal{S}_2$, let $x_1$ and $x_2$ denote the arguments of the cosines:

$$x_1 = \frac{\pi T_S}{\beta}\left[-(f+F_d) - \frac{1-\beta}{2T_S}\right], \qquad x_2 = \frac{\pi T_S}{\beta}\left[-f - \frac{1-\beta}{2T_S}\right]. \tag{A.48}$$

The following identity can be used to eliminate the square roots:

$$\sqrt{1+\cos(x)} = \sqrt{2}\cos\left(\frac{x}{2}\right). \tag{A.49}$$

This yields

$$\mathcal{S}_2 = \int_{S_2} T_S \cos\left(\frac{x_1}{2}\right)\cos\left(\frac{x_2}{2}\right) \, df. \tag{A.50}$$

We can then use the product-to-sum identities of trigonometry to obtain

$$\mathcal{S}_2 = \int_{S_2} \frac{T_S}{2}\cos\left(\frac{x_1}{2} - \frac{x_2}{2}\right) + \frac{T_S}{2}\cos\left(\frac{x_1}{2} + \frac{x_2}{2}\right). \tag{A.51}$$

Resubstituting $x_1$ and $x_2$ gives

$$\mathcal{S}_2 = \int\limits_{-\frac{1+\beta}{2T_S}}^{-\frac{1-\beta}{2T_S}-F_d} \frac{T_S}{2}\cos\left(\frac{\pi F_d T_S}{2\beta}\right) + \frac{T_S}{2}\cos\left(\frac{\pi T_S}{\beta}\left[-f - \frac{1-\beta}{2T_S}\right] - \frac{\pi F_d T_S}{2\beta}\right) df. \tag{A.52}$$

Finally, we can solve the integral to obtain

$$\mathcal{S}_2 = \frac{1}{2}\cos\left(\frac{\pi F_d T_S}{2\beta}\right)(\beta - F_d T_S). \tag{A.53}$$

Regarding the evaluation of section $S_3$, we can also use the identity given in Equation (A.49) to eliminate the square root. The resulting integral can be easily solved:

$$\mathcal{S}_3 = \int\limits_{-\frac{1-\beta}{2T_S}-F_d}^{-\frac{1-\beta}{2T_S}} T_S \cos\left(\frac{\pi T_S}{2\beta}\left[-f - \frac{1-\beta}{2T_S}\right]\right) df = \frac{2\beta}{\pi}\sin\left(\frac{\pi F_d T_S}{2\beta}\right). \tag{A.54}$$

The solutions to $\mathcal{S}_5$ and $\mathcal{S}_6$ can be obtained equivalently to $\mathcal{S}_3$ and $\mathcal{S}_2$, respectively. The result is intuitive, since the areas between $P(f)$ and $G(f+F_d)$ are equal for sections

$S_3, S_5$ and $S_2, S_6$ respectively. Therefore, we have

$$\mathcal{S}_6 = \mathcal{S}_2 = \frac{1}{2}\cos\left(\frac{\pi F_d T_S}{2\beta}\right)(\beta - F_d T_S), \tag{A.55}$$

$$\mathcal{S}_5 = \mathcal{S}_3 = \frac{2\beta}{\pi}\sin\left(\frac{\pi F_d T_S}{2\beta}\right). \tag{A.56}$$

It can be noted that the results of all integrals always contain the combination of $F_d T_S$, which corresponds to the normalized Doppler shift $f_d$ and can therefore be substituted. Finally, according to Equation (A.45), the results of the integrals of the different sections can be added to yield an expression for $\mathcal{I}_0(f_d)$:

$$\begin{aligned}\mathcal{I}_0(f_d) &= \mathcal{S}_1 + \mathcal{S}_2 + \mathcal{S}_3 + \mathcal{S}_4 + \mathcal{S}_5 + \mathcal{S}_6 + \mathcal{S}_7 \\ &= 1 - \beta - f_d + \frac{4\beta}{\pi}\sin\left(\frac{\pi f_d}{2\beta}\right) + (\beta - f_d)\cos\left(\frac{\pi f_d}{2\beta}\right).\end{aligned} \tag{A.57}$$

## A.6. Derivation of Doppler Distribution in Satellite Beam

In this section we want to derive the Doppler shift at any location in the satellite footprint. In general the Doppler shift depends on the relative velocity of transmitter and receiver, i.e., terminal and satellite, the carrier frequency $F_c$ and the speed of light $c$. It can be computed as

$$F_d = \frac{F_c v_{\text{rel}}}{c}. \tag{A.58}$$

The relative velocity $v_{\text{rel}}$ depends on the location of the terminal with respect to the satellite. The terminal may be located in a random location in the coverage area. In order to obtain an expression for the relative velocity of a randomly located terminal, the geometry of the satellite link has to be analyzed. A depiction of this is given in Figure A.1. We define the $z$-axis as the line connecting the center of the Earth and the satellite, which also passes through the center of coverage (CoC) on the Earth's surface. Hereby, we assume that the satellite's antenna is pointed towards the Earth along the $z$-axis, i.e., the satellite is not tilted. Furthermore, we define the $x$- and $y$-axis so that the speed vector $\mathbf{v}_s$ of the satellite only has one non-zero component, in our case we choose $y$. Therefore, the speed vector is given as

$$\mathbf{v}_s = \begin{pmatrix} 0 \\ v_s \\ 0 \end{pmatrix}, \tag{A.59}$$

where $v_s$ is the satellites orbital velocity. This depends solely on constants and the

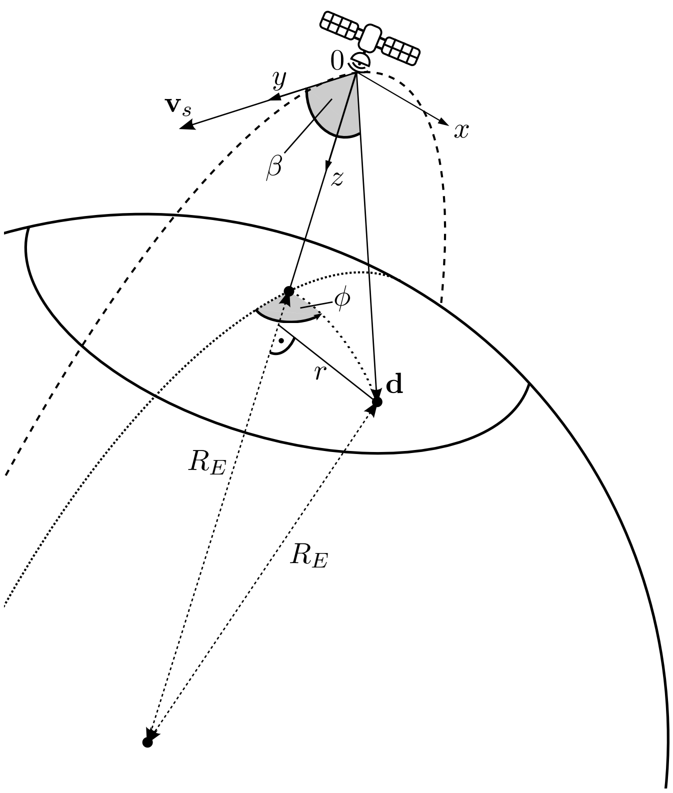

Figure A.1.: Geometry of a satellite link.

satellites altitude $h$, therefore, it can be calculated as

$$v_s = \sqrt{\frac{GM}{R_E + h}}, \tag{A.60}$$

where $G = 6.667 \cdot 10^{-11}\,\frac{\mathrm{m}^3}{\mathrm{kg\,s}^2}$ is the gravitational constant, $M = 5.972 \cdot 10^{24}\,\mathrm{kg}$ is the Earth's mass and $R_E = 6378\,\mathrm{km}$ is the Earth's radius. We assume that the communication system has a maximum distance at which the link can be closed. This is known as the maximum slant range $d_{\max}$. With this we can define the coverage of the satellite as a spherical cap with a maximum slant range of $d_{\max}$. Essentially, this corresponds to a circle around the $z$-axis with radius $r_{\max}$, which can be geometrically found to be

$$r_{\max} = R_E \sqrt{1 - \left(\frac{(R_E + h)^2 + R_E^2 - d_{\max}^2}{2R_E(R_E + h)}\right)^2}. \tag{A.61}$$

Once the coverage area is established, a general expression for the location of the terminal shall be found in order to compute the relative velocity. A point in the coverage area can be well defined in cylindrical coordinates, with the satellite being the center of the coordinate system. A point is then given by the distance from the center axis $r$, a phase $\phi$ and a height $z$. A restriction on the $z$-coordinate is that it must lay on the surface of the Earth. The Pythagoras theorem can be used to find $z = -R_E + \sqrt{R_E^2 - r^2} - h$. Therefore, every point $d$ in the coverage area of the satellite is characterized by

$$\mathbf{d} = \begin{pmatrix} r\sin(\phi) \\ r\cos(\phi) \\ -R_E + \sqrt{R_E^2 - r^2} - h \end{pmatrix}, \quad \text{where } r \in [0, r_{\text{max}}],\ \phi \in [0, 2\pi]. \tag{A.62}$$

The relative velocity between terminal and satellite is the component of $\mathbf{v}_s$, which acts in direction of $\mathbf{d}$. This can be found using trigonometry:

$$v_{\text{rel}} = v_s \cos(\beta), \tag{A.63}$$

where $\beta$ is the angle between the speed vector of the satellite and the vector from satellite to terminal. As both of these are known, we can calculate $\cos(\beta)$ as

$$\cos(\beta) = \frac{\mathbf{v}_s \cdot \mathbf{d}}{||\mathbf{v}_s||\,||\mathbf{d}||}. \tag{A.64}$$

Hereby, $||d||$ corresponds to the slant range of the link and be computed from either equation (A.62) or (A.61) as

$$d(r) = ||\mathbf{d}|| = \sqrt{(R_E + h)^2 + R_E^2 - 2(R_E + h)\sqrt{R_E^2 - r^2}}. \tag{A.65}$$

We can finally put together equations (A.65), (A.64), (A.63) and (A.58) to calculate the Doppler shift as

$$F_d = \frac{F_c v_{\text{rel}}}{c} = \frac{F_c v_s r\cos(\phi)}{c\,d(r)}. \tag{A.66}$$

# B. Reduction of ISI by Modification of the Receive Filter

Conventional communication systems ensure an ISI free transmission by employing a combination of pulse shaping and receive filter that satisfies the Nyquist criterion. Usually, this is achieved with SRRC filters at the transmitter and the receiver. However, in the given satellite scenario, the Doppler shift is unknown and therefore it is not possible to apply a (perfectly) matched filter at the receiver. As shown in Chapter 6, this has a twofold effect: an energy loss due to the frequency components which are filtered out, and the introduction of ISI. The discussion in the thesis has shown that the former effect dominated the performance for the problem of frame synchronization. It would be desirable to modify the filtering process to reduce the energy loss and ISI caused by the frequency offset. This short appendix introduces the strategy of using a different, broader receive filter, which yields better performance by mitigating the energy loss.

To reduce the energy loss, a larger amount of the spectral components of the incoming signal have to be contained by the filter. An intuitive approach to achieve this is to increase the bandwidth of the receive filter by the maximum expected Doppler shift $f_{\mathrm{max}}$, such that independently of the actual Doppler shift the received signal will always be completely contained by the filter. This would increase the captured signal energy, but would also increase the energy of the filtered noise, due to the larger bandwidth of the receive filter. Furthermore, increasing the bandwidth could also lead to inter-carrier interference from adjacent channels. However, given sufficiently large guard bands this may be neglected. A detailed study may provide more insight on the tradeoff of a reduction of ISI and the increase of the noise energy for larger bandwidth filters.

A possible strategy to increase the captured frequency components without increasing the energy of the filtered noise is to increase the roll-off factor of the SRRC receive filter. This widens the frequency response of the filter, i.e., it increases its spectral range, such that more frequency components are picked up, although with a small amplification. The energy of the Gaussian noise filtered with a SRRC receive filter does not depend on its roll-off factor [JBS06] and therefore does not increase for larger roll-offs. Thus, since a broader spectral range is considered, the energy loss of the signal is reduced, while

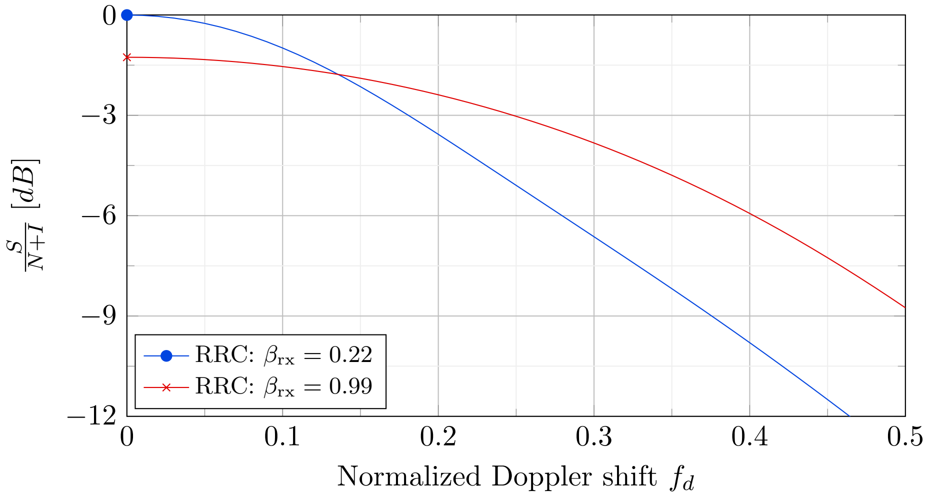

Figure B.1.: SINR for different SRRC roll-off factors. The roll-off of the transmitted pulse is $\beta_{\mathrm{tx}} = 0.22$. A filter span of 11 symbols and binary PSK was considered. $\frac{E_S}{N_0} = 0\,\mathrm{dB}$.

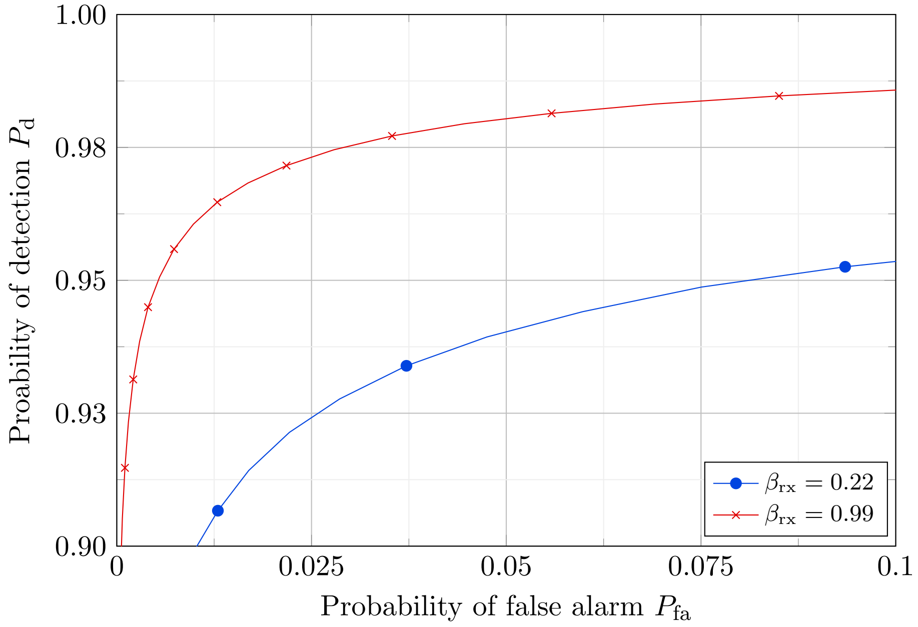

Figure B.2.: Simulated ROC using the swiveled correlator $L_{\mathrm{S}}$ with different SRRC roll-off factors for the receive filter. The roll-off of the transmitted pulse is $\beta_{\mathrm{tx}} = 0.22$. The filters were implemented as FIR filters with a span of 11 symbols. $\frac{E_S}{N_0} = -7\,\mathrm{dB}, K = 150, f_{\mathrm{max}} = 0.5$.

the energy of the filtered noise stays the same. A powerful measure to compare the performance of different filtering strategies is the signal-to-noise-and-interference ratio (SINR), which gives an insight on how large the useful signal energy is compared to the energy of the noise and interfering symbols. The SINR for SRRC filters with different roll-off factors is plotted in Figure B.1.

For a Doppler shift of $f_d = 0$, the modified roll-off negatively affects the SINR, since the combined pulse shaping and receive filter does not satisfy the Nyquist criterion. However, for larger Doppler shifts the effect reverses and the reduced energy loss due to the larger spectral range becomes apparent. Regarding the problem of frame synchronization, Figure B.2 shows the effect this has on the simulated ROC curve of the swiveled correlator. It becomes clear that increasing the roll-off factor has a beneficial effect on the detection performance when considering a large range of Doppler shifts. This study is far from complete and should only provide an initial insight on the possible benefit of modifying the receive filtering process.

# Bibliography

[3GP21] 3GPP, "Study on narrow-band Internet of things (NB-IoT) /enhanced machine type communication (eMTC) support for non-terrestrial networks (NTN)," 3rd Generation Partnership Project (3GPP), Technical Report (TR) 36.763, 06 2021, version 17.0.0. [Online]. Available: https://www.3gpp.org/ftp/Specs/archive/36_series/36.763/

[Abr70] N. Abramson, "The ALOHA system: Another alternative for computer communications," in *Proceedings of the November 17-19, 1970, Fall Joint Computer Conference*, ser. AFIPS '70 (Fall). New York, NY, USA: Association for Computing Machinery, 1970, p. 281–285. [Online]. Available: https://doi.org/10.1145/1478462.1478502

[AML05] K. Aamir, M. Maud, and A. Loan, "On Cooley-Tukey FFT method for zero padded signals," in *Proceedings of the IEEE Symposium on Emerging Technologies, 2005.*, 2005, pp. 41–45.

[Chi10] M. Chiani, "Noncoherent frame synchronization," *IEEE Transactions on Communications*, vol. 58, no. 5, pp. 1536–1545, 2010.

[CL02] Z. Y. Choi and Y. Lee, "Frame synchronization in the presence of frequency offset," *IEEE Transactions on Communications*, vol. 50, no. 7, pp. 1062–1065, 2002.

[CM06] M. Chiani and M. Martini, "On sequential frame synchronization in AWGN channels," *IEEE Transactions on Communications*, vol. 54, no. 2, pp. 339–348, 2006.

[CPV06] G. Corazza, R. Pedone, and M. Villanti, "Frame acquisition for continuous and discontinuous transmission in the forward link of satellite systems," *International Journal of Satellite Communications and Networking*, vol. 24, pp. 185 – 201, 03 2006.

[DGdRHG14] R. De Gaudenzi, O. del Rio Herrero, and G. Gallinaro, "Enhanced spread ALOHA physical layer design and performance," *International*

*Journal of Satellite Communications and Networking*, vol. 32, no. 6, pp. 457–473, 2014. [Online]. Available: https://onlinelibrary.wiley.com/doi/abs/10.1002/sat.1078

[JBS06] M. C. Jeruchim, P. Balaban, and K. S. Shanmugan, *Simulation of communication systems: modeling, methodology and techniques.* Springer Science & Business Media, 2006.

[LoR21] LoRa Alliance, "The LoRa alliance wide area networks for Internet of Things," Accessed Dec. 6, 2021. [Online]. Available: https://www.lora-alliance.org

[Mas72] J. Massey, "Optimum frame synchronization," *IEEE Transactions on Communications*, vol. 20, no. 2, pp. 115–119, 1972.

[NP33] J. Neyman and E. S. Pearson, "On the problem of the most efficient tests of statistical hypotheses," *Philosophical Transactions of the Royal Society A*, vol. 231, pp. 289–337, 1933.

[PM96] T. Pollet and M. Moeneclaey, "The effect of carrier frequency offset on the performance of band limited single carrier and OFDM signals," in *Proceedings of GLOBECOM'96. 1996 IEEE Global Telecommunications Conference*, vol. 1, 1996, pp. 719–723 vol.1.

[PP02] A. Papoulis and S. Pillai, *Probability, Random Variables, and Stochastic Processes*, ser. McGraw-Hill series in electrical engineering: Communications and signal processing. McGraw-Hill, 2002.

[PVVC$^+$10] R. Pedone, M. Villanti, A. Vanelli-Coralli, G. E. Corazza, and P. T. Mathiopoulos, "Frame synchronization in frequency uncertainty," *IEEE Transactions on Communications*, vol. 58, no. 4, pp. 1235–1246, 2010.

[Rob95] P. Robertson, "Optimal frame synchronization for continuous and packet data transmission," Ph.D. dissertation, UniBw Muenchen, Munich, April 1995. [Online]. Available: https://elib.dlr.de/58752/

[SCW08] W. Suwansantisuk, M. Chiani, and M. Z. Win, "Frame synchronization for variable-length packets," *IEEE Journal on Selected Areas in Communications*, vol. 26, no. 1, pp. 52–69, 2008.

[Sig21] Sigfox, "SIGFOX: The global communications service provider for the Internet of Things," Accessed Dec. 6, 2021. [Online]. Available: https://www.sigfox.com

[SKMB90] M. Sust, R. Kaufmann, F. Molitor, and G. Bjornstrom, "Rapid acquisition concept for voice activated CDMA communication," in *[Proceedings] GLOBECOM '90: IEEE Global Telecommunications Conference and Exhibition*, 1990, pp. 1820–1826 vol.3.

[SSS$^+$00] S. Spangenberg, I. Scott, M. Stephen, G. Povey, D. Cruickshank, and P. Grant, "An FFT-based approach for fast acquisition in spread spectrum communication systems," *Wireless Personal Communications*, vol. 13, pp. 27–55, 01 2000.

[Wat95] G. N. Watson, *A treatise on the theory of Bessel functions.* Cambridge university press, 1995.

[WRKH17] R. Wuerll, J. Robert, G. Kilian, and A. Heuberger, "A comparison of methods for detecting preambles with frequency offset at low SNR," in *2017 2nd International Conference on Computer and Communication Systems (ICCCS)*, 2017, pp. 96–100.

[WRKH18] R. Wuerll, J. Robert, G. Kilian, and G. Heuberger, "Optimal one-shot detection of preambles with frequency offset," in *2018 IEEE International Conference on Advanced Networks and Telecommunications Systems (ANTS)*, 2018, pp. 1–4.